CHALMERS
UNIVERSITY OF TECHNOLOGY

LeMMINGs - I. The eMERLIN legacy survey of nearby galaxies. 1.5-GHz parsec-scale radio structures and cores

Citation for the original published paper (version of record):
Baldi, R., Williams, D., McHardy, I. et al (2018). LeMMINGs - I. The eMERLIN legacy survey of nearby galaxies. 1.5-GHz parsec-scale radio
structures and cores. Monthly Notices of the Royal Astronomical Society, 476(3): 3478-3522.
http://dx.doi.org/10.1093/MNRAS/STY342

Monthly Notices
of the
ROYAL ASTRONOMICAL SOCIETY

MNRAS **476,** 3478–3522 (2018)
Advance Access publication 2018 February 9

doi:10.1093/mnras/sty342

LeMMINGs – I. The eMERLIN legacy survey of nearby galaxies. 1.5-GHz parsec-scale radio structures and cores

R. D. Baldi,[1]★ D. R. A. Williams,[1] I. M. McHardy,[1] R. J. Beswick,[2] M. K. Argo,[2,3] B. T. Dullo,[4] J. H. Knapen,[5,6] E. Brinks,[7] T. W. B. Muxlow,[2] S. Aalto,[8] A. Alberdi,[9] G. J. Bendo,[2,10] S. Corbel,[11,12] R. Evans,[13] D. M. Fenech,[14] D. A. Green,[15] H.-R. Klöckner,[16] E. Körding,[17] P. Kharb,[18] T. J. Maccarone,[19] I. Martí-Vidal,[8] C. G. Mundell,[20] F. Panessa,[21] A. B. Peck,[22] M. A. Pérez-Torres,[9] D. J. Saikia,[18] P. Saikia,[17,23] F. Shankar,[1] R. E. Spencer,[2] I. R. Stevens,[24] P. Uttley[25] and J. Westcott[7]

Affiliations are listed at the end of the paper

Accepted 2018 February 2. Received 2018 January 19; in original form 2018 January 19

ABSTRACT

We present the first data release of high-resolution ($\leq$0.2 arcsec) 1.5-GHz radio images of 103 nearby galaxies from the Palomar sample, observed with the eMERLIN array, as part of the LeMMINGs survey. This sample includes galaxies which are active (low-ionization nuclear emission-line regions [LINER] and Seyfert) and quiescent (H II galaxies and absorption line galaxies, ALGs), which are reclassified based upon revised emission-line diagrams. We detect radio emission $\gtrsim$0.2 mJy for 47/103 galaxies (22/34 for LINERS, 4/4 for Seyferts, 16/51 for H II galaxies, and 5/14 for ALGs) with radio sizes typically of $\lesssim$100 pc. We identify the radio core position within the radio structures for 41 sources. Half of the sample shows jetted morphologies. The remaining half shows single radio cores or complex morphologies. LINERs show radio structures more core-brightened than Seyferts. Radio luminosities of the sample range from 10^{32} to 10^{40} erg s^{-1}: LINERs and H II galaxies show the highest and lowest radio powers, respectively, while ALGs and Seyferts have intermediate luminosities. We find that radio core luminosities correlate with black hole (BH) mass down to $\sim$$10^7$ M$_\odot$, but a break emerges at lower masses. Using [O III] line luminosity as a proxy for the accretion luminosity, active nuclei and jetted H II galaxies follow an optical Fundamental Plane of BH activity, suggesting a common disc–jet relationship. In conclusion, LINER nuclei are the scaled-down version of FR I radio galaxies; Seyferts show less collimated jets; H II galaxies may host weak active BHs and/or nuclear star-forming cores; and recurrent BH activity may account for ALG properties.

Key words: galaxies: active – galaxies: jet – galaxies: nuclei – galaxies: star formation – radio continuum: galaxies.

1 INTRODUCTION

The advent of large-area, high-sensitivity, sub-arcsecond resolution surveys enables the investigation of large samples of extragalactic radio sources in order to understand the interplay and dominance of the two astrophysical processes which dominate the emission from our Universe: star-formation (SF) and accretion, i.e. the growth of galaxies and of super-massive black holes (SMBH). SF is fundamental for the formation and evolution of galaxies whilst accretion, the phenomenon responsible for powering active galactic nuclei (AGNs), provides a major power source in the distant Universe, dominating the emission across most wavelengths in the form of QSOs (quasi-stellar objects) and blazars. Conversely, in the local Universe, low-luminosity AGN (LLAGN, defined by Ho, Filippenko & Sargent 1997 as AGN with H α luminosity $\lesssim 10^{40}$ erg s^{-1}) and SF similarly contribute to illuminating the galaxies and the surrounding media.

Observational and theoretical studies support the co-evolution of the SMBH and host galaxy properties (e.g. the black hole [BH] mass – stellar velocity dispersion, or $M_{\rm BH} - \sigma$ relationship; Ferrarese & Merritt 2000; Tremaine et al. 2002; Di Matteo, Springel & Hernquist 2005; Di Matteo et al. 2008; Shankar et al. 2016) and

---

★ E-mail: R.Baldi@soton.ac.uk

Published by Oxford University Press on behalf of the Royal Astronomical Society

also the connection between SF and nuclear activity in LLAGNs (e.g. Kauffmann et al. 2007; LaMassa et al. 2013), where the faint radiation from the AGN allows the detection and the study of SF.

LLAGNs generally differ from luminous AGNs because they are powered by low accretion rate SMBHs and/or radiatively inefficient accreting SMBHs (e.g. Ho 1999a; Maoz 2007; Panessa et al. 2007), resulting in undetectably low optical to X-ray luminosities. LLAGNs are important because: (i) they numerically dominate the local Universe, outnumbering QSOs, and representing the most common mode of SMBH accretion; (ii) they are similar to quiescent galaxies, where the central SMBH is not necessarily active, allowing the study of nuclear triggering mechanisms; (iii) the nuclear emission does not swamp the emission of the host galaxy, allowing for the discrimination of the accretion process from SF; (iv) they are in a regime of low accretion rate, an optimal condition to investigate the transition of the radiative efficiency of accretion discs; (v) they can be associated with lower BH masses, crucial for constraining the scaling relations and the cosmological evolutionary models for SMBHs and galaxies (Barausse et al. 2017); (vi) they sample the low end of the luminosity function, important for a complete census of local SMBH activity.

The best way to study nuclear accretion and to disentangle it from the emission associated with star-forming regions is by observing nearby galaxies. The proximity enables high linear resolution and high sensitivity observations, allowing detections of lower luminosity sources, comparable to Sgr A*. Therefore, the local Universe provides a unique opportunity to explore LLAGNs and their interplay with their host galaxies at the low end of galaxy and AGN luminosity functions.

Although all bands are useful to fully constrain the origin of the emission from LLAGN, radio observations can offer the best single diagnostic of SF and nuclear accretion. Indeed, SF and AGN emit in the cm–mm band, where the two processes can be detected at low luminosity regime, since the galaxy contributes negligibly. Furthermore, long-baseline radio arrays provide high-angular resolution and high sensitivity, which are essential to detect and isolate the low-brightness nuclear emission with respect to the dominant galaxy emission. X-ray observations can also probe BH accretion at the galaxy centre. However, due to the cost and resolution limitation of the X-ray satellites and the great range of earth-based sensitive radio telescopes available to astronomers (e.g. VLA, VLBI, LOFAR, ALMA, eMERLIN), deep radio interferometric observations of local galaxies are ideal for probing small spatial scales of often $\lesssim$500 pc in the innermost central regions and identifying the emission from SMBHs.

High-resolution measurements of radio emission, flux density and its variability, compactness of the source, radio spectral index, brightness temperatures, and polarization are unique diagnostic tools for determining the nature of the radio emission. Synchrotron radiation generated in magnetic fields and free–free emission are typically the primary physical origin of the radio emission in local LLAGNs. In addition, LLAGNs are more efficient than QSOs at launching radio jets, whose synchrotron emission in some cases dominates the total output (Körding, Jester & Fender 2008). The detection of jets or high brightness temperature radio cores represents a valid method of the identification of an active SMBH at the galaxy centre, in the absence of other AGN signatures such as high-ionization emission lines, or an X-ray nucleus.

In the last half century, several interferometric radio surveys at 1.4 and 5 GHz with a resolution of $\sim$1 arcsec have been conducted on local LLAGNs (e.g. Ekers & Ekers 1973; Sadler 1984; Sadler, Jenkins & Kotanyi 1989; Ulvestad & Wilson 1989; Vila et al. 1990; Wrobel 1991; Slee et al. 1994; Sadler et al. 1995; Ulvestad & Ho 2001a; Gallimore et al. 2006) revealing a large fraction of radio cores, not only in elliptical but also in bulge-dominated spiral galaxies. LLAGNs typically have compact flat-radio-spectrum cores, interpreted as the synchrotron self-absorbed base of the jet which fuels larger-scale radio emission (Mezcua & Prieto 2014). Flat-spectrum radio sources can also result from thermal emission due to ionized gas in H II regions or from free–free non-thermal emission, occurring in compact nuclear star bursts (Condon et al. 1991) with low-brightness temperatures ($<10^5$ K). In addition, LLAGNs exhibit a large variety of radio morphologies: single core, core–jet, Fanaroff–Riley morphologies (FR; Fanaroff & Riley 1974), double lobes, and complex structures. The presence of composite radio structures may indicate the contribution of SF in the observed radio emission.

Unambiguously determining the physical nature of the radio emission in nearby galaxies is more than just of mere phenomenological interest. Understanding how radio core emission is associated with accretion-powered nuclei was the goal of several observational studies (e.g. Ho 1999b; Hardcastle & Worrall 2000; Capetti & Balmaverde 2006; Giroletti & Panessa 2009; Nagar, Falcke & Wilson 2005). Theoretical papers and numerical simulations which explored the accretion disc–jet relationship in the case of galactic nuclei (e.g. Begelman, Blandford & Rees 1984; Lovelace & Romanova 1996; Falcke & Biermann 1999; Beckwith, Hawley & Krolik 2008; Massaglia et al. 2016) suggested that LLAGNs have nuclear and jet properties, similar to powerful AGNs (Ulvestad & Ho 2001b). Compact nuclear radio emission and jets are expected from the accretion discs in the form of advection-dominated accretion flows (ADAF; Narayan, Mahadevan & Quataert 1998) at low accretion rates ($<10^{-3}$ of the Eddington rate). At higher rates, accretion takes the form of a geometrically thin, optically thick disc (standard disc; Shakura & Sunyaev 1973) with a hot, X-ray emitting corona, typically associated with luminous Seyferts. Many radio studies have reported jet structures associated with Seyferts (e.g. Ulvestad & Wilson 1984; Kukula et al. 1995, 1999; Thean et al. 2000; Orienti & Prieto 2010; Kharb et al. 2017). However, there are indications that by increasing either the accretion rate or the radiative efficiency of a standard disc, the fraction of radio jets observed in sources optically classified as Seyferts decreases from low-power Seyferts to QSOs (Blundell & Rawlings 2001; Ho & Ulvestad 2001; Ulvestad & Ho 2001a; Blundell 2003; Heywood, Blundell & Rawlings 2007). This radio behaviour of Seyferts generally suggests that jet production in radiatively efficient discs is still viable, but it is less efficient than in ADAF discs (Kukula et al. 1999; Nagar et al. 1999; Giroletti & Panessa 2009; King et al. 2011). However, since jets are universally observed across all types of AGNs, it is still under debate whether the accretion-jet symbiosis is scale invariant, regardless of the accretion mode, e.g. in the so-called ‘Fundamental Plane of BH activity’ (FPBHA) (Merloni, Heinz & di Matteo 2003; Falcke, Körding & Markoff 2004; Körding, Falcke & Corbel 2006; Panessa et al. 2007; Plotkin et al. 2012; Bonchi et al. 2013). This plane is believed to unify all active BHs at different mass scales (from galactic BHs to AGNs), indicating similar physical mechanisms in accretion and jet production from accreting compact objects.

A systematic, deep radio study of a large and complete sample of LLAGNs at milli-arcsecond resolution and μJy beam^{-1} sensitivity promises to provide insights on the radio properties of LLAGNs. While previous studies focused on only known active galaxies, a comprehensive radio study of inactive galaxies is necessary to investigate low-level SMBH accretion activities, akin to that of Sgr

A*. With these intentions, a new radio survey has been designed, based on the capabilities of the *enhanced Multi-Element Radio Linked Interferometer Network* (eMERLIN). The project is named the Legacy eMERLIN Multi-band Imaging of Nearby Galaxies survey (LeMMINGs, PI: McHardy and Beswick; Beswick et al. 2014). The target of this survey is the Palomar nearby galaxy sample (Filippenko & Sargent 1985), optically selected, with no radio constraint bias. In this paper we present results from an interim sample of 103 galaxies, essentially a random sub-set from the Palomar sample which demonstrates the data and imaging quality and shows the progress of the Legacy Programme. This sample includes LLAGNs and quiescent galaxies with a broad distribution of nuclear and host properties. In addition, excellent ancillary data that cover wide wavelength ranges, i.e. from infrared to X-ray, are available for the LeMMINGs sample of galaxies. Such a multiband survey will unveil the nature of the central engines in LLAGNs.

This paper is organized as follows. In Section 2 we present the LeMMINGs project and sample; the observations and calibration of the radio data are explained in Section 3. The radio properties of the sample are presented in Section 4 and the connection between the radio and optical properties to study the SMBH activity is examined in Section 5. We discuss the results for the different optical classes in Sections 6 and we provide an overview of the accretion–radio connection for LLAGNs and draw conclusions in Section 7. The Appendix shows the radio images of the radio detected galaxies and presents several tables listing their properties.

2 THE SAMPLE AND THE LEGACY

The sample investigated by the LeMMINGs survey is a subset of the Palomar sample, which itself includes nearby galaxies with $\delta > 0^\circ$ and $B_\mathrm{T} \leq 12.5$ mag from the Revised Shapley–Ames Catalog of Bright Galaxies (RSA; Sandage & Tammann 1981) and the Second Reference Catalogue of Bright Galaxies (RC2; de Vaucouleurs, de Vaucouleurs & Corwin 1976). The Palomar sample was observed by Ho, Filippenko & Sargent (1995) with the Hale 5m telescope at the Palomar Observatory (Filippenko & Sargent 1985) to carry out an intense spectroscopic campaign.

The Palomar galaxies have been optically classified, based on the ratios of several optical narrow lines (i.e. H β, [O III], H α, [N II]) extracted from a long-slit spectra on a nuclear region of 2×4 arcsec^2. Several optical classes are identified based on position in emission-line diagnostic diagrams similar to the methodology of Veilleux & Osterbrock (1987). Ho et al. (1997) distinguish H II, Seyfert, low-ionization nuclear emission-line regions (LINER), and Transition galaxies among the objects which show prominent emission lines.

H II galaxies (∼42 per cent of the Palomar sample) are considered star-forming galaxies where the emission lines are ascribed to young massive stars. Seyferts and LINERs (∼11 and 19 per cent of the Palomar sample, respectively) correspond to two active types of the central SMBHs. The Transition galaxies (∼ 14 per cent) are sources with composite characteristics of LINER nuclei contaminated by H II emission regions (e.g. Ho, Filippenko & Sargent 1993). The Transition class is not commonly used since its selection is more restrictive than the other optical classes (see Section 5.1). Therefore we prefer to remove this class of objects and convert the Transition galaxies into LINERs or H II galaxies based on different line diagnostics. The rest of the sample (∼14 per cent of the Palomar sample) shows no significant optical emission lines and are typically in elliptical and lenticular galaxies. These sources are named Absorption-line galaxies (ALGs). The lack of an emitting-line nucleus can be explained either by the inactivity of the SMBH or by the non-detection of a very weak active SMBH, whose emission lines are dominated by an old stellar population (similar to low-power radio galaxies; Buttiglione et al. 2009), or diluted by a non-thermal power-law continuum (similar to BL Lacs; Scarpa & Falomo 1997; Capetti, Raiteri & Buttiglione 2010), or dimmed by extinction through the host galaxy (Goulding & Alexander 2009). However, as already suggested by Ho, Filippenko & Sargent (2003) and pointed out by several authors (e.g. Best et al. 2005b; Baldi & Capetti 2010), the spectro-photometric properties of a large fraction of ALGs can be reconciled with the picture of LINERs.

The active galaxies in the Palomar sample have also been observed at low and high resolutions (arcsec and mas) at different cm-band frequencies (VLA, Nagar et al. 2000; Nagar, Wilson & Falcke 2001; Nagar et al. 2002a; Filho, Barthel & Ho 2000; Nagar et al. 2005; Ho & Ulvestad 2001; VLBA/VLBI, Falcke et al. 2000, Ulvestad & Ho 2001b, Nagar et al. 2002a,b; Anderson, Ulvestad & Ho 2004; Filho et al. 2004; Nagar et al. 2005; Filho et al. 2004; Nagar, Falcke & Wilson 2005; Panessa & Giroletti 2013; MERLIN Filho, Barthel & Ho 2006). However, an exhaustive sub-arcsecond sub-mJy radio study of the Palomar sample, unbiased towards the inactive galaxies, is still missing and is the goal of the LeMMINGs survey.

The LeMMINGs project focuses on a declination-cut subset of the Palomar galaxies, with declination $> 20^\circ$ (280 targets, more than one half of the original Palomar sample), to ensure proper visibility $(u - v)$ coverage at higher latitudes, accessible to the eMERLIN array. This legacy survey has been granted 810 h of eMERLIN time in total, representing the second largest of the eMERLIN legacy surveys. The aim of this project is to detect pc-scale radio components associated with either SF regions or AGNs. The survey is being carried out at 1.5 and 5 GHz using a two-tiered approach: the ‘shallow’ and ‘deep’ samples. The former consists of short observations of a large sample of 280 objects for a total of 750 h. The latter consists of six scientifically interesting targets observed for longer exposure times for a total of 60 h to reach a higher sensitivity. The observations of these six sources include the Lovell telescope and are published as separate papers: M 82 (Muxlow et al. 2010), IC 10 (Westcott et al. 2017), NGC 4151 (Williams et al. 2017), NGC 5322 (Dullo et al. 2018), M 51b (Rampadarath et al. 2018), and NGC 6217 (Williams et al, in preparation).

In this work, we present the first release[1] of the eMERLIN results of the ‘shallow sample’ at 1.5 GHz, focusing on the central galaxy region (0.73 arcmin^2) to explore the nuclear radio properties. In this first data release, we publish the data for 103 galaxies which are randomly selected from the original sample of 280 targets and are observed and calibrated until the end of the first semester of 2017. In the next data release, we will complete the sample and perform a detailed multiwavelength study, which will provide better statistics from greater numbers of sources per class, critical to draw final conclusions on the LeMMINGs sample.

Although the 103 sources (listed in Table 1) are randomly selected from the Palomar sample, all the optical classes (30 LINERs, 7 Seyferts, 16 Transition galaxies, 37 H II galaxies, and 13 ALGs, according to Ho et al. 1997) are included. However, we will revise the optical classifications based on the new updated diagnostic schemes (Section 5.1). The sample encompasses all galaxy morphologies (E, S0, Sa-b-c-d-m, I0, Pec). The galaxies extend in

---

[1] The eMERLIN radio images will be released through the Centre de Données astronomiques de Strasbourg (CDS) website to store and distribute the astronomical data in early 2018.

Table 1. Radio properties of the sample.

Name (1)	RA (2)	DEC. (3)	*D* (4)	LEM (5)	phase cal (6)	*Q* (7)	Beam (8)	PA (9)	rms (10)	det (11)	morph (12)
NGC 7817	00 03 58.899	+20 45 08.42	31.5	04	0004+2019	++	0.21 × 0.13	33.4	82	U	
IC 10	00 20 23.16	+59 17 34.7	1.3	04	0027+5958	++	0.21 × 0.11	88.2	89	U	
NGC 147	00 33 12.120	+48 30 31.46	0.7	04	0039+4900	++	0.24 × 0.14	− 63.2	73	I	A
NGC 185	00 38 57.970	+48 20 14.56	0.7	04	0039+4900	++	0.17 × 0.14	− 84.3	82	U	
NGC 205	00 40 22.075	+41 41 07.08	0.7	04	0038+4137	++	0.20 × 0.13	79.8	86	U	
NGC 221	00 42 41.825	+40 51 54.61	0.7	04	0038+4137	++	0.36 × 0.15	− 34.7	82	U	
NGC 224	00 42 44.330	+41 16 07.50	0.7	04	0038+413	++	0.19 × 0.14	− 71.4	79	U	
NGC 266	00 49 47.793	+32 16 39.81	62.4	03	0048+3157	+	0.48 × 0.31	− 40.0	95	I	A
NGC 278	00 52 04.300	+47 33 01.93	11.8	04	0039+4900	++	0.29 × 0.14	− 55.2	50	I	A
NGC 315	00 57 48.883	+30 21 08.81	65.8	03	0048+3157	+	0.12 × 0.12	45.0	5500	I	A
NGC 404	01 09 27.021	+35 43 05.27	2.4	03	0112+3522	+	0.43 × 0.26	− 46.8	61	U	
NGC 410	01 10 58.872	+33 09 07.30	70.6	03	0112+3522	+	0.52 × 0.32	− 46.85	140	I	A
NGC 507	01 23 39.950	+33 15 22.22	65.7	03	0112+3522	+	0.46 × 0.35	− 67.8	180	I	A
NGC 598	01 33 50.904	+30 39 35.79	0.7	03	0137+3122	+	0.32 × 0.13	12.1	103	U	
IC 1727	01 47 29.890	+27 20 00.06	8.2	03	0151+2744	+	0.48 × 0.17	− 8.8	98	U	
NGC 672	01 47 54.523	+27 25 58.00	7.5	03	0151+2744	+	0.50 × 0.23	− 16.3	118	U	
NGC 697	01 51 17.568	+22 21 28.69	41.6	03	0152+2207	+	0.43 × 0.13	13.7	95	U	
NGC 777	02 00 14.90	+31 25 46.00	66.5	02	0205+3219	m	0.23 × 0.15	7.6	77	I	A
NGC 784	02 01 16.932	+28 50 14.13	4.7	03	0151+2744	+	0.48 × 0.22	− 29.3	131	U	
NGC 812	02 06 51.497	+44 34 22.48	108.8	02	0204+4403	m	0.21 × 0.16	− 76.5	79	U	
NGC 818	02 08 44.510	+38 46 38.11	59.4	02	0204+3649	m	0.21 × 0.17	54.9	72	U	
NGC 841	02 11 17.334	+37 29 49.96	59.5	02	0204+3649	m	0.21 × 0.18	50.3	81	U	
NGC 890	02 22 01.008	+33 15 57.94	53.4	02	0226+3421	m	0.22 × 0.18	42.1	75	U	
NGC 891	02 22 32.907	+42 20 53.95	9.6	02	0222+4302	m	0.20 × 0.17	65.6	64	unI	
NGC 925	02 27 16.913	+33 34 43.97	9.4	02	0226+3421	m	0.22 × 0.18	42.7	75	U	
NGC 959	02 32 23.945	+35 29 40.80	10.1	02	0226+3421	m	0.20 × 0.15	43.4	81	U	
NGC 972	02 34 13.34	+29:18:40.57	21.4	02	0237+2848	m	0.24 × 0.17	37.2	69	I	B
NGC 2273	06 50 08.663	+60 50 44.50	28.4	27	0707+6110	++	0.20 × 0.16	48.1	930	I	E
NGC 2342	07 09 18.089	+20 38 09.22	69.5	27	0700+1709	++	0.18 × 0.18	0.0	65	I	E
NGC 2268	07 14 17.441	+84 22 56.18	34.4	25	0702+8549	+	0.20 × 0.20	0.0	91	U	
UGC 3828	07 24 35.784	+57 58 02.98	46.8	27	0707+6110	++	0.19 × 0.16	50.3	71	I	C
NGC 2276	07 27 14.485	+85 45 16.20	36.8	25	0702+8549	+	0.20 × 0.20	0.0	110	U	
NGC 2300	07 32 20.486	+85 42 31.90	31.0	25	0702+8549	+	0.20 × 0.20	0.0	60	I	A
UGC 4028	07 50 49.918	+74 21 27.79	52.7	25	0749+7420	+	0.20 × 0.20	0.0	100	I	C
NGC 2500	08 01 53.225	+50 44 13.56	10.1	27	0808+4950	++	0.20 × 0.16	48.6	93	U	
NGC 2543	08 12 57.955	+36 15 16.23	32.9	27	0815+3635	++	0.24 × 0.16	35.0	77	U	
NGC 2537	08 13 14.643	+45 59 23.25	9.0	27	0806+4504	++	0.21 × 0.16	40.3	92	U	
NGC 2541	08 14 40.073	+49 03 41.18	10.6	27	0808+4950	++	0.20 × 0.16	48.9	87	U	
NGC 2639	08 43 38.093	+50 12 19.94	42.6	27	0849+5108	++	0.20 × 0.19	68.0	130	I	C
NGC 2634	08 48 25.433	+73 58 01.62	30.2	25	0930+7420	+	0.20 × 0.20	0.0	82	I	A
NGC 2681	08 53 32.739	+51 18 49.35	13.3	27	0849+5108	++	0.19 × 0.16	51.8	920	I	C
IC 520	08 53 42.275	+73 29 27.32	47.0	25	0930+7420	+	0.20 × 0.20	0.0	102	U	
NGC 2655	08 55 37.731	+78 13 23.10	24.4	25	0919+7825	+	0.20 × 0.20	0.0	120	I	E
NGC 2715	09 08 06.196	+78 05 06.57	20.4	25	0919+7825	+	0.20 × 0.20	0.0	93	U	
NGC 2748	09 13 43.037	+76 28 31.23	23.8	25	0930+7420	+	0.20 × 0.20	0.0	90	U	
NGC 2841	09 22 02.655	+50 58 35.32	12.0	27	0929+5013	++	0.19 × 0.16	52.7	74	I	C
NGC 3184	10 18 16.985	+41 25 27.77	8.7	17	1020+4320	++	0.34 × 0.28	32.4	108	U	
NGC 3198	10 19 54.990	+45 32 58.88	10.8	17	1020+4320	++	0.20 × 0.20	0.00	114	I	A
NGC 3294	10 36 16.267	+37 19 28.52	26.7	17	1033+3935	++	0.37 × 0.29	− 56.4	119	U	
NGC 3319	10 39 09.533	+41 41 12.74	11.5	17	1033+3935	++	0.45 × 0.33	− 49.0	98	U	
NGC 3414	10 51 16.242	+27 58 29.88	23.9	17	1102+2757	++	0.22 × 0.14	20.60	60	I	C
NGC 3430	10 52 11.415	+32 57 01.53	26.7	17	1050+3430	++	0.20 × 0.20	0.0	100	I	E
NGC 3432	10 52 31.132	+36 37 07.60	7.8	17	1050+3430	++	0.47 × 0.28	− 16.7	110	I	A
NGC 3583	11 14 10.979	+48 19 06.16	34.0	18	1110+4817	++	0.17 × 0.13	− 59.4	79	U	
NGC 3600	11 15 51.980	+41 35 28.96	10.5	18	1110+4403	++	0.17 × 0.14	− 55.8	77	U	
NGC 3652	11 22 39.056	+37 45 54.14	33.5	17	1130+3815	++	0.20 × 0.20	0.0	89	U	
NGC 3665	11 24 43.630	+38 45 46.05	32.4	17	1130+3815	++	0.20 × 0.20	0.0	61	I	B
NGC 3675	11 26 08.584	+43 35 09.30	12.8	18	1110+4403	++	0.17 × 0.14	− 63.3	80	I	A
NGC 3726	11 33 21.174	+47 01 44.73	17.0	18	1138+4745	++	0.18 × 0.13	− 59.0	63	U	
NGC 3877	11 46 07.782	+47 29 40.20	91.6	18	1138+4745	++	0.18 × 0.13	− 54.7	66	U	
NGC 3893	11 48 38.207	+48 42 38.84	17.0	18	1153+4931	++	0.18 × 0.13	− 59.4	58	U	
NGC 3938	11 52 49.453	+44 07 14.63	17.0	18	1155+4555	++	0.19 × 0.14	− 54.2	74	I	A
NGC 3949	11 53 41.748	+47 51 31.62	17.0	18	1153+4931	++	0.18 × 0.13	− 56.5	71	U	

Table 1 – *continued*

Name (1)	RA (2)	DEC. (3)	*D* (4)	LEM (5)	phase cal (6)	*Q* (7)	Beam (8)	PA (9)	rms (10)	det (11)	morph (12)
NGC 4013	11 58 31.417	+43 56 49.28	17.0	18	1155+4555	++	0.19 × 0.14	– 56.4	70	unI	
NGC 4051	12 03 09.686	+44 31 52.54	17.0	18	1155+4555	++	0.18 × 0.14	– 58.6	71	I	C
NGC 4914	13 00 42.967	+37 18 55.20	62.4	10	1308+3546	++	0.21 × 0.19	28.4	71	U	
NGC 5005	13 10 56.312	+37 03 32.19	21.3	10	1308+3546	++	0.21 × 0.19	27.0	93	I	D
NGC 5055	13 15 49.329	+42 01 45.44	7.2	10	1324+4048	++	0.20 × 0.19	68.1	84	U	
NGC 5112	13 21 56.503	+38 44 04.23	20.5	10	1324+4048	++	0.20 × 0.19	34.4	104	U	
NGC 5194	13 29 52.698	+47 11 42.93	7.7	10	1335+4542	++	0.18 × 0.17	82.7	101	I	D
NGC 5195	13 29 59.590	+47 15 58.06	9.3	10	1335+4542	++	0.20 × 0.18	82.8	80	I	C
NGC 5273	13 42 08.386	+35 39 15.26	21.3	09	1340+3754	m	0.25 × 0.17	32.4	57	unI	
NGC 5297	13 46 23.694	+43 52 19.34	37.8	10	1335+4542	++	0.20 × 0.19	85.9	102	U	
NGC 5353	13 53 26.741	+40 16 59.24	37.8	09	1405+4056	m	0.18 × 0.14	29.6	180	I	A
NGC 5371	13 55 40.023	+40 27 42.37	37.8	09	1405+4056	m	0.20 × 0.15	35.0	80	U	
NGC 5377	13 56 16.670	+47 14 08.03	31.0	10	1358+4737	++	0.20 × 0.18	– 86.5	91	I	C
NGC 5383	13 57 04.980	+41 50 45.60	37.8	09	1405+4056	m	0.20 × 0.15	35.0	85	U	
NGC 5395	13 58 37.939	+37 25 28.49	46.7	09	1340+3754	m	0.23 × 0.15	30.8	77	U	
NGC 5448	14 02 50.072	+49 10 21.53	32.6	10	1358+4737	++	0.19 × 0.18	– 86.6	86	I	C
NGC 5523	14 14 52.310	+25 19 03.41	21.5	09	1419+2706	m	0.26 × 0.14	26.5	79	U	
NGC 5557	14 18 25.708	+36 29 37.28	42.6	09	1426+3625	m	0.24 × 0.15	30.6	90	U	
NGC 5660	14 29 49.801	+49 37 21.40	37.2	07	1439+4958	++	0.29 × 0.17	13.4	77	U	
NGC 5656	14 30 25.514	+35 19 15.98	42.6	09	1426+3625	m	0.23 × 0.15	29.6	86	U	
NGC 5676	14 32 46.853	+49 27 28.11	34.5	07	1439+4958	++	0.35 × 0.19	23.2	85	unI	
NGC 5866	15 06 29.561	+55 45 47.91	15.3	07	1510+5702	++	0.18 × 0.18	0.0	97	I	D
NGC 5879	15 09 46.751	+57 00 00.76	16.8	07	1510+5702	++	0.18 × 0.18	0.0	71	I	A
NGC 5905	15 15 23.324	+55 31 01.59	44.4	07	1510+5702	++	0.28 × 0.19	18.6	75	U	
NGC 5907	15 15 53.687	+56 19 43.86	14.9	07	1510+5702	++	0.28 × 0.19	18.6	90	unI	
NGC 5982	15 38 39.778	+59 21 21.21	38.7	07	1559+5924	++	0.26 × 0.19	20.2	78	U	
NGC 5985	15 39 37.090	+59 19 55.02	39.2	07	1559+5924	++	0.26 × 0.19	22.1	57	I	D
NGC 6015	15 51 25.232	+62 18 36.11	17.5	07	1559+5924	++	0.23 × 0.18	25.4	67	unI	
NGC 6140	16 20 58.162	+65 23 25.98	18.6	07	1623+6624	++	0.23 × 0.18	23.2	75	U	
NGC 6702	18 46 57.576	+45 42 20.56	62.8	05	1852+4855	m	0.19 × 0.16	56.7	74	I	C
NGC 6703	18 47 18.845	+45 33 02.33	35.9	05	1852+4855	m	0.19 × 0.15	53.6	66	I	A
NGC 6946	20 34 52.332	+60 09 13.24	5.5	05	2010+6116	m	0.19 × 0.15	– 84.1	57	I	E
NGC 6951	20 37 14.118	+66 06 20.02	24.1	05	2015+6554	m	0.20 × 0.15	88.5	55	I	C
NGC 7217	22 07 52.368	+31 21 33.32	16.0	05	2217+3156	m	0.18 × 0.18	0.0	75	I	C
NGC 7331	22 37 04.102	+34 24 57.31	14.3	05	2253+3236	m	0.15 × 0.15	0.0	81	U	
NGC 7332	22 37 24.522	+23 47 54.06	18.2	05	2238+2749	m	0.15 × 0.15	0.0	86	U	
NGC 7457	23 00 59.934	+30 08 41.61	12.3	05	2253+3236	m	0.15 × 0.15	0.0	92	U	
NGC 7640	23 22 06.584	+40 50 43.54	8.6	05	2312+3847	m	0.15 × 0.15	0.0	81	U	
NGC 7741	23 43 54.375	+26 04 32.07	12.3	04	2343+2339	++	0.19 × 0.14	36.0	70	U	
NGC 7798	23 59 25.503	+20 44 59.59	32.6	04	0004+2019	++	0.20 × 0.14	35.9	31	I	C

Column description: (1) source name; (2)-(3) RA and DEC position (J2000) from NED, using optical or infrared images; (4) distance (Mpc) from Ho et al. (1997); (5) LeMMINGs observation block; (6) phase calibrator name; (7) raw data and calibration quality: '++' = very good; '+' = good; 'm' = moderate; (8) restoring beam size in arcsec in full resolution map; (9) PA angle (degree) in full resolution map; (10) rms in full resolution map in μJy beam^{-1}; (11) radio detection status of the source: 'I' = detected and core identified; 'U' = undetected; 'unI' = detected but core unidentfied; (12) radio morphological class: A = core/core–jet; B = one-sided jet; C = triple; D = doubled-lobed ; E = jet+complex.

distance out to 120 Mpc, but with a median distance of ∼20 Mpc, similar to the original Palomar sample.

3 OBSERVATIONS AND DATA REDUCTION

The LeMMINGs shallow sample was observed with eMERLIN, an array consisting of seven radio telescopes spread across the UK. The configuration of eMERLIN is identical to that of MERLIN, but with a wider bandwidth and greater sensitivity. The observations were made at *L* band (20 cm, 1.5 GHz) without the Lovell telescope during 2015–2017. The sample was split into blocks of 10 galaxies (plus calibrators) per observation, clustered on the sky in intervals of right ascension to minimize the slewing of the telescopes. We use a 'snapshot imaging' mode: each observation has a time-on-source of ∼48 min per target, with the observations spread out over several hour angles to improve the $u - v$ coverage. The observational set-up used a total bandwidth of 512 MHz split into eight intermediate frequencies (IFs), each with a width of 64 MHz and consisting of 128 channels, centred on 1.5 GHz between 1.244 and 1.756 GHz.

In this work we provide the observations from 11 observing blocks: 2, 3, 4, 5, 7, 9, 10, 17, 18, 25, and 27, which include 110 targets. Several phase calibrators were used across the data sets, filling the gaps between the target pointings. The target-phase calibrator loop usually lasted 10–11 min, with 3–4 min on the phase calibrator and 7 min on the target, for a total of seven visits to fully cover the $u - v$ plane. The phase calibrators were selected from the VLBA calibrator lists (Beasley et al. 2002) to be unresolved on eMERLIN baseline scales. The bandpass calibrator (OQ 208) and the flux calibrator (3C 286) were typically observed at the end of each run.

3.1 Data calibration

The data reduction was carried out using AIPS (the Astronomical Image Processing Software from NRAO) software, following the calibration steps detailed in the eMERLIN cookbook (Belles et al 2015).

The large separation between the eMERLIN telescopes yield projected baselines in the *uv*-plane of up to ∼1300 kλ for our data sets. This results in high-resolution maps (beam FWHM ∼150 mas), which are necessary to study the pc-scale nuclear emission of the sources. Spurious, low-level radio frequency interference (RFI) can affect the observations of our targets, which are expected to be intrinsically weak in radio. First, we excised bright RFI, using the SERPENT auto-flagging code (Peck & Fenech 2013) written in Parsel-Tongue (Kettenis et al. 2006) principally for use in the eMERLIN pipeline (Argo 2015). Next, we carried out a further inspection of the data with the tasks SPFLG and IBLED to remove any remaining RFI not recognized by the automatic flagger. The first and last 10 channels in each IF were flagged because they are in the least sensitive areas of the passband and contribute mostly noise. We estimate that the flagged data are generally ∼30 per cent of a full data set, but represents a higher portion in those runs where antennas were missing from the observations.

No pipeline was used for the data reduction. We began the calibration procedures by fitting the offsets in delays using the task FRING before calibrating for phase and gain. We followed standard calibration procedures to determine the complex gain solutions from the flux calibrator to apply later to the data. Bandpass solutions were calculated with BPASS and applied to the data, followed by imaging the phase calibrator. We performed several rounds of phase-only self-calibration on the phase calibrators and a final round of self-calibration in phase and amplitude. The phase solutions are stable within $\pm 20^\circ$ independent of baseline. The amplitude solutions show typical variations within a range of 10–20 per cent. The solutions from self-calibration were then applied to the target field. For some scans, the calibration failed due to lack of sufficiently long exposure times on the phase calibrator caused by antenna problems and we deleted the affected calibrator-target scans for some objects.

At the end of the calibration, we find that observing blocks 4, 7, 10, 17, 18, and 27 have standard-quality data, while block 5 shows poor but still valid calibration solutions. During observing blocks 2, 3, 9, and 25 some eMERLIN antennas partially participate in observations due to a combination of weather and technical issues (weak flux calibrators on short scans, antenna dropouts in the observing run, or low-elevation observations). In summary, adequate data were acquired for all but seven of the observed galaxies (NGC 783, NGC 2685, NGC 3395, NGC 5033, NGC 5354, NGC 5548, NGC 7080). The exclusion of these seven galaxies resulted in a final sample of 103 galaxies presented in this paper. Table 1 displays the final list of sources with their associated phase calibrators, observing blocks and their calibration quality.

After a further inspection of the target data to check the quality and remove possible bad scans, the calibrated data sets were imaged (Stokes I) using the standard multiscale, multifrequency synthesis algorithm IMAGR, with a cell size of 0.05 arcsec and natural weighting. Because of the short observations with the snapshot imaging mode and the large bandwidth, the H I absorption line, which falls in the covered radio spectral window, was expected not to significantly contribute and, hence, it was not considered later in the calibration and in the imaging process. We performed a few rounds of self-calibration in phase and a final one in phase and amplitude, using 1–2 min of integration time and using at least 3σ detections for solutions. However, only sources with flux densities higher than five produced adequate solutions. This procedure improved the signal to noise of the final maps and reduced the phase and gain solution scatter. Bright sources in the fields were mapped separately while imaging the targets to reduce the noise in the field. At this stage of the project, we focused only on the central region of fields within an area of at least 1024 × 1024 pixels around the target position from NED (optical or infrared images), which corresponds to an area of 0.73 arcmin^2 (within the primary beam). Mapping the entire primary-beam field will be addressed in future papers. Several images were created in different resolutions (i) to study the morphology of each source, picking up the low-brightness diffuse emission, (ii) to increase the detection probability in case no source appears in the full-resolution map, and (iii) to detect any possible background sources or off-nuclear components. Lower-resolution maps were obtained using different values of the UVTAPER parameter in the IMAGR task, ranging between 750 and 200 kλ. This parameter specifies the width of the Gaussian function in the *uv*-plane to down-weight long-baseline data points. Smaller units of this parameter correspond to a shallower angular resolution, i.e. a larger beam size, up to a factor 10 larger than ones reached in full resolution (i.e. $\lesssim$1.5 arcsec).

For sources which have very elliptical restoring beams (with major-minor axis ratio higher than ∼2), we create a further map using a circular beam with a radius (typically 0.18–0.2 mas, presented in the Appendix) corresponding to the area equivalent to the elliptical beam. This approach helps us to identify possible genuine radio morphological elongations of the sources in the direction of the major axis of the beam.

We present in the Appendix the full- and low-resolution maps of the detected sources (Figs A1 and A2). The uv-tapered maps are typically obtained with $u - v$ scales of 750 kλ, corresponding to a resolution of 0.4 arcsec, double that of the full-resolution images. The large dynamic range of the radio maps highlights their quality, which both depend on the phase and amplitude solutions of the phase calibrators and the self-calibration on the target (if performed). For a small fraction of sources (in blocks 2, 3, 9, and 25), the image quality is modest, but still adequate for the purposes of our survey.

4 RADIO RESULTS

In this section we present the results related to the 103 radio images of the LeMMINGs legacy survey, which are released in this paper.

4.1 Radio maps and source parameters

Since the goal of this work is to study the radio emission associated with the SMBH, we search for detected radio sources in the innermost region of the optical galaxy extent (within a radius of 5 kpc at 20 Mpc) in full resolution and at multiple tapering scales. This choice favours the selection of radio sources co-spatial with the optical galaxy centre.

With a typical beam size of 0.15–0.2 arcsec at full resolution, each radio map of our sample reveals either single or multiple components. We adopt a consistent method in extracting source parameters (position, deconvolved size, peak flux density, integrated flux density, beam size, and PA), by fitting a 2-D Gaussian model with the task JMFIT. This procedure works for compact, unresolved components. For extended resolved structures, we measure the flux density within interactively defined boundaries with IMEAN for rectangular boxes or TVSTAT for irregularly shaped regions, following the emitting area of the sources. We always repeat the measurements several times using similar regions to derive an average value. The rms is measured in a region around the central source if present or at the optical centre, using a rectangular box with IMSTAT. We also apply this method to the uv-tapered maps to search for detected components. We consider the components detected if their flux densities were above 3σ above the typical rms measured around the source. Additional components not present in full resolution may appear in the uv-tapered map because the larger beam allows for low-brightness diffuse emission to emerge above the rms in the image. In this case we derive a 3σ upper-limit flux density for the undetected counterparts at full resolution.

In general, the final natural-weighted full-resolution maps reach a median rms of 70 μJy beam^{-1}, with a standard deviation of 0.54. Searching components within the central galaxy region, we detect significant radio emission ($\gtrsim$0.2 mJy) at the galaxy centre for 47 out of the 103 sources (~46 per cent). For such sources, we also extract the flux densities of their counterparts in the uv-tapered maps. The main parameters of the full-resolution maps (beam size, PA, rms) are listed in Table 1. The source parameters for the detected sources in full and low resolutions are listed in Tables A1 and A2 in the Appendix. For the remaining 56 objects, no significant radio emission has been detected in the core region of their fields both in full- and low-resolution images, which are essentially consistent with the 3σ rms level.

The detected sources show a large variety of radio morphologies from pc-scale unresolved single components to extended and complex shapes. The low-resolution maps typically show radio structures more extended than those revealed from full-resolution maps. The notable cases are the maps of NGC 5005 and NGC 5194: kpc-scale double lobes come out when reducing the resolution. The sizes of the radio structures vary from 150 mas for the unresolved sources to 26 arcsec for NGC 5005 with a median size of 1.5 arcsec. This interval corresponds to a physical linear range of ~10–1700 pc (median ~100 pc), depending on the galaxy of the sample. In Tables A1 and A2, we list the radio sizes for the resolved sources.

We perform a further step in the analysis, i.e. identifying the radio cores. We define cores in our sources as the unresolved radio centre of the sources, which may represent either a possible jet base or an unresolved central star-forming region, where the SMBH resides. The identification of the radio core in our maps depends on the specific morphology and on the proximity to the optical centre, taken from the NED catalogue (using the HST optical centroid in the best-case scenario). The core is generally recognized as an unresolved component at the centre of a symmetric structure (i.e. twin jets). In case of radio asymmetry, the optical centre and the brightness of the radio components (with the core brighter than the other components, i.e. in the case of one-sided jets) aid with pinpointing the radio core. Nevertheless, the distance between the optical galaxy centre and the closest possible radio component is the main criterion for a core identification.

Previous VLA observations on the Palomar sample detected and identified radio cores with a resolution of ~1 arcsec (e.g. Filho et al. 2000; Nagar et al. 2002a, 2005), generally matching the optical galaxy centres. Since our eMERLIN observations are five times higher in resolution, the VLA 1 arcsec-beam size can be used to roughly estimate the optical-radio offset we expect to find for our sample. Such an offset corresponds to an average area with a radius of ~100 pc for our sample. Indeed, the typical radio-optical separation observed in our sample is 0.3 arcsec, largely within the VLA resolution. To be precise, for 38 out of the 47 detected sources, radio emission is detected within 1 arcsec from the optical centre. Only three sources (NGC 147, UGC 4028, and NGC 3432) show a radio core at 1.5 arcsec from the optical centre. For these 41 (38+3) objects we assume that the radio cores are correctly identified (see Section 4.2) and we call them 'identified' hereafter. For the remaining 6 objects out of 47 detected (NGC 189, NGC 4013, NGC 5273, NGC 5676, NGC 5907, and NGC 6015) the identification of their radio cores is questionable because of either the lack of a clear core within 2 arcsec from the optical centre or the presence of multiple components of ambiguous nature. Furthermore, another two sources (NGC 2342 and NGC 3198), whose radio core has already been identified, show an unexpected additional radio source in the central field, possibly related to a background AGN. We call these 8 (6+2) sources 'unidentified' hereafter (see Section 4.3). The status of the radio detection/core-identification is listed in column 11 of Table 1.

4.2 Identified sources

Fig. A1 presents the full- and low-resolution radio maps (source characteristics in Table A1; radio contours and restoring beam in Table A3) of the 41 detected galaxies, where we identify the radio cores within 1.5 arcsec from the optical centre.

To test the possibility that the radio cores are associated with the galaxies and not with background objects, we calculate the probability of detecting a radio source above the survey detection limit of 0.2 mJy within a given sky area. For this purpose, we consider the source count distribution obtained with VLA observations at 1.4 GHz of the 13th *XMM*–Newton/ROSAT Deep X-ray survey area (Seymour, McHardy & Gunn 2004) over a 30-arcmin diameter region as no eMERLIN wide-field survey exists at this frequency in the literature. Based on this source density distribution, we expect to randomly detect one radio source out of 103 galaxies within a circular area of radius 3.7 arcsec. This result suggests that the radio cores, identified within the radio-optical offset of 1.5 arcsec observed for the 41 galaxies, are likely to be associated with the target sources.

The radio nuclei are detected at full resolution for all, except five targets (NGC 147, NGC 3430, NGC 3675, NGC 5985, and NGC 6702) for which only the low-resolution maps reveal the radio cores. The core peak flux densities for most of the sample fall below ~1 mJy beam^{-1} on a scale of 0.2 arcsec, reaching values up to ~500 mJy beam^{-1} for NGC 315. Assuming that a source is considered unresolved if its deconvolved size is smaller than the beam size at the FWHM for both major and minor axes, $\theta_{\rm M}$ and $\theta_{\rm m}$, most of these central components appear unresolved as cores. In fact, the peak flux densities of the core components are typically consistent with their integrated flux densities within a factor of ~2. The cores, which appear slightly resolved, typically show a protrusion associated with a core–jet morphology (Conway et al. 1994).

Most of the identified sources (25/41) show clear extended radio structures. In this paper we preferentially favour the interpretation that this extended radio emission originates from radio jets, based on their morphologies. This is because of the possibility that the radio emission from a galaxy disc is limited by the properties of our eMERLIN observations (long baselines and snapshot imaging), which are sensitive to compact radio emission like in jets, but insensitive to diffuse low-brightness emission, as expected by a galaxy disc (Brown & Hazard 1961; Kennicutt 1983) (see Section 6.5 for discussion).

We classify the identified sources into five radio structures based on both the full- and low-resolution maps (see column 12 of Table 1). The *core/core–jet* morphology (16 galaxies marked as A) consists of sources which show bright cores with a possible elongation in one direction (core–jet morphology) and radio components aligned in the same direction of the possible jet: an example is NGC 266. The *one-sided jets* (two galaxies marked as B) are sources which clearly show a jet extended asymmetrically: a clear example is NGC 3665. The *triple-sources* (14 galaxies marked as C) are sources which show three aligned components in full-resolution maps, which may turn into *twin symmetric jets* in low-resolution maps: for example, UGC 3828. Large *double-lobed* sources (four galaxies marked as D) are objects which show two large radio lobes at large scales in either full- or low-resolution maps, e.g. NGC 5005. The last class is represented by '*jet+complex*' (five galaxies marked as E) which reveal a possible jet but additional components emerge making the overall radio appearance complex: an example is NGC 2273. The radio sources which show jet-like morphologies (one-sided, two-sided, triple, double-lobed sources) are hereafter called 'jetted' and those without a clear jet, 'non-jetted'. Note that the radio classifications can be equivocal since the radio structures are generally characterized by low brightness.

4.3 Unidentified sources

Eight radio sources have been classified as 'unidentified'. Six of them do not show an unequivocal radio core, further than at least 2 arcsec from the optical centre. The remaining two are unknown radio sources detected in the central field of NGC 2342 and NGC 3198. Fig. A2 shows the full- and low-resolution maps (for radio contours and restoring beam, see Table A3) of the eight unidentified sources. Their radio source parameters are listed in Table A2.

For NGC 891, no components are detected in the full-resolution map but three components, which might be a triple source, are detected in the low-resolution map.[2] The nominal optical centre of the galaxy lies almost midway between two of the north components, being about 2.5 arcsec from either one. In NGC 4013 and NGC 5273, radio emission is detected in a circular shape (a diameter of 2.5–3 arcsec) around the optical centre, probably associated with a nuclear star-forming ring. For these three cases, the identification of the radio core is ambiguous, but the radio emission is likely associated with the target galaxies. For the other three remaining unidentified sources (NGC 5676, NGC 5907, and NGC 6015), radio components are detected further than 20 arcsec from the optical nucleus ($\sim$ 2 kpc), pointing to an SF origin or background sources.

In addition, two radio sources appear in the field of NGC 2342 and NGC 3198, respectively, 4 arcsec and 6 arcsec from the detected central cores, such that these off-nuclear sources are unidentified. In both cases, the source components appear two-sided and elongated, similar to radio jets, and hence these sources possibly belong to unknown background AGN.

Using the same approach explained in Section 4.2, the numbers of expected random radio detections within areas of radii 4 and 20 arcsec (the offsets measured above) are, respectively, 1.2 and 39.2. These values agree with the interpretation that the radio sources found in the field of NGC 2342 and NGC 3198 and the off-nuclear components in NGC 5676, NGC 5907, and NGC 6015 are potentially background objects.

Although the core has not been ascertained in the unidentified sources, these galaxies might still conceal active nuclei at the galaxy centre, emitting below the detection limit or simply not identified within a complex radio structure. HST and eMERLIN C-band observations will provide better constraints on the nature of these unidentified radio sources.

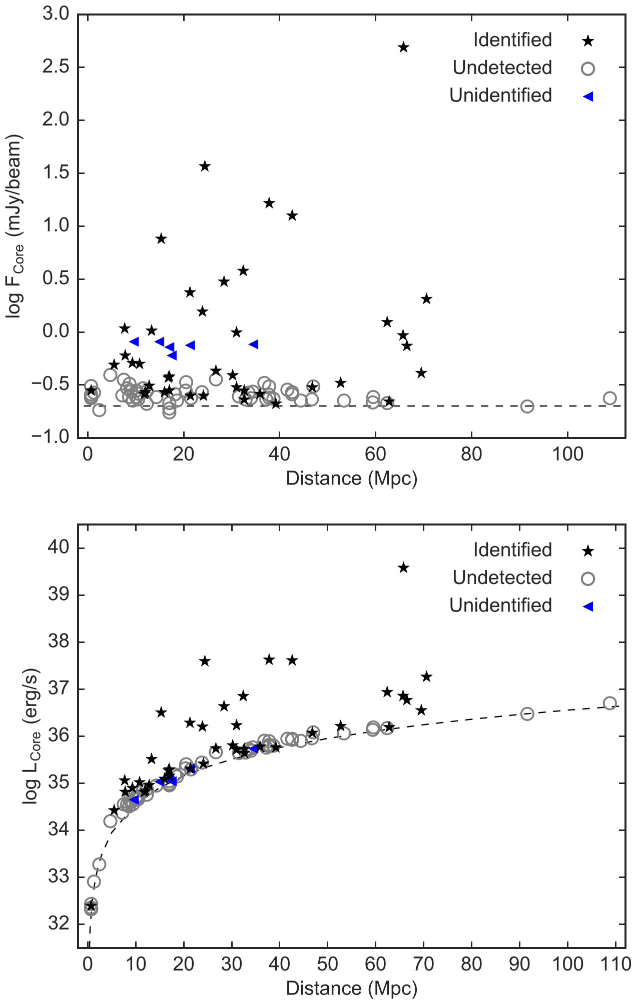

Figure 1. Radio core flux density ($F_{\rm core}$ in mJy beam^{-1}) (upper panel) and its luminosity ($L_{\rm core}$ in erg s^{-1}) (lower panel) as a function of the distance (Mpc) for the entire sample. The dashed lines correspond to the flux density and luminosity curves at a 3σ flux limit (0.2 mJy beam^{-1}). The different symbols correspond to identified sources, unidentified and undetected radio sources. For these last two types of sources, the values on the *y*-axis are meant as upper limits.

4.4 Radio brightness

The LeMMINGs survey detects for the first time faint radio cores ($<$ 1 mJy) on parsec scales for a large sample of nearby active and quiescent galaxies. The 3σ flux density limit of this survey is $\sim$0.2 mJy (Fig. 1 , upper panel), and we detect radio sources up to 70 Mpc; only two targets are more distant and are not detected. Table 2 collects the radio luminosities of the sample. Fig. 1 (lower panel) displays the core luminosity-distance curve for our sample. The identified sources are largely above the luminosity curve, while the undetected and unidentified sources straddle the curve.

The core luminosities range between 10^{32} and 10^{40} erg s^{-1}, with a median value of 5.8 $\times$ 10^{35} erg s^{-1}. The sources in our sample extend to lower radio luminosities, on average by a factor of 10

---

[2] SN 1986J, present in NGC 891 and detected in the radio band by VLA (Pérez-Torres et al. 2002), is located $\sim$1 arcmin south of the optical centre, which is beyond the region considered in our analysis.

Table 2. Optical-radio properties of the sample.

Name (1)	Hubble type (2)	Class HO ET AL. (1997) (3)	Class BPT (4)	σ km s^{-1} (5)	log($M_{\rm BH}$) M$_\odot$ (6)	$L_{\rm core}$ erg s^{-1} (7)	$L_{\rm tot}$ erg s^{-1} (8)	$L_{\rm [O\,III]}$ erg s^{-1} (9)	log($L_{\rm bol}/L_{\rm Edd}$) (10)
NGC 7817	SAbc	H	H	66.7	6.21	<35.64	–	39.29	– 1.51
IC 10	IBm?	H	H	35.5	5.11	<32.91	–	37.13	– 2.57
NGC 147	dE5 pec	ALG	ALG^a	22	4.28	32.39	32.92	–	–
NGC 185	dE3 pec	S2	L	19.9	4.10	<32.33	–	34.63	– 4.06
NGC 205	dE5 pec	ALG	ALG^a	23.3	4.34*	<32.36	–	–	–
NGC 221	E2	ALG	ALG^a	72.1	6.36*	<32.33	–	–	–
NGC 224	SAb	ALG	ALG^a	169.8	7.84	<32.32	–	–	–
NGC 266	SBab	L1.9	L	229.6	8.37	36.94	37.02	39.43	– 3.53
NGC 278	SABb	H	H	47.6	5.62	34.81	35.83	37.47	– 2.74
NGC 315	E+	L1.9	L	303.7	8.92*	39.58	39.61	39.43	– 4.02
NGC 404	SA0	L2	L	40	5.65∗	<33.28	–	37.16	– 3.08
NGC 410	E+	T2:	L	299.7	8.84	37.26	37.53	<39.32	<-4.11
NGC 507	SA0	ALG	ALG	307.7	8.88	36.86	37.07	–	–
NGC 598	SAcd	H	H^a	21	4.20	<32.43	–	<34.63	<-4.16
IC 1727	SBm	T2/L2	L	136.8	7.47	<34.55	–	37.34	– 4.72
NGC 672	SBcd	H	H	<64.3	<6.15	<34.55	–	37.66	– 3.08
NGC 697	SABc	H	H	75	6.42	<35.95	–	37.86	– 3.15
NGC 777	E1	S2/L2::	L^b	324.1	8.97	36.77	36.98	38.38	– 5.18
NGC 784	SBdm	H	H^c	35.5	5.11	<34.19	–	37.68	– 2.02
NGC 812	SAB0/a pecH	H	120.9	7.25	<36.70	–	38.68	– 3.16	
NGC 818	SABc	H:	H	151.3	7.64	<36.14	–	38.46	– 3.77
NGC 841	SABab	L1.9:	L^d	159.2	7.73	<36.19	–	38.74	– 3.58
NGC 890	SAB0	ALG	ALG	210.9	8.22	<36.06	–	–	–
NGC 891	SAb?	H	H$^{c,\,e}$	73.1	6.37	<34.65	–	36.29	– 4.66
NGC 925	SABd	H	H	71.9	6.34	<34.55	–	37.21	– 3.72
NGC 959	SAdm	H	H	43.6	5.47	<34.65	–	37.40	– 2.66
NGC 972	SAab	H	H	102.8	6.97	35.31	36.06	38.64	– 2.92
NGC 2273	SBa	S2	S	148.9	7.61	36.64	37.98	40.43	– 1.77
NGC 2342	S pec	H	H	147.3	7.60	36.55	37.64	39.71	– 2.48
NGC 2268	SABbc	H	H	143.3	7.55	<35.76	–	39.27	– 2.87
UGC 3828	SABb	H	H	73.9	6.39	36.07	36.63	38.84	– 2.14
NGC 2276	SABc	H	H	83.5	6.61	<35.90	–	38.17	– 3.03
NGC 2300	SA0	ALG	ALG	261.1	8.60	36.23	36.41	–	–
UGC 4028	SABc?	H	H	80.5	6.54	36.22	36.70	38.88	– 2.25
NGC 2500	SBd	H	H^c	47.1	5.61	<34.71	–	36.55	– 3.65
NGC 2543	SBb	H	H	112.4	7.12	<35.65	–	38.55	– 3.16
NGC 2537	SBm pec	H	H	63	6.11	<34.60	–	38.72	– 1.98
NGC 2541	SAcd	T2/H:	H^f	53	5.81	<34.72	–	36.80	– 3.60
NGC 2639	SAa?	S1.9	L^g	179.3	7.94	37.61	38.50	39.60	– 2.93
NGC 2634	E1	ALG	ALG	181.1	7.96	35.81	35.87	–	–
NGC 2681	SAB0/a	L1.9	L^h	109.1	7.07	35.51	35.99	38.37	– 3.29
IC 520	SABab?	T2:	L	138.1	7.48	<36.08	–	39.03	– 3.04
NGC 2655	SAB0/a	S2	L	159.8	7.74	37.59	37.97	39.44	– 2.89
NGC 2715	SABc	H	H	84.6	6.63	<35.32	–	37.79	– 3.43
NGC 2748	SAbc	H	H	83	7.65*	<35.44	–	37.83	– 4.41
NGC 2841	SAb	L2	L^c	222	8.31	34.84	35.47	38.19	– 4.63
NGC 3184	SABcd	H	H	43.3	5.46	<34.64	–	37.31	– 2.74
NGC 3198	SBc	H	H	46.1	5.57	35.02	35.19	36.97	– 3.19
NGC 3294	SAc	H	H	56.4	5.92	<35.66	–	38.33	– 2.18
NGC 3319	SBcd	H:	L^i	87.4	6.68	<34.84	–	37.07	– 4.20
NGC 3414	SA0 pec	L2	L^q	236.8	8.40*	36.20	36.33	39.06	– 3.95
NGC 3430	SABc	H	H	50.4	5.72	35.74	36.19	37.74	– 2.57
NGC 3432	SBm	H	H	37	5.18	34.82	34.83	38.00	– 1.77
NGC 3583	SBb	H	H	131.7	7.40	<35.69	–	38.26	– 3.73
NGC 3600	SAa?	H	H	49.8	5.70	<34.66	–	38.21	– 2.08
NGC 3652	SAcd?	H	H	56.4	5.92	<35.73	–	38.51	– 2.00
NGC 3665	SA0	H:	H	236.8	8.76*	36.85	37.67	38.28	– 4.73
NGC 3675	SAb	T2	L^e	108	7.26*	34.96	35.17	37.79	– 3.85
NGC 3726	SBa pec	H	H	41.5	5.38	<34.99	–	37.80	– 2.17
NGC 3877	SAc	H	H	86.1	6.66	<36.47	–	37.86	– 3.39
NGC 3893	SABc	H	H	85.3	6.64	<34.96	–	37.44	– 3.79
NGC 3938	SAc	H::	H^{e,j}	29.1	4.76	35.16	35.49	37.61	– 1.74

Table 2 – *continued*

Name (1)	Hubble type (2)	Class Ho et al. (1997) (3)	Class BPT (4)	σ km s^{-1} (5)	log($M_{\rm BH}$) M$_\odot$ (6)	$L_{\rm core}$ erg s^{-1} (7)	$L_{\rm tot}$ erg s^{-1} (8)	$L_{\rm [O\,III]}$ erg s^{-1} (9)	log($L_{\rm bol}/L_{\rm Edd}$) (10)
NGC 3949	SAbc	H	H	82	6.57	<35.05	–	37.44	– 3.72
NGC 4013	SAb	T2	L^{e,i}	86.5	6.67	<35.10	–	37.36	– 3.90
NGC 4051	SABbc	S1.2	S^{e,k}	89	6.10*	35.29	36.92	40.17	– 1.14
NGC 4914	E	ALG	ALG	224.7	8.33	<36.17	–	–	–
NGC 5005	SABbc	L1.9	L	172	8.27*	36.29	37.54	39.41	– 3.05
NGC 5055	SAbc	T2	L^{l}	117	8.92*	<34.37	–	37.44	– 6.07
NGC 5112	SBcd	H	H	<60.8	<6.05	<35.40	–	37.42	– 3.22
NGC 5194	SAbc pec	S2	S	96	6.85	35.06	36.14	38.91	– 2.53
NGC 5195	IA0 pec	L2:	L^{e}	124.8	7.31	34.90	35.59	37.84	– 4.06
NGC 5273	SA0	S1.5	S	71	6.61*	<35.31	–	39.82	– 1.38
NGC 5297	SABc	L2	L^{m}	61.3	6.07	<35.89	–	38.22	– 2.44
NGC 5353	SA0	L2/T2:	L	286.4	8.76	37.63	37.66	38.73	– 4.62
NGC 5371	SABbc	L2	L	179.8	7.94	<35.79	–	39.03	– 3.50
NGC 5377	SBa	L2	L	169.7	7.84	35.71	36.35	38.81	– 3.62
NGC 5383	SBb pec	H	H	96.5	6.86	<35.82	–	38.07	– 3.38
NGC 5395	SAb pec	S2/L2	L^{i}	145.5	7.57	<35.96	–	38.66	– 3.50
NGC 5448	SABa	L2	L	124.5	7.30	35.73	36.46	38.55	– 3.34
NGC 5523	SAcd	H	H	30.1	4.82	<35.29	–	37.25	– 2.16
NGC 5557	E1	ALG	ALG	295.3	8.81	<35.94	–	–	–
NGC 5660	SABc	H	H	60.7	6.05	<35.76	–	38.10	– 2.54
NGC 5656	SAab	T2::	L^{i,n}	116.7	7.19	<35.92	–	37.99	– 3.79
NGC 5676	SAbc	H	H	116.7	7.19	<35.74	–	37.96	– 3.82
NGC 5866	SA0	T2	L	169.1	7.84	36.50	36.76	37.50	– 4.93
NGC 5879	SAbc	T2/L2	L	73.9	6.62*	35.27	35.39	37.89	– 3.09
NGC 5905	SBb	H	H	174.6	7.89	<35.90	–	39.03	– 3.45
NGC 5907	SAc	H:	H	120.2	7.24	<35.03	–	36.88	– 4.94
NGC 5982	E3	L2::	ALG	239.4	8.44	<35.80	–	<38.55	<-4.48
NGC 5985	SABb	L2	L	157.6	7.71	35.76	36.30	38.76	– 3.54
NGC 6015	SAcd	H	H	43.5	5.47	<35.04	–	37.18	– 2.88
NGC 6140	SBcd pec	H	H	49.4	5.69	<35.15	–	37.52	– 2.76
NGC 6702	E	L2::	ALG	173.6	7.88	36.19	36.85	–	–
NGC 6703	SA0	L2::	L	179.9	7.95	35.78	35.91	38.46	– 4.08
NGC 6946	SABcd	H	H	55.8	5.90	34.43	35.73	37.03	– 3.46
NGC 6951	SABbc	S2	L^{o}	127.8	6.93*	35.42	36.02	38.69	– 3.25
NGC 7217	SAab	L2	L	141.4	7.52	35.09	35.87	38.31	– 3.80
NGC 7331	SAb	T2	L^{p}	137.2	8.02*	<34.95	–	38.30	– 3.76
NGC 7332	SA0 pec	ALG	ALG	124.1	7.08*	<35.18	–	–	–
NGC 7457	SA0?	ALG	ALG	69.4	6.95*	<34.88	–	–	–
NGC 7640	SBc	H	H	48.1	5.64	<34.51	–	36.84	– 3.39
NGC 7741	SBcd	H	H	29.4	4.78	<34.7	–	37.91	– 1.46
NGC 7798	S	H	H	75.1	6.42	35.64	36.54	38.64	– 2.37

Column description: (1) source name; (2) morphological galaxy type given from RC3 (de Vaucouleurs et al. 1991); (3) optical spectroscopic classification based on Ho et al. (1997): H=H II, S=Seyfert, L=LINER, T=Transition object, and ALG=Absorption line galaxy. The number attached to the class letter designates the AGN type (between 1 and 2); quality ratings are given by ':' and '::' for uncertain and highly uncertain classification, respectively. Two classifiations are given for some ambiguous cases, where the first entry corresponds to the adopted choice; (4) optical spectroscopic classification based on BPT diagrams and from the literature. See the notes for the classification based on the literature; (5) stellar velocity dispersion (km s^{-1}) from Ho et al. (2009); (6) logarithm of the SMBH mass (M$_\odot$) determined based on stellar velocity dispersions (Tremaine et al. 2002) and the galaxies marked with * have direct BH mass measurements from van den Bosch (2016). ; (7)-(8) radio core and total luminosities (erg s^{-1}); (9) [O III] luminosities from Ho et al. (1997); (10) Eddington ratio, i.e. ratio between the bolometric and Eddington luminosity.

Notes: letters correspond to following publications: *a* Lira et al. (2007); *b* Annibali et al. (2010); *c* Gavazzi et al. (2013); *d* Cid Fernandes et al. (2005); *e* Goulding & Alexander (2009); *f* Moustakas & Kennicutt (2006); *g* Trippe et al. (2010); *h* Cappellari et al. (2001); *i* SDSS; *j* Dale et al. (2006); *k* Balmaverde & Capetti (2014); *l* Balmaverde & Capetti (2013); *m* Rampazzo et al. (1995); *n* Leech et al. (1989); *o* Pérez et al. (2000); *p* Keel (1983), Bower (1992); *q* Falco et al. (1999), Sarzi et al. (2006).

more than in previous surveys of the Palomar sample, 10^{35} erg s^{-1} (Nagar et al. 2002a; Filho et al. 2006), within 100–1000 times higher than the luminosity of Sgr A*. The total radio powers for our sample estimated from the low-resolution radio images (median value of 2.2 × 10^{36} erg s^{-1}; Table 2) cover the same range of core luminosities. The radio core typically contributes ∼26 per cent of the total radio emission.

We calculated the brightness temperatures for the detected targets using the eMERLIN beam size and the peak flux densities. At the typical observed unresolved scale of 0.2 arcsec, the brightness temperatures of radio cores of ∼1mJy are of the order of 10^4 K, below the typical threshold of ∼10^6 K to discriminate between an AGN and stellar origin (Falcke et al. 2000). However, the calculated values do not preclude an active SMBH origin. Since the

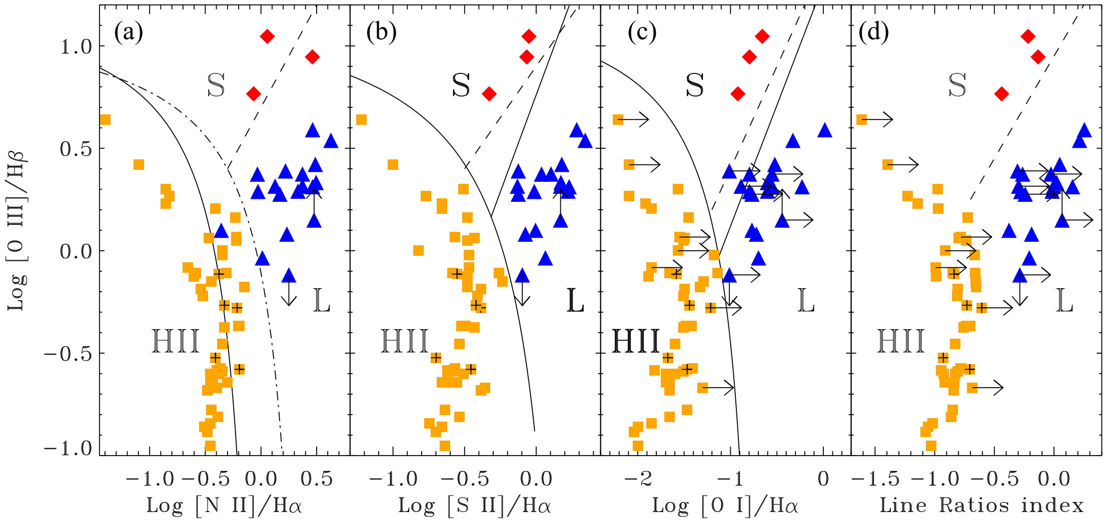

Figure 2. Diagnostic spectroscopic (BPT) diagrams for the 66 galaxies classified in this paper based only on the data from Ho et al. (1997) (the remaining sources are classified based on data from recent literature; see column 4 in Table 2): log([O III]/Hβ) versus (a) log([N II]/Hα), (b) log([S II]/Hα), (c) versus log([O I]/Hα), and (d) line ratios index (see definition in Section 5.1). In the first three panels, the solid lines separating star-forming galaxies, LINER, and Seyfert galaxies are from Kewley et al. (2006). The dashed lines between Seyferts and LINERs in the four panels are introduced by Buttiglione et al. (2010). In the diagram *a*, the sources between the solid and the dot–dashed lines (based on starburst models), (Kewley et al. 2001; Kauffmann et al. 2003) were classified as Transition galaxies by Ho et al. (1997), which we re-classify as LINER or H II galaxies based on the other diagrams. We mark LINERs as blue triangles, Seyferts as red diamonds, and H II galaxies as orange squares (with an additional plus for the jetted H II).

brightness temperatures depend on the flux densities and the sizes, at eMERLIN resolution and sensitivity only sources brighter than 5 mJy beam^{-1} can yield brightness temperatures greater than 10^6 K and, thus, be identified with synchrotron emission from relativistic jets. Only six sources exceed this core flux density limit and they are associated with all types of radio morphologies observed.

5 OPTICAL DATA

In this section, we introduce the optical classifications for the AGN and galaxies for our sample and we compare the different classes based on their radio properties.

5.1 Revised optical classification

The optical nuclear spectra contain several narrow and broad emission lines which diagnose the nature of the nuclear emission. Baldwin, Phillips & Terlevich (1981) introduced a series of widely used diagnostic diagrams (BPT diagrams) to classify objects based on their narrow emission line intensity ratios. In these diagrams, nebulae photoionized by hot, young stars (H II regions) can be distinguished from those photoionized by a harder radiation field, such as that of an AGN. A suitable choice of emission line ratio further delineates the excitation sequence in H II regions and divides AGN into a high-excitation class (Seyferts) and a low-excitation class (low-ionization nuclear emission-line regions, LINERs; Heckman 1980).

Ho et al. (1997) detected emission lines for most of the Palomar sample, which indicate the presence of active SMBHs and SF regions. They used spectroscopic criteria similar to Veilleux & Osterbrock (1987) to separate active nuclei from SF galaxies as they both used line ratios insensitive to the reddening, [O III]/Hβ, [N II]/Hα, [S II]/Hα, [O I]/Hα. We revise their classifications by using the state-of-the-art spectroscopic diagnostic diagrams based on the criteria introduced by Kewley et al. (2006) using the SDSS emission-line galaxies (using BPT diagrams, mostly including radio-quiet AGN) and by Buttiglione et al. (2010) using optical spectra for the 3C radio galaxies (only radio-loud AGN) with the Telescopio Nazionale Galileo. The Kewley et al. and Buttiglione et al. schemes marginally differ in the separation of LINERs and Seyferts from those used by Ho et al. (1997): the low [O III]/Hβ Seyferts are now reclassified as LINERs. Furthermore, we also estimate for all narrow-lined objects the average of the low ionization lines ratios, i.e. 1/3 (log([N II]/Hα)+ log([S II]/Hα)+ log([O I]/Hα)) defined as the 'line ratios index' by Buttiglione et al. (2010). This index appears to be more stable than the other single line ratios as it is an averaged line ratio, and represents a further diagnostic for a more robust separation between LINERs and Seyferts.

For our sample of 103 sources, 66 are detected (i.e. having line uncertainties smaller than 50 per cent in Ho et al. 1997) in at least four emission lines, which should be sufficient for a secure classification in the BPT diagrams (Table 2): these galaxies are displayed in Fig. 2. Of the remaining 37 sources, 23 are classified based on recent data from the literature (see notes in Table 2). The classification of 12 galaxies, all ALGs, remains unchanged from Ho et al. (1997), because we do not find further spectra available in the literature with detectable emission lines. In addition, we reclassify the LINERs, NGC 5982, and NGC 6702, as ALGs, because they do not show any significant emission lines.

We choose to remove the class named 'Transition galaxies' since it is a composite class of H II and AGN objects, based only on one diagnostic panel ([O III]/Hβ versus [N II]/Hα in the BPT diagrams). Therefore the sources which fall in the 'transition' region in this panel (see Fig. 2) are then classified as LINER or H II depending on where they fall on the other diagnostic diagrams. Finally, each object is classified as H II, LINER, or Seyfert based on at least two diagnostic diagrams in case the third one disagrees with the previous two.

The revised diagnostic diagrams mostly affect the number of Seyferts: four Seyferts and two objects tentatively classified as Seyfert/LINERs according to Ho et al. (1997) are now classified as LINERs (NGC 185, NGC 777, NGC 2639, NGC 2655, NGC

Table 3. Spectral–radio morphological classification breakdown.

Radio class	LINER	ALG	Seyfert	H II	Tot
	Optical class				
Core/core–jet (A)	8	4	0	4	16
One-sided jet (B)	0	0	0	2	2
Triple (C)	9	1	1	3	14
Doubled-lobed (D)	3	0	1	0	4
Jet+complex (E)	1	0	1	3	5
Tot	21	5	3	12	41
Unidentified	1	0	1	4	6
Undetected	12	9	0	35	56
Total	34	14	4	51	103

Notes. The sample is divided in radio and optical classes based on their radio detection, core-identification, or non-detection.

5395, and NGC 6951) because of a low [O III]/H β as explained previously. The two sources which show optical broad lines remain classified as type-1 Seyferts (NGC 4051 and NGC 5273). In addition, only one H II galaxy is now considered a LINER (NGC 3319).

After the revised optical classification, the sample discussed in this paper consists of 52 H II galaxies, 33 LINERs, 14 ALGs, and 4 Seyferts. As we removed the Transition galaxies from the sample and reclassified them as LINERs or H II regions, the comparison with the full Palomar sample classified by Ho et al. (1997) is not straightforward. LINERs and H II galaxies now account for ∼45–50 per cent of the sample. Only Seyferts appear to be less represented than in the original Palomar sample.

When considering the galaxy morphological types, most of the sources are late-type galaxies (from Sa to Sd, ∼75 per cent), with a smaller fraction of elliptical and lenticulars (E and S0). Using the stellar velocity dispersions measured from the optical spectra by Ho et al. (2009) (see Table 2) and the empirical relation from Tremaine et al. (2002), we inferred their BH masses, which range between 10^4 and 10^9 $M_\odot$. The most massive BHs are, not surprisingly, found in the elliptical galaxies, that host LINERs and ALGs. We also derive the BH masses using the $M_{BH} - \sigma$ relations from Graham & Scott (2013) and Kormendy & Ho (2013). The different relations lead to M_{BH} measurements,[3] which agree with each other for intermediate BH masses, $\sim10^6$–10^7 $M_\odot$, but differ at high BH masses within 0.5 dex and at low BH masses within 1 dex. For 17 sources, we use the direct BH measurements (derived from stellar and gas dynamics, mega-masers, and reverberation mapping) available from the BH mass compilation of van den Bosch (2016). These M_{BH} values are consistent with the values obtained using the $M_{BH} - \sigma$ relation from Tremaine et al. (2002), which we then choose to use for our work. However, the choice of the $M_{BH} - \sigma$ relation used for our sample does not significantly affect the scope of the work.

5.2 Radio versus optical classification

Table 3 summarizes the number of detected, unidentified, and undetected sources dividing the sample by optical class.

Although Seyferts have the highest radio detection rate (4/4), their scarcity in our sample limits our conclusions. LINERs have the second largest detection rate in the sample: 22 objects out of 34 (∼65 per cent). Absorption line galaxies have a smaller detection rate than LINERs: 5 out of 14 galaxies (∼36 per cent). The radio detection fraction is yet lower for H II galaxies with 16 out of 51 (∼31 per cent). Considering only those sources for which we identify a radio core, results in the exclusion of six sources (one LINER, one Seyfert, and four H II galaxies) such that the detection fractions become LINERs 21/34, Seyferts 3/4, ALGs 5/14, and H II galaxies 12/51.

By dividing the sample into the different radio morphological types, the sources in the sample spread across all the radio categories (Table 3). The radio classes which imply a presence of a jet (B, C and D) encompass all the optical classes. LINERs show different radio structures, but mostly core/core–jet and triple structures. ALGs are mostly core/core–jet, Seyferts show edge-brightened radio morphologies, and H II galaxies are not associated with large double-lobed radio morphologies. Although H II galaxies are powered by SF according to the BPT diagrams, five sources show clear jetted morphologies: two show one-sided jets, a possible sign of a Doppler-boosted jet. In fact, one of these two is NGC 3665, which exhibits an FR I radio morphology extended over ∼3 kpc at the VLA scale (Parma et al. 1986). Conversely, the remaining seven H II galaxies do not show clear evidence of jets (single cores or complex morphologies).

Regarding relations with galaxy type, early-type galaxies (elliptical and lenticular) are most frequently detected as radio sources (∼50 per cent) and are typically associated with jetted radio morphologies. Spiral galaxies, which are the most abundant host type (73 per cent), are detected in radio in one-third of cases, and are associated with all types of radio structures. Only one irregular galaxy is detected out of two in this sample.

Fig. 3 shows the luminosity distribution of the radio core and total emission for our sample for each optical class. The LINERs produce the largest radio core luminosities with a median value of 6.0×10^{35} erg s^{-1}. ALGs show a slightly higher median value (1.6×10^{36} erg s^{-1}), but are also among the weakest radio sources. Seyferts and H II galaxies show the lowest core power, 2.0×10^{35} and 3.2×10^{35} erg s^{-1}, respectively. The undetected and unidentified galaxies have radio luminosities ranging between 10^{32} and 10^{37} erg s^{-1}, with a median radio luminosity of 1.7×10^{35} erg s^{-1}.

The total radio luminosities of the sample generally cover the same range of values as the core powers: LINERs and H II galaxies are again at the two opposites of the luminosity range. The core dominance, which represents the contribution of the radio core with respect to the total flux density of the source, differs for each optical class. The ALGs are the most core dominated (∼60 per cent), followed by LINERs and H II galaxies with moderate core dominance (∼27 per cent), while the Seyferts have the smallest core dominance (∼2.4 per cent).

By dividing our sample by galaxy morphological type, early-type hosts produce the highest and lowest radio luminosities, because they mostly include LINERs and ALGs (Fig. 3, lower plot). The most numerous type of galaxies in our sample, spirals, spreads across the entire distribution of radio luminosities. The only irregular galaxy detected in the radio band (NGC 5195) has low core and total luminosities of 7.9×10^{34} and 3.9×10^{35} erg s^{-1}, respectively.

For the brightness temperatures, the values mostly reflect the flux density distribution. In fact, LINERs show the highest values, with six sources exceeding 10^6 K, which can be thus associated

---

[3] The median M_{BH} and standard deviations of the M_{BH} distribution for our sample using the three $M_{BH} - \sigma$ relations are (in a logarithmic scale) 6.85, 6.46, and 7.09 $M_\odot$ and 1.18, 1.62, 1.29 $M_\odot$ for Tremaine et al. (2002), Graham & Scott (2013), and Kormendy & Ho (2013), respectively. The Tremaine et al. correlation produces the smallest M_{BH} scatter for our sample.

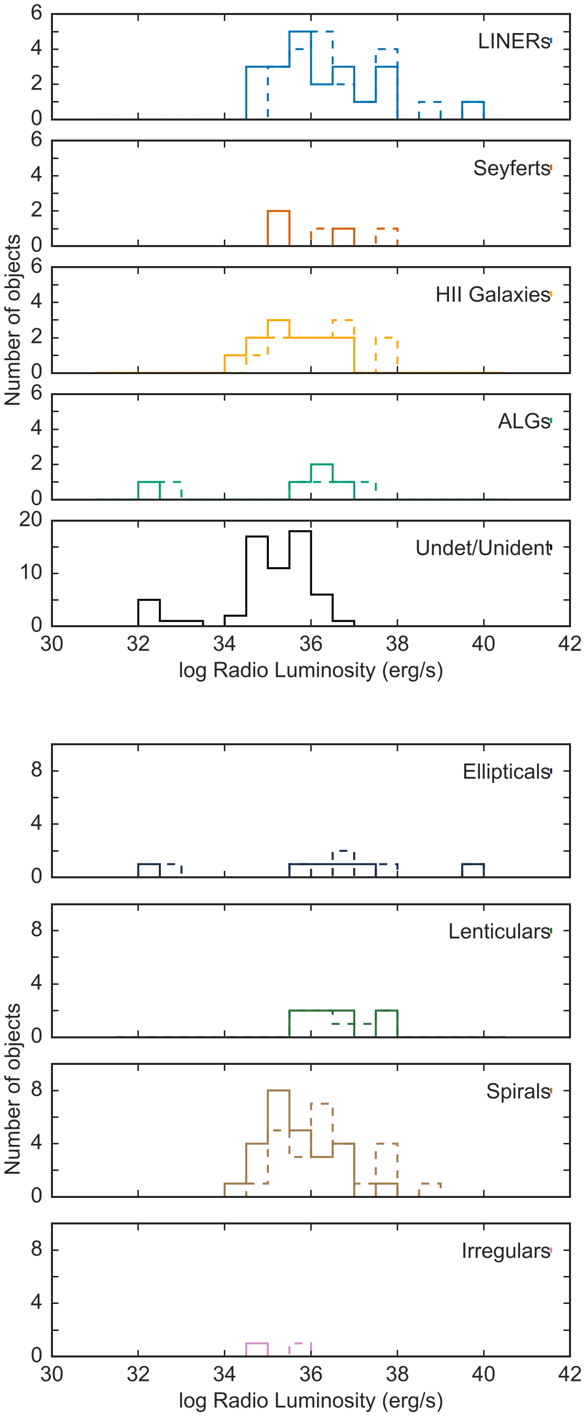

Figure 3. Histograms of the radio luminosity (erg s^{-1}) per optical class (upper plot) and host morphological type (lower plot). The solid-line histogram represents the radio core luminosity distribution and the dashed line corresponds to the total radio luminosity distribution. In the bottom panel of the upper plot, we also show the 3σ upper limit radio luminosity distribution for the undetected and unidentified sources.

with synchrotron emission from relativistic jets. Seyferts, ALGs, and H II have, respectively, lower brightness temperatures, down to 10^3 K. Therefore, we cannot use the brightness temperature as a diagnostic of the presence of an AGN for the vast majority of the sample.

5.3 Radio properties versus BH mass

As the BPT diagrams ascribe the ionization of the emission lines for Seyferts and LINERs to their central AGN, their radio cores are expected to be attributed to active SMBHs. Conversely, caution is needed to confirm the AGN origin of the identified cores of H II galaxies, since both small star-forming clusters and weak AGNs can account for the radio emission in regions of size 100 pc (Condon et al. 1982; Varenius et al. 2014; Salak et al. 2016). Instead, ALGs might exhibit radio activity from their SMBHs, while they are undetected in the optical band.

Two possible diagnostics to identify active SMBHs are the BH mass, $M_{\rm BH}$, and the radio luminosity (listed in Table 2). The former can be used as an indicator of nuclear activity, because active nuclei are preferentially associated with massive BHs (e.g. Best et al. 2005a; Gallo et al. 2010). The latter roughly assesses the probability of being radio-jet dominated: a sign of an active SMBH. Furthermore, the two quantities are typically connected in active nuclei: radio-emitting AGNs tend to be radio louder as the BH becomes more massive (e.g. Best et al. 2005a). The histogram in Fig. 4 (upper panel) describes the radio core detection for our sample as a function of BH mass. It is evident that the detection fraction increases with BH mass. For $M_{\rm BH} > 10^7$ $M_{\odot}$, this fraction is ~50 per cent reaching 85 per cent in the last bin, $\sim 10^8 - 10^9$ $M_{\odot}$, while it drops to less than 40 per cent below 10^6 $M_{\odot}$.

Fig. 4 (lower panel) also shows the distribution of core luminosities as a function of BH mass. Two different situations appear in this plot, roughly separated at 10^6–10^7 $M_{\odot}$: a positive radio-$M_{\rm BH}$ sequence appears for $M_{\rm BH} \gtrsim 10^{6.6}$ $M_{\odot}$, where all jetted or active galaxies are included, while at lower BH masses a luminosity plateau emerges. Despite the large scatter, we note that the $M_{\rm BH}$–$L_{\rm core}$ sequence includes LINERs and Seyferts, which generally tend to have larger BH masses in local galaxies (Best et al. 2005b; Kewley et al. 2006) and clearly have an active nucleus as they are detected in the emission line diagrams. Note that the ALGs, which are not detected in emission lines, are also present along this sequence, whilst H II galaxies are mostly at lower BH masses where the flattening of the sequence is evident. Therefore, we fit the data points present in this sequence with a linear relation and we find a correlation in the form $L_{\rm core} \sim {M_{\rm BH}}^{1.0\,\pm\,0.2}$ with a Pearson correlation coefficient (r-value) of 0.663, which indicates that the two quantities do not correlate with a probability smaller than 6.5×10^{-5}. Conversely, if we search for a correlation including all the detected radio sources on the entire range of BH masses, the correlation is drastically less significant (r-value is 0.525 with a probability of 4.2×10^{-4} of being a fortuitous correlation) due to the radio-$M_{\rm BH}$ break at $\sim 10^{6.6}$ $M_{\odot}$.

In general, LINERs, Seyferts, and ALGs appear to be on the correlation, suggesting that the radio core emission is probably dominated by the AGN component. For H II galaxies, those which display a jetted radio morphology, all with $M_{\rm BH} > 10^6$ $M_{\odot}$, lie at the low end of the relation. Conversely, the non-jetted H II galaxies fall on the flat part of the $M_{\rm BH}$–$L_{\rm core}$ relation. This different behaviour between the jetted non-jetted H II galaxies suggests an AGN dominance for the former group and an SF dominance for the latter group.

Considering the radio morphological classes, all structures are represented along the sequence (Fig. 5). The core/core–jet morphology spans the entire range of BH masses and total radio luminosities, dominating the distribution below 10^6 $M_{\odot}$ and above 10^8 $M_{\odot}$. The remaining morphological radio types are found mainly between 10^6 and 10^8 $M_{\odot}$. But, overall, there is no strong tendency

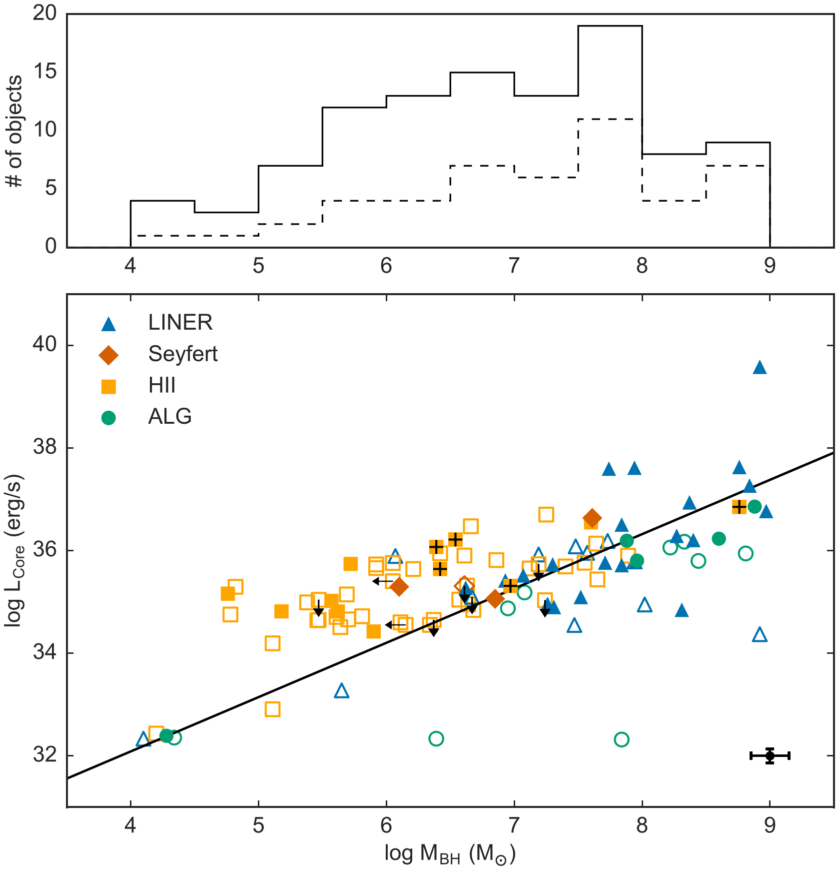

Figure 4. In the upper plot, we show the histograms of the entire sample (solid line) and of the detected/identified sources (dashed line) in bins of BH mass to estimate the detection fraction. In the lower panel, we show the radio core luminosities ($L_{\rm core}$ in erg s^{-1}) as a function of the BH masses (M$_{\odot}$) for the sample, divided per optical class (symbol and colour coded as in the legend). The jetted H II galaxies show an additional plus symbol. The filled symbols refer to the detected radio sources, while the empty symbols refer to undetected radio sources. The unidentified sources are the empty symbols with radio upper limits. The solid line represents the linear correlation found for all the jetted or active galaxies (corresponding to $M_{\rm BH} \gtrsim 10^{6.6}$ M$_{\odot}$). In the bottom-right corner, we show the typical error bars associated with the points.

for specific radio morphologies to be associated with particular radio luminosities.

5.4 Radio properties and [O III] luminosity

[O III] is a forbidden emission line, coming from the narrow-line region extending from some hundreds of pc to kpc scale. Although it is marginally dependent on orientation and obscuration (e.g. Risaliti, Salvati & Marconi 2011; Baldi et al. 2013; Dicken et al. 2014; Bisogni, Marconi & Risaliti 2017), [O III] line luminosity, $L_{\rm [O\,III]}$, is a good indicator of the bolometric AGN luminosity ($L_{\rm bol}$=3500 × $L_{\rm [O\,III]}$; Heckman et al. 2004).

Fig. 6 shows the radio core luminosity as a function of the [O III] luminosity (values taken from Ho et al. 1997) for the Palomar sample. The three optical classes generally cluster at different $L_{\rm [O\,III]}$. Seyferts have the highest [O III] luminosities (mean value 6.9 × 10^{39} erg s^{-1} with a deviation standard of 0.80), while the H II regions lie on the opposite side of the $L_{\rm [O\,III]}$ range (mean value 9.1 × 10^{37} erg s^{-1} and a deviation standard of 0.83). LINERs bridge the gap between the other two classes with intermediate $L_{\rm [O\,III]}$ (mean value 4.6 × 10^{38} erg s^{-1} and a standard deviation of 0.67). In addition, we note that LINERs scatter along a specific [O III]-radio trend. Therefore, we test the hypothesis of a linear correlation for this class. We found a tentative correlation in the form $L_{\rm [O\,III]} \propto L_{\rm core}^{0.35\pm0.20}$. The corresponding Pearson correlation coefficient (*r*-value) is 0.672, which indicates that the two luminosities for LINERs do not correlate with a probability of 8 × 10^{-4}. The galaxies with a core/core–jet morphology or a triple structure tend to be on the correlation, since they are mostly classified as LINERs. Furthermore, most of the elliptical and lenticular galaxies (unbarred galaxies in general) follow the correlation.

We test the possibility of a linear correlation which might encompass the LINERs in our sample with low-luminosity radio-loud AGN with a LINER optical spectrum, FR I radio galaxies. This hypothesis is supported by the idea of a common central engine, an ADAF disc coupled with a jet, typically attributed to LINERs (Falcke, Körding & Markoff 2004; Nemmen, Storchi-Bergmann & Eracleous 2014). Hence, we collect all the 1.5-GHz MERLIN observations of FR I radio galaxies from the literature at z<0.05 which have an angular resolution similar to our eMERLIN observations. We find six sources, which we list in Table 4. Fig. 6 shows that FR I radio galaxies extend the LINER correlation at higher luminosities. Although FR Is are more powerful than the LINERs in our sample by a factor of 10–10^3 in radio, they are still in the low-luminosity regime ($L_{\rm H\alpha}$ < 10^{40} erg s^{-1}). The linear correlation ($L_{\rm [O\,III]} \propto L_{\rm core}^{0.29\pm0.15}$) has an *r*-value of 0.766 with a probability of 3 × 10^{-6} to be fortuitous. This correlation is consistent within the errors with the one found only for the LINERs of the sample.

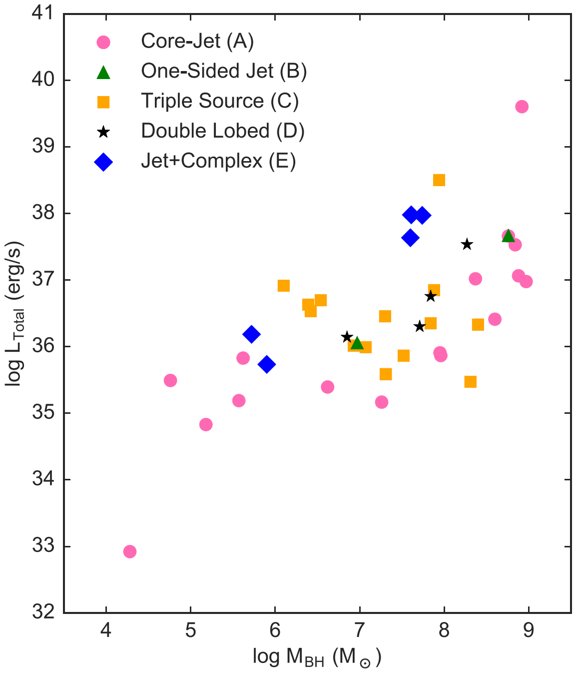

Figure 5. The total radio luminosity (L_{tot} in erg s^{-1}) as a function of the BH masses ($M_\odot$) for the sample, divided per radio morphological class A, B, C, D, and E (symbol and colour coded according to the legend).

Table 4. FR Is observed by MERLIN from literature.

Name	z	F_{core} mJy	L_{core} erg s^{-1}	$L_{[O\,III]}$ erg s^{-1}	Ref
3C 66B	0.021258	180	39.40	40.05	FR97
3C 264	0.021718	170	39.39	39.20	BA97
3C 78	0.028653	700	40.25	39.41	UN84
3C 338	0.030354	163	39.67	39.57	GI98
3C 274	0.004283	530	38.45	38.99	GO89
3C 189	0.042836	512	40.48	39.94	BO00

Notes. Column description. (1) name; (2) redshift; (3)–(4) radio core flux density and luminosity from MERLIN observations from literature data; (5) [O III] luminosity from Buttiglione et al. (2010); (6) MERLIN radio references: FR97 Fraix-Burnet, Despringre & Baudry (1997); BA97 Baum et al. (1997); UN84 Unger, Booler & Pedlar (1984); GI98 Giovannini et al. (1998); GO89 Gonzalez-Serrano et al. (1989); BO00 Bondi et al. (2000).

Seyfert galaxies typically lie below the correlation found for LINERs and are up to a factor of 100 more luminous in [O III]. Conversely, the jetted H II galaxies lie on the correlation, while the non-jetted ones (single-core component or with a complex radio morphology) fall above: less luminous in [O III] by a factor of 30 and more luminous in radio by some orders of magnitudes because of the steepness of the [O III]-radio relation. The only exception is an H II galaxy with a complex radio morphology, NGC 2342, which lies above the correlation found for LINERs. Furthermore, we include in Fig. 6 NGC 5982, which is the only ALG of the sample, for which an upper limit on the [O III] luminosity is available from Ho et al. (1997).

Using the bolometric and Eddington luminosities, we can also calculate the Eddington ratio, L_{bol}/L_{Edd}, an indicator of the accretion rate on to the SMBH (listed in Table 2). We derive the values for the detected radio sources of our sample and present them in a histogram in Fig. 7. Assuming that line emission is powered by the AGN for H II galaxies, we note that, although less luminous in line

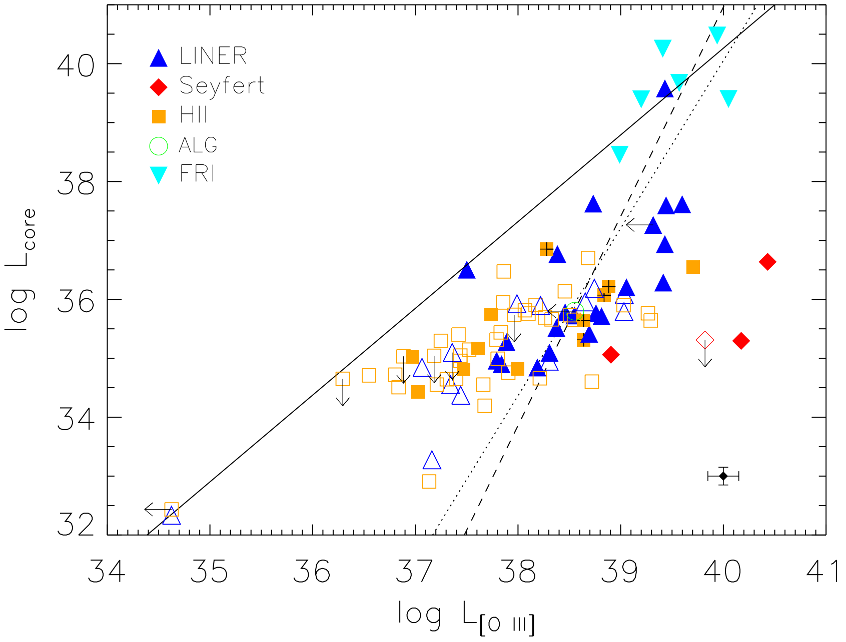

Figure 6. [O III] luminosity($L_{[O\,III]}$ in erg s^{-1}) versus radio core luminosities (L_{core} in erg s^{-1}) for the LeMMINGs sample. The different optical classes are coded (symbol and colour) in the plot according to the legend. The jetted H II galaxies show an additional plus symbol. The filled symbols refer to the detected radio sources, while the empty symbols refer to undetected radio sources. The unidentified sources are the empty symbols with radio upper limits. The FR I radio galaxies are the filled cyan downward triangles. The dotted line represents the linear correlation by fitting only the LINERs, while the dashed line represents the fit by including the FR I radio galaxies observed with MERLIN. The solid line corresponds to the [O III]–radio linear fit valid for FR I radio galaxies using VLA radio data at 5 GHz from Baldi, Capetti & Giovannini (2015). The bars in the bottom-right corner indicate the typical errors for the data points.

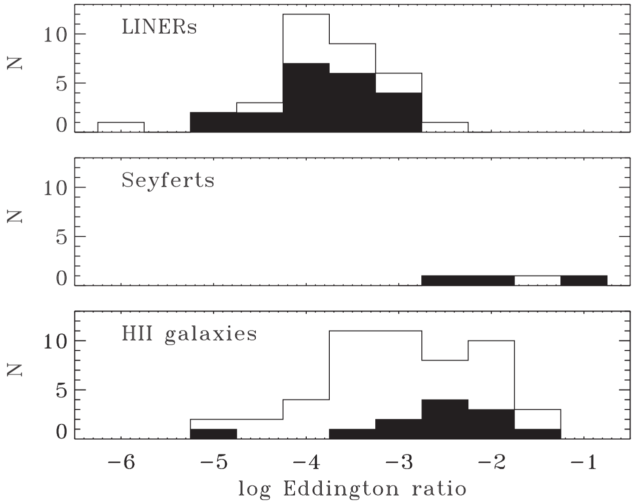

Figure 7. The Eddington ratio (ratio between the bolometric and Eddington luminosity) for the sources detected in [O III]: LINERs, Seyferts, and H II galaxies. The distribution of the identified sources is shown as a filled histogram.

emission, they have intermediate Eddington ratios between LINERs and Seyferts. The Eddington ratios of LINERs are below 10^{-3}, while the values of Seyferts are above it, e.g. the typical threshold used to separate between low- and high-accretion on to the SMBHs (Best & Heckman 2012). The H II galaxy with the lowest Eddington rate is the FR I, NGC 3665, consistent with the other LINERs. We do not find any correlation between the Eddington ratio and the radio core luminosity for our sample.

5.5 The Fundamental Plane of BH Activity in the Optical Band

An attempt at unifying all active BHs comes from the empirical FPBHA relation (Merloni et al. 2003; Falcke et al. 2004; Gültekin et al. 2009), which suggests a scale invariance in accretion and jet production. This plane relates radio and X-ray luminosities and BH mass for a sample of compact objects: from galactic BHs to AGN. By using a similar approach, Saikia et al. (2015) introduced a new FPBHA using the [O III] luminosity as a tracer of the accretion, instead of the X-ray luminosity and found an analogous correlation for active BHs.

Since BH masses and emission line luminosities are available for our sample, we plot our data by using the same parametrization expressed by Saikia et al. (2015) for the entire sample (Fig. 8). The plane identified by Saikia et al. (2015) used radio cores, detected at 15 GHz with VLA by Nagar et al. (2005) at a resolution (∼0.13 arcsec) comparable with our observations. This difference in frequency yields a difference in radio powers (in νL_ν). In fact, five sources in common with our sample have eMERLIN core luminosities, on average, lower than the VLA counterparts by a factor of ∼4. This corresponds to a spectral index between 1.5 and 15 GHz of $\alpha \sim -0.4$ ($F_\nu \sim \nu^\alpha$).

When considering our sample in the optical FPBHA, LINERs and Seyferts appear to follow the same trend, which extends to FR I radio galaxies. The jetted and non-jetted H II galaxies appear in two different areas of the plot: the former sources cluster where LINERs lie, while the latter are offset by a factor of ∼100 because of their smaller BH masses and lower [O III] luminosities. Therefore, by excluding the non-jetted H II galaxies, we find another correlation

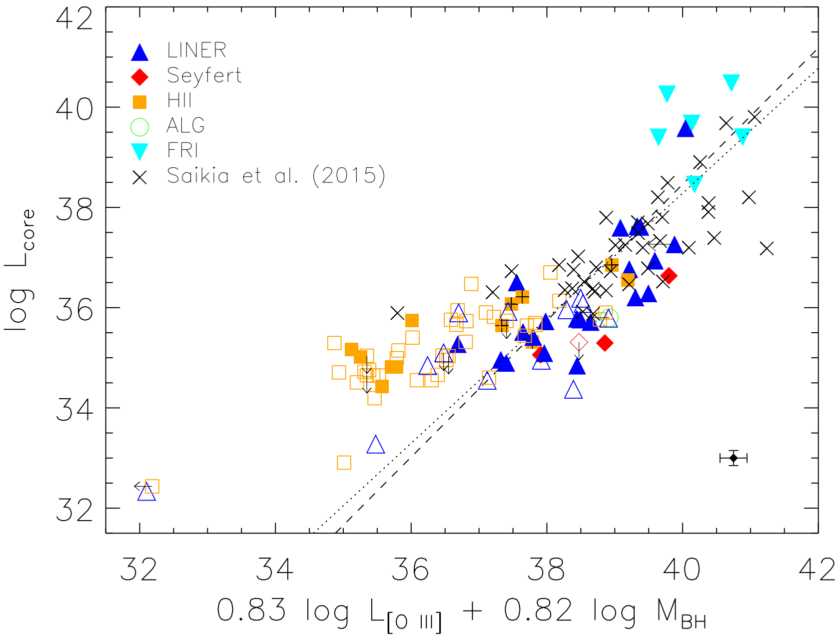

Figure 8. Projection of the FPBHA in the optical band for the LeMMINGs sample, i.e. core luminosities versus $0.83 \times \log L_{[\mathrm{O\,III}]} + 0.82 \times \log M_{\mathrm{BH}}$ with the luminosities in erg s^{-1} and BH masses in $\mathrm{M}_{\odot}$. The different classes are coded (colour and symbol) according to the legend. The jetted H II galaxies show an additional plus symbol. The filled symbols refer to the detected radio sources, while the empty symbols refer to undetected radio sources. The unidentified sources are the empty symbols with radio upper limits. The FR I radio galaxies are the filled cyan downward triangles. The black crosses are the Palomar galaxies used by Saikia, Körding & Falcke (2015) in the optical FPBHA. The dotted correlation is found for the entire sample, but excluding the non-jetted H II galaxies and the dashed correlation is obtained for LINERs and FR Is. The correlations are parametrized as expressed by Saikia et al. (2015). The bars in the bottom-right corner indicate the typical uncertainties for the data points.

which extends over four orders of magnitudes, by using the same parametrization of Saikia et al. (2015):

$$\log L_{\rm core} = (0.83 \ \log L_{\rm [O\,III]} + 0.82 \ \log M_{\rm BH})m + q$$

where $m = 1.25 \pm 0.15$ and $q = -11.6 \pm 5.9$, while Saikia et al. found $m = 1$ and $q = -3.08$. The units are erg s^{-1} for the luminosities and $M_{\odot}$ for the BH masses. The corresponding Pearson correlation coefficient (r-value) is 0.815, which indicates that the two quantities do not correlate with a probability of $<10^{-7}$. If we consider only LINERs and FR Is, we find that m=1.37 ± 0.17 and q= −16.6 ± 6.7. The corresponding r-value is 0.847 with a probability of $<10^{-7}$ of being a fortuitous correlation. This correlation is still consistent with that found for the entire sample (excluding the non-jetted H II galaxies) within the errors. Furthermore, most of the elliptical and lenticular galaxies lie on the correlation.

Although radio core luminosity, BH mass and [O III] luminosity are found to correlate for LINERs, the scatter in the optical FPBHA is larger (∼1 dex) than those found in the other correlations with $L_{\rm core}$ (0.6–0.8 dex). However, the FPBHA is not driven by any stronger dependence of one of the three quantities which establish the Fundamental Plane. This confirms the validity of the FPBHA at least for the LINERs of our sample. The small number of Seyferts and jetted H II galaxies in our sample limits an analogous analysis performed for these classes. For the non-jetted H II galaxies, which induce the break in the optical FPBHA at low radio powers, we have verified that assigning a possible core luminosities via the radio–$M_{\rm BH}$ relation found at larger BH masses, these sources nicely line up on the Fundamental Plane. This test further corroborates our suggestion that the radio emission in the non-jetted H II galaxies is mostly powered by SF, because otherwise we would not expect these galaxies to necessarily depart from the optical FPBHA.

In general, in the optical FPBHA, we also note that the three optical classes slightly scatter in radio luminosities along the correlation, by decreasing $L_{\rm core}$ in the order: H II galaxies, Seyferts, and LINERs.

6 DISCUSSION

This eMERLIN radio legacy survey represents the deepest radio study of the Palomar sample to date, reaching rms of ∼70μJy. Furthermore, the LeMMINGs survey differs from previous studies of the Palomar sample, as we have deliberately observed all the optical classes including the galaxies which are not classified as AGN based on the emission line ratios, i.e. H II galaxies and ALGs. Here we discuss the results of 103 radio sources, randomly selected from the full LeMMINGs ‘shallow’ sample (280 sources).

The total detection rate (47/103, ∼46 per cent) is consistent with previous VLA/VLBA observations of the Palomar sample (see Ho 2008 for a review), which mostly focused on LINERs and Seyferts which are typically the brightest radio sources. For 40 per cent (41/103) of the sample the radio emission can be associated with the optical galaxy centre, suggesting a relation with the active SMBH.

More than half of the sources, classified as active based on their emission-line ratios, show a compact radio source and/or jet structures. Half of the sources which are not classified as powered by an AGN based on the BPT diagrams show jetted radio appearances, a possible sign of active SMBHs. Half of the detected sources show clear jetted morphologies (triple sources, twin jets, double lobed, one-sided jets, 20/41) and five sources show a complex structure which might hide a possible jet and diffuse SF.

The most frequent radio class observed in our sample is the core/core–jet morphology (16/41). The nature of these unresolved radio components, whether an unresolved radio jet base or an SF nuclear region on the scale of <100 pc, can be revealed by using further diagnostics such as [O III] luminosities and BH masses in absence of clear jet-like structures. We will discuss the core origin and the results of each optical class in the following sub-sections.

6.1 Liners

LINERs show the highest number of radio detections in the Palomar sample and are hosted by elliptical, lenticular, and spiral galaxies. The detection rate (22/34; 64 per cent) is slightly higher than a previous radio survey of the Palomar sample (∼44 per cent; Ho 2008). The eMERLIN observations reveal that LINERs are associated with single radio core components (8/21), triple radio sources which turn into twin jets at lower resolutions (9/21), double-lobed structures (3/21), and complex morphologies (1/21). Only one object lacks a core identification. Their radio luminosities are on average higher than Seyferts and H II galaxies by a factor of 2–3.

Although the typical emission line ratios of LINERs can be reproduced by an AGN, shocks, or post-AGB stars (Allen et al. 2008; Sarzi et al. 2010; Capetti & Baldi 2011; Singh et al. 2013), several factors point to an AGN origin of their radio emission:

(i) They are mostly associated with symmetric jets extended on ∼0.05–1.7 kpc-scales. It is unlikely that SF can reproduce such radio morphologies and radio luminosities, since SF typically dominates over the AGN emission below 10^{34} erg s^{-1} in the sub-mJy regime (Bonzini et al. 2013; Padovani 2016).

(ii) The radio jets are brightened closer to the cores, similar to the edge-darkened morphologies of FR Is. These characteristics suggest that the jets are probably launched collimated and relativistically, and their bulk speed decreases along the jet propagation axis, similar to what is seen in nearby low-luminosity radio galaxies (Morganti et al. 1987; Parma et al. 1987; Falcke et al. 2000; Giovannini et al. 2005).

(iii) Radio core luminosities correlate with the BH masses, highlighting the role of the SMBHs in the production of radio emission in this class.

(iv) The highest radio core flux densities are associated with the LINERs, pointing to high brightness temperatures: at eMERLIN sensitivity and resolution, six LINERs have bright radio cores (> 5 mJy) with brightness temperatures $>10^6$ K, indicative of synchrotron emission from relativistic jets. High brightness temperatures ($>10^8$ K) of radio cores detected with the VLBA for LINERs (Falcke et al. 2000) point to the same interpretation, which is analogous to luminous radio-loud AGN.

LINERs are associated with different types of host galaxy, but with the largest BH masses ($>10^7$ $M_{\odot}$) and typically accrete at low rates ($<10^{-3}$ Eddington rate). The most accepted scenario for this class is a radiatively inefficient disc model, usually as an advection-dominated, geometrically thick, optically thin accretion disc (ADAF; see review from Narayan et al. 1998; Narayan & McClintock 2008). Since LINERs tend to be radio louder than other optical classes (Capetti & Balmaverde 2006; Kharb et al. 2012), this effect can be ascribed to an ADAF disc which is efficient at producing jets, as suggested by theoretical studies including analytical work (e.g. Narayan & Yi 1994; Meier 2001; Nemmen et al. 2007; Begelman 2012) and numerical simulations (e.g. Tchekhovskoy, Narayan & McKinney 2011; McKinney, Tchekhovskoy & Blandford 2012; Yuan, Bu & Wu 2012).

The combination of a jet and an ADAF disc (JDAF; Falcke et al. 2004) is also attributed to FR I radio galaxies. We find that LINERs and FR Is follow similar correlations in the [O III]-radio plane and in the optical FPBHA. Hence, LINERs share the same central engine as FR Is and appear to be scaled-down versions of FR Is. This result is analogous to what has been found for low-luminosity radio-loud LINERs in early-type galaxies (e.g. Balmaverde & Capetti 2006).

6.2 Seyferts

Only four Seyferts are present in this sample, based on the revised BPT diagrams. Seyferts are mostly found in spiral galaxies and are all detected at 1.5 GHz. One source (NGC 5273, a lenticular galaxy) does not show a radio core, but a ring of radio emission is probably associated with SF. The radio morphologies observed for the three detected and identified Seyferts are: a triple source, a double-lobed source, and a complex morphology with a possible jet, all suggestive of a jetted structure on a scale of ∼50–400 pc. Our detection rate (4/4) is higher than previous radio surveys of the Palomar sample for this class of sources (∼47 per cent; Ho 2008). Although the small number of Seyferts in our sample limits the interpretation of our results about this class, we can, however, highlight their properties as compared to the LINERs.

The high emission line ratios typical of Seyferts require photoionization from an AGN (Kewley et al. 2006). However, the question remains as to whether these active SMBHs or SF can account for the observed radio properties of Seyferts. In our survey, the jets of Seyferts appear to be more edge-brightened than LINERs and similar to the radio morphologies of local Seyferts (e.g. Kukula et al. 1993, 1995; Gallimore et al. 1996; Morganti et al. 1999; Wrobel 2000; Kharb et al. 2006). For the three detected Seyferts, diffuse radio structures appear in low-resolution images resembling radio lobes, which are observed to be more common in Seyfert galaxies than in LINERs (Baum et al. 1993; Gallimore et al. 2006). Lobe structures indicate that the jets are not necessarily relativistic nearer to the core and they eventually terminate in a bow shock which ploughs into the surrounding interstellar medium, resulting in a bubble-like structure. An AGN-driven scenario can explain pc-kpc scale lobes, but we cannot rule out the possibility that starburst super-winds cause the observed morphologies (Pedlar, Unger & Dyson 1985; Heckman, Lehnert & Armus 1993; Colbert et al. 1996).

The [O III] line excess observed for our Seyferts with respect to the [O III]-radio correlation established for LINERs (Fig. 6) invokes the presence of a brighter ionizing source at the centre of these galaxies than an ADAF disc. The high [O III] luminosities, a proxy of the AGN bolometric power, lead to high accretion rates ($>10^{-3}$ Eddington rate), providing further evidence for a different central engine from that present in LINERs. A thin disc (standard disc; Shakura & Sunyaev 1973) is commonly used to account for the multiband properties of Seyferts. These disc systems are less efficient in launching relativistic radio jets than ADAF discs, but are still able to produce jets, though less collimated and slower than those in LINERs (Yuan & Narayan 2014 and references therein). In fact, the Seyferts in our sample roughly follow the optical FPBHA traced by the LINERs, possibly suggesting a comparable jet-disc symbiosis. The large fraction of Seyferts associated with jets in our sample and in previous studies of local Seyferts suggests that low-power Seyferts exist in an intermediate regime between the jet-ADAF-dominated LINERs and the near-Eddington luminous QSOs, which are typically radio-quiet (Ho 2002, 2008; Kauffmann, Heckman & Best 2008; Sikora, Stawarz & Lasota 2008). This intermediate stage could be a consequence of an evolutionary transition of disc physics from an ADAF to a standard disc by increasing the accretion rate and/or disc radiative efficiency (Trippe 2014). However, a substantial paucity of radio studies of QSOs, which are typically at higher redshifts, in literature, could also affect this observational evidence. In fact, generally, the nature of the radio emission in radio-quiet AGN, whether a scaled-down version of the radio-loud jet (Barvainis, Lonsdale & Antonucci 1996; Gallimore et al. 2006), coronal emission from magnetic activity above the accretion disc as an outflow (Field & Rogers 1993; Laor & Behar 2008; Behar et al. 2015), or thermal free–free emission/absorption (Gallimore, Baum & O'Dea 2004) still remains to be fully understood.

6.3 Absorption line galaxies

As discussed in the Introduction section, although ALGs lack evidence of BH activity, they may still hide an active BH. In our sample we detected radio emission associated with the innermost region of the galaxy for ∼36 per cent (5/14) of the ALGs. They appear as a single radio core for four cases and a triple source for one galaxy. The ALGs in our survey are elliptical or lenticular galaxies, which harbour SMBHs with masses larger than 10^8 $M_{\odot}$, typical of $M_{\rm BH}$ limits set for radio-loud AGN (Chiaberge & Marconi 2011). The radio luminosities for these sources are similar to LINERs. Only NGC 147 has an exceptionally low BH mass of 1.9×10^4 $M_{\odot}$ in a dwarf elliptical galaxy associated with the lowest radio luminosity ($\sim10^{32}$ erg s^{-1}) of the sample.

The lack of availability of detected emission lines for our ALGs prevents further analysis on either AGN bolometric luminosities or SF rates. Therefore, a complementary multiband study of these galaxies is needed first to study whether they hide active SMBHs. A cross-matching of optical SDSS (Stoughton et al. 2002) and radio FIRST (Becker, White & Helfand 1995) data of local radio galaxies reveals that no-emission line radio sources (slightly higher in radio luminosities, 10^{39}–10^{41} erg s^{-1}, than our sample) mostly show host and nuclear properties similar to LINERs (Baldi & Capetti 2010) and show extended radio structures for 27 per cent of the sample. In summary, our high-resolution radio observations and previous studies argue for the presence of active SMBHs associated with radio jets in, at least, one third of the ALGs.

The lack of evidence of an active SMBH in a large fraction of ALGs might be interpreted within a nuclear recurrence scenario due to an intermittent accretion phenomenon (Reynolds 1997; Czerny et al. 2009). To account for the large fraction of the undetected and the five detected ALGs, the duration of the active phase must cover a wide range of values with short active periods favoured over the longer ones. Assuming a jet bulk speed of $\sim0.02c$ typical for low-power radio galaxies (Massaglia et al. 2016), the most extended radio jet detected for an ALG (∼700pc for NGC 6702) in our sample sets a limit on the age of $\sim1.3 \times 10^5$ yr. Therefore, this value infers an upper limit on the radio activity of ALGs, which is consistent with the typical duty cycles of radio AGN, i.e. 10^4–10^8 yr estimated at different wavelengths (see Morganti 2017 for a review). This recurrent nuclear activity might account for their high core dominance, possibly interpreted as a sign of a young radio age.

6.4 H II galaxies

H II galaxies are SF-dominated nuclei, based on the emission line ratios, but their classification does not preclude the possibility of the presence of a weak AGN at their galaxy centre. The relatively few available radio observations of H II galaxies and single-source studies generally lead to low detection rates (∼7.5 per cent; Ulvestad & Ho 2002 and references therein). We detected radio emission for 31 per cent (16/51) of the H II sample. For 12 H II galaxies, five sources show jetted structures (one-sided and twin jets), four show single core detections and three show complex morphologies. However, for four sources a clear radio core component is missing from the eMERLIN maps. The radio luminosities of H II galaxies are, on average, lower than those of LINERs by a factor of ∼2. The radio structure sizes are of order 50–500 pc.

Two different types of H II galaxies emerge from our eMERLIN survey: jetted and non-jetted. The H II galaxies with jetted morphologies (NGC 972, NGC 3665, UGC 3828, NGC 7798, and UGC 4028), possibly indicating the presence of an AGN, are found associated with BH masses larger than 10^6 $M_\odot$. The emission line ratios of these sources do not differ from the other H II galaxies in the BPT diagrams (see Fig. 2). As further evidence of a possible AGN, these five sources lie on the [O III]–radio correlation found for LINERs and on the optical FPBHA. One source, NGC 3665, shows an FR I radio morphology at VLA resolution (Parma et al. 1986). Two sources show one-sided jets, which might indicate the Doppler boosting effect of relativistic jets. This group of H II galaxies probably hosts a weak AGN whose optical signature has simply been overpowered by the dominant optical signal from nuclear SF. Their hidden LLAGNs appear more consistent with a sub-Eddington LINER rather than a more luminous Seyfert. In fact, the radio jets of this group are morphologically similar (e.g. core-brightened) to the LINERs in our sample and roughly follow the relations traced by the LINERs.

Conversely, the situation appears different for the remaining seven H II galaxies (NGC 278, NGC 3198, NGC 3938, NGC 3432, NGC 6946, NGC 2342, and NGC 3430), which do not show clear jet structures. The BH masses of these sources are below 10^6 $M_\odot$ and they show clear [O III] line deficit of a factor of ∼30 and a large radio excess with respect to the [O III]–radio correlation found for LINERs. This result seems to follow the idea that the low-radiation field generated by SF can account for both their observed radio and emission line properties. The only exception to this picture is NGC 2342, which has a complex radio morphology, has a BH mass of 4×10^7 $M_\odot$, lies on the optical FPBHA, and has the highest [O III] luminosity of all detected H II galaxies.

For non-jetted H II galaxies, we consider the case of non-thermal SF to be the primary origin of their radio counterparts (an assumption which is justified at 20 cm where most of the radio emission is of a non-thermal nature). We calculate the expected nuclear supernova rates $\nu_{\rm SN}$ assuming that the total radio emission is dominated by cosmic rays accelerated in supernova remnants (SNRs), using the formula from Condon (1992), $L_{\rm radio}/(1.4 \times 10^{38}\,{\rm erg\,s^{-1}}) = 11 \times (\nu_{\rm SN}/{\rm yr^{-1}})$. The calculated supernova rates correspond to 2×10^{-5}–$6 \times 10^{-4}\,{\rm yr^{-1}}$ in the central core region of ∼50 pc. These values are roughly similar to the supernova rates expected in M82 (15–30 $\rm yr^{-1}$ for the entire galaxy; Muxlow et al. 1994; Fenech et al. 2008) extrapolated to a region 100 times smaller, or $(3–6) \times 10^{-4}\,{\rm yr^{-1}}$. Furthermore, assuming that a fraction of radio emission comes from thermal stellar processes, the predicted free–free radio emission expected from the H α luminosities ($10^{37.7\,-\,38.8}\,{\rm erg\,s^{-1}}$; Ho et al. 1997) due to thermal stellar emission (Ulvestad, Wilson & Sramek 1981; Filho, Barthel & Ho 2002) would be conservatively higher within a factor of ∼10 than the measured radio luminosities of AGN-dominated sources, i.e. Seyferts and LINERs. This would correspond to SF rates of 4×10^{-4}–$5 \times 10^{-3}\,M_\odot\,{\rm yr^{-1}}$ in the central radio core, derived from the H α luminosities (assuming a Salpeter mass function for 0.1–100 $M_\odot$ and solar metallicity; Kennicutt 1998). In conclusion, all these calculations favour an SF origin of the radio emission, possibly from a pc-scale nuclear starburst, for the non-jetted H II galaxies.

6.5 Any clear star-forming galaxies?

Considering the identified galaxies of our sample which do not show clear jetted morphologies, we do not find any evidence for radio sources which generally resemble diffuse star-forming galaxies (Muxlow et al. 2010; Herrero-Illana et al. 2017; Murphy et al. 2018), based only on the radio properties. However, single radio components might hide unresolved nuclear star-bursts and complex radio morphologies might also be due to the presence of star-forming regions, possibly induced by radio jets (see e.g. NGC 2273 and NGC 2655). The only cases where the radio-optical results support for a possible star-forming scenario are the non-jetted H II galaxies.

For the unidentified galaxies, the nature of the detected radio emission is unclear. However, two objects (NGC 4013 and NGC 5273) clearly show circum-nuclear radio-emitting rings, which were not seen before at lower resolution. These two sources are the most evident cases of SF in our sample, based on their radio morphology.

For the objects further than 4 Mpc, which are the majority of the sample, the spatial frequencies covered by eMERLIN are suited to detect compact SNR (Westcott et al. 2017). However, the snapshot imaging technique used in this survey is not appropriate for detecting diffuse, low-brightness radio emission ($<10^5$ K), typical of old SNR. Conversely, young SNR and H II regions could be detected since they are more compact and brighter. At distances less than ∼4 Mpc, VLA data are required to study old SNR (> 400–500 yr), which would be resolved out by the eMERLIN baselines. Within this distance, only one galaxy (NGC 147) has been detected in our survey, showing a single radio component. The addition of shorter spacing VLA data to this project will enhance the ability to detect more diffuse lower surface brightness emission from SF products.

6.6 Host galaxies

In this sample, we find that half of the early-type galaxies (ellipticals and lenticulars) host a radio-emitting active SMBH, while this occurs only in one third of the late-type galaxies (spirals and irregulars). More precisely, our radio survey detects ∼60 per cent of galaxies earlier than Sb. The detection rate of radio AGN dramatically drops towards later Hubble types: we detect radio cores for 22 per cent of Sc–Sd galaxies only. Our results agree with previous radio studies on the Palomar sample (Ho & Ulvestad 2001; Ulvestad & Ho 2001a; Nagar et al. 2005; Ho 2008), which found flat-spectrum radio cores predominantly in massive early-type galaxies (Sadler et al. 1989; Wrobel & Heeschen 1991; Capetti et al. 2009; Miller et al. 2009; Nyland et al. 2016).

The LeMMINGs survey detects nuclear activity, predominantly in the form of jet morphologies, for SMBHs more massive than 10^6 $M_\odot$ but the detection fraction drastically decreases below 10^7 $M_\odot$. We also find that the core luminosities of the jetted galaxies correlate with the BH mass. These results confirm past radio continuum studies that showed that radio brightness in galaxies is a strong function of the host mass or BH mass, proportional to $M_{\rm BH}^{\alpha}$ (with a broad range of α values, typically $1 - 2$; Laor 2000; Nagar et al. 2002a; Best et al. 2005a; Mauch & Sadler 2007). Consequently, this dependence also explains the different detection rates between early-type and late-type galaxies (Decarli et al. 2007; Gallo et al. 2008), due to their different BH masses.

The association between radio detection, host type, and BH mass is an indirect consequence of a more fundamental relationship between radio luminosity and optical bulge luminosity (or mass) (Ho 2002; Nagar et al. 2002a). Massive elliptical galaxies, which typically host large SMBHs, are more efficient in producing radio emission than less massive spiral galaxies and, thus, turn out to be radio-loud for $M_{\rm BH} > 10^8$ M$_\odot$ (Chiaberge & Marconi 2011).

7 SUMMARY AND CONCLUSIONS

This paper presents the first release of radio data and results from the eMERLIN legacy survey, LeMMINGs, aimed at studying a sample of nearby (active and quiescent) galaxies. We observed 103 sources from the Palomar sample (Ho et al. 1997) with $\delta > 20°$ (one third of the entire legacy program) at 1.5 GHz with the eMERLIN array, reaching a sensitivity of ~70μJy and an angular resolution of ~150 mas. The remaining radio images of this survey and the multiband study of the sample will be released and addressed in forthcoming papers.

First, we have updated the optical spectroscopic classification of the sample based on the state-of-the-art diagrams. We used diagnostic schemes presented in Kewley et al. (2006) and Buttiglione et al. (2010) to classify the sources as LINERs, Seyferts, H II galaxies, and ALGs (34:4:51:14).

Our radio survey detected significant radio emission in the innermost region of the galaxies (0.73 arcmin^2) for 47 objects out of 103 (~46 per cent) with flux densities $\gtrsim$0.2 mJy. For 41 sources we identified the radio core within the structure, associated with the optical galaxy centre. We resolved parsec-scale radio structures with a broad variety of morphologies: core/core–jet, one-sided jet, triple sources, twin jets, double-lobed, and complex shapes with extents of 40–1700 pc. It is important to stress that such detected structures mostly appeared as compact in previous VLA observations. The jetted radio sources (25/41) are more common than single cores (16/41). While the jetted morphologies, which are associated with galaxies with $M_{\rm BH} > 10^6$ M$_\odot$, are interpreted as a possible sign of an active SMBH, more caution is needed to interpret the single unresolved components associated with no jets, whether they are a simple unresolved jet base or star-forming cores.

The radio core powers (10^{32}–10^{40} erg s^{-1}) are lower than those measured from previous radio surveys of the Palomar sample, 10^{35} erg s^{-1} (Nagar et al. 2005; Filho et al. 2006), due to higher sensitivity (by a factor of ~4) and higher angular resolution (by a factor of 2–10, depending on frequency) of eMERLIN. The most common detected radio galaxies are LINERs and early-type galaxies, typically showing single cores or jetted morphologies. Seyferts show more edge-brightened radio morphologies than those of LINERs and have intermediate luminosities. ALGs mostly show single cores and are highly core-dominated. H II galaxies lie on the lower side of the radio luminosity range and show both jetted and non-jetted radio morphologies for the detected H II galaxies. The radio cores typically contribute to ~26 per cent of the total detected emission. Concerning the host type, half of the early-type galaxies and one third of the late-type galaxies are detected in our survey.

To investigate the nature of the radio emission, we look for empirical correlations between core luminosities and BH masses and [O III] line luminosity, all good diagnostics of the SMBH activity. We find that the core power, indicative of the jet energetics, correlates with $M_{\rm BH}$ for masses $\gtrsim 10^7$ M$_\odot$, but a clear break emerges at lower masses. Ellipticals, lenticulars, and radio jetted galaxies lie on the correlation. This result is possibly a consequence of a fundamental link between SMBH activity and radio jet production. By assuming a hierarchical galaxy evolution, massive galaxies (typically early-type) nurse their SMBHs through mergers, which grow in mass and evolve to low-Eddington ratios (Volonteri et al. 2013). Massive SMBHs provide the adequate conditions for supporting the launch of a jet (Falcke et al. 2004), which accounts for the empirical radio–$M_{\rm BH}$ relation. Conversely, for SMBHs with masses $\lesssim 10^6$ M$_\odot$, which are generally found in less-massive late-type galaxies, the radio detection rate decreases in our sample. It is likely that a larger contribution from SF in the radio band might account for the flattening of the radio-$M_{\rm BH}$ relation.

[O III] line luminosity is a good indicator of AGN bolometric luminosity, and is found to broadly correlate with radio core power. However, the radio emission efficiency, i.e. the fraction of the radio emission produced with respect to the bolometric luminosity of the AGN, is different for each optical class. This result is in agreement with previous multiband studies for different classes of LLAGNs and extends to more powerful radio galaxies (e.g. Chiaberge, Capetti & Celotti 1999; Nagar, Falcke & Wilson 2005; Balmaverde & Capetti 2006; Balmaverde, Capetti & Grandi 2006; Panessa et al. 2007; Hardcastle, Evans & Croston 2009; Baldi et al. 2010; de Gasperin et al. 2011; Panessa & Giroletti 2013; Asmus et al. 2015; Mingo et al. 2016). The radio properties and the location in the radio–[O III] plane attribute different nuclear characteristics, resulting from fundamentally different BH physics, which we discuss further below.

(i) **LINERs**. Our eMERLIN observations show a prevalence of jetted structures associated with LINERs (13/21). Furthermore, we find evidence of an affinity between the LINERs in our sample and FR I radio galaxies, as they follow similar correlations in the [O III]–radio plane and in the optical FPBHA. This result points to a common origin of the nuclear emission: the non-thermal synchrotron emission from a jet, which dominates the spectral output of the AGN at different wavelengths (Körding et al. 2008). The low Eddington rate of LINERs and their similarities with FR Is suggest that a radiatively inefficient disc, probably an ADAF disc, which also aids in the jet production due to its funnel-like structure and poloidal magnetic field, is the most viable accretion mode at the centre of LINERs. These results are in agreement with previous multiband studies which proposed a jet+ADAF model (JDAF; Falcke et al. 2004) (Balmaverde & Capetti 2006; Balmaverde et al. 2006; Panessa et al. 2007; Baldi & Capetti 2009) for LINER-like LLAGNs, which also accounts for the inverse correlation between their Eddington rate and radio-loudness (Ho 2002, 2008).

(ii) **Seyferts**. Although this class is limited in number in our sample, we find that Seyferts are associated with radio jets (3/4), which appear more edge-brightened than those observed in LINERs. This type of morphology points to jet bulk speeds lower than those inferred from the core-brightened jets in LINERs. The high emission line ratios, large [O III] luminosities, and the large [O III] excess with respect to the [O III]-radio core correlation found for the synchrotron-dominated LINERs indicate a different central engine for Seyferts: a radiatively efficient disc, accreting at higher rates than in LINERs. Our results emphasize the increasing observational evidence that kpc-scale jets are more commonly observed in local Seyferts than in more luminous Seyferts and QSOs. As also supported by the shared optical FPBHA with LINERs, low-power Seyferts are in an intermediate position between the jetted LINERs and the radio-quiet near-Eddington QSOs (Balick & Heckman 1982; Ho 2002, 2008; Busch et al. 2014), suggesting a continuum of radio properties of LLAGNs (Kharb et al. 2014). This intermediate stage is probably a consequence of a luminosity/accretion dependence on the jet efficiency (Trippe 2014) from a thick to thin accretion disc (Donea & Biermann 1996, 2002; Markoff, Nowak & Wilms 2005; King et al. 2011).

(iii) **H II galaxies** and ALGs are a mixed population of galaxies which host either weakly active or silent SMBHs, and may be overwhelmed by SF. On one hand, eMERLIN observations of H II galaxies reveal a sub-population of jetted sources (5/51), which has $M_{\rm BH} > 10^6$ $M_{\odot}$, follows the LINERs in the optical FPBHA: these sources are possibly powered by weakly active SMBHs, similar to LINERs. The remaining non-jetted H II galaxies better reconcile with an SF scenario. On the other hand, the detected ALGs (5/14) are associated with core–jet/triple radio morphologies and are commonly hosted in massive ellipticals, similar to LINERs. Furthermore, for ALGs, a possible radio nuclear recurrence scenario might reconcile with the occasional lack of activity observed in massive early-type galaxies, due to general duty cycles of nuclear activity (Morganti 2017).

In conclusion, to a first approximation, AGN with different BH masses and hosted in different galaxies can produce jets with similar power, size, and morphology (Gendre et al. 2013; Baldi, Capetti & Massaro 2018). This result suggests that (currently) directly unobservable quantities, such as BH spin, magnetic field strength, and accretion rotation, might play an important role in the jet-launching mechanism (Garofalo, Evans & Sambruna 2010; Tchekhovskoy & McKinney 2012; Garofalo 2013), regardless of the AGN and host properties. In addition, in our survey, independent of their optical classes, the active galaxies and the jetted H II galaxies appear to broadly follow a similar correlation in the optical FPBHA, stretching their luminosities up to FR I radio galaxies. Therefore, in the low-luminosity regime, the physical process which regulates the conversion of the accretion flow into radiative and kinetic jet energy could be universal across the entire SMBH mass scale and for different optical classes. Such a process does not necessarily require the same disc–jet coupling since the classes are differently powered. Instead, it points to a common scaling relation in terms of BH properties (mass, spin, disc-BH alignment, and co-rotation), accretion, and jet production, which are distinct for each AGN class, but become similar when all are properly combined in the FPBHA, as validated by magnetic–hydrodynamic simulations (Heinz & Sunyaev 2003). However, we should point out that a slight separation of the different optical classes is still evident across the optical FPBHA (with the Seyferts at lower radio luminosities than LINERs), which was not observed in previous works at lower VLA resolution. Resolving the parsec-scale jet base, thanks to eMERLIN, has helped to bring this effect in the Fundamental Plane to light. The origin of this stratification in the optical FPBHA might be still reminiscent of the different accretion modes for each optical class.

The LeMMINGs project has uncovered new radio active SMBHs in the local Universe, which were not detected and identified before. This discovery is fundamental for conducting a fair census of the local BH population and to provide robust constraints on cosmological galaxy evolution models (Shankar 2009). The local BH demographics and the study of the BH activity are currently still limited to a few single-band observations, circumscribed to small samples. The LeMMINGs legacy survey will address these topics with a multiband approach applied to a complete sample, pushing the low end of the radio luminosity function. In fact, further eMERLIN observations at *C* band (5 GHz) will, for the first time, extend the radio luminosity function of the local Universe down to 10 times the luminosity of Sgr A* and help to discriminate SF from genuine AGN activity. Furthermore, complementary data, which include optical (*HST*), X-ray (*Chandra*), and infrared (*Spitzer*) band, will unveil the origin of the parsec-scale radio emission and properties of the central engines of the local LLAGN population.

ACKNOWLEDGEMENTS

The authors thank the referee for a quick publication and the helpful comments from A. Laor and A. Capetti for the interpretation of the results. RDB and IMcH acknowledge the support of STFC under grant [ST/M001326/1] and IMcH thanks the Royal Society for the award of a Royal Society Leverhulme Trust Senior Research Fellowship. We acknowledge funding from the University of Southampton for a Mayflower studentship afforded to DW. EB and JW acknowledge support from the UK's Science and Technology Facilities Council [grant number ST/M503514/1] and [grant number ST/M001008/1], respectively. CGM acknowledges financial support from STFC. JHK acknowledges financial support from the European Union's Horizon 2020 research and innovation programme under Marie Skłodowska-Curie grant agreement No. 721463 to the SUNDIAL ITN network, and from the Spanish Ministry of Economy and Competitiveness (MINECO) under grant number AYA2016-76219-P. DMF wishes to acknowledge funding from an STFC Q10 consolidated grant [ST/M001334/1]. BTD acknowledges support from a Spanish postdoctoral fellowship 'Ayudas para la atracción del talento investigador. Modalidad 2: jóvenes investigadores, financiadas por la Comunidad de Madrid' under grant number 2016-T2/TIC-2039. FP has received funding from the European Union's Horizon 2020 Programme under the AHEAD project (grant agreement No. 654215). We also acknowledge the Jodrell Bank Centre for Astrophysics, which is funded by the STFC. eMERLIN and formerly MERLIN is a National Facility operated by the University of Manchester at Jodrell Bank Observatory on behalf of STFC. This publication has received funding from the European Union's Horizon 2020 research and innovation programme under grant agreement No. 730562 [RadioNet].

REFERENCES

Allen M. G., Groves B. A., Dopita M. A., Sutherland R. S., Kewley L. J., 2008, ApJS, 178, 20
Anderson J. M., Ulvestad J. S., Ho L. C., 2004, ApJ, 603, 42
Annibali F., Bressan A., Rampazzo R., Zeilinger W. W., Vega O., Panuzzo P., 2010, A&A, 519, A40
Argo M., 2015, preprint (arXiv:1502.04936)
Asmus D., Gandhi P., Hönig S. F., Smette A., Duschl W. J., 2015, MNRAS, 454, 766
Baldi R. D., Capetti A., 2009, A&A, 508, 603
Baldi R. D., Capetti A., 2010, A&A, 519, A48
Baldi R. D. et al., 2010, ApJ, 725, 2426
Baldi R. D., Capetti A., Buttiglione S., Chiaberge M., Celotti A., 2013, A&A, 560, A81
Baldi R. D., Capetti A., Giovannini G., 2015, A&A, 576, A38
Baldi R. D., Capetti A., Massaro F., 2018, A&A, 609, A1
Baldwin J. A., Phillips M. M., Terlevich R., 1981, PASP, 93, 5
Balick B., Heckman T. M., 1982, ARA&A, 20, 431
Balmaverde B., Capetti A., 2006, A&A, 447, 97
Balmaverde B., Capetti A., 2013, A&A, 549, A144
Balmaverde B., Capetti A., 2014, A&A, 563, A119
Balmaverde B., Capetti A., Grandi P., 2006, A&A, 451, 35
Barausse E., Shankar F., Bernardi M., Dubois Y., Sheth R. K., 2017, MNRAS, 468, 4782
Barvainis R., Lonsdale C., Antonucci R., 1996, AJ, 111, 1431
Baum S. A., O'Dea C. P., Dallacassa D., de Bruyn A. G., Pedlar A., 1993, ApJ, 419, 553
Baum S. A. et al., 1997, ApJ, 483, 178
Beasley A. J., Gordon D., Peck A. B., Petrov L., MacMillan D. S., Fomalont E. B., Ma C., 2002, ApJS, 141, 13
Becker R. H., White R. L., Helfand D. J., 1995, ApJ, 450, 559
Beckwith K., Hawley J. F., Krolik J. H., 2008, ApJ, 678, 1180

Begelman M. C., 2012, MNRAS, 420, 2912

Begelman M. C., Blandford R. D., Rees M. J., 1984, Rev. Mod. Phys., 56, 255

Behar E., Baldi R. D., Laor A., Horesh A., Stevens J., Tzioumis T., 2015, MNRAS, 451, 517

Best P. N., Heckman T. M., 2012, MNRAS, 421, 1569

Best P. N., Kauffmann G., Heckman T. M., Brinchmann J., Charlot S., Ivezić Ž., White S. D. M., 2005a, MNRAS, 362, 25

Best P. N., Kauffmann G., Heckman T. M., Ivezić Ž., 2005b, MNRAS, 362, 9

Beswick R., Argo M. K., Evans R., McHardy I., Williams D. R. A., Westcott J., 2014, Proc. 12th Eur. VLBI Network Symp. Users Meeting (EVN 2014), 7–10 October 2014, Cagliari, Italy, p. 10

Bisogni S., Marconi A., Risaliti G., 2017, MNRAS, 464, 385

Blundell K. M., 2003, The Observatory, 47, 593

Blundell K. M., Rawlings S., 2001, ApJ, 562, L5

Bonchi A., La Franca F., Melini G., Bongiorno A., Fiore F., 2013, MNRAS, 429, 1970

Bondi M., Parma P., de Ruiter H., Fanti R., Laing R. A., Fomalont E. B., 2000, MNRAS, 314, 11

Bonzini M., Padovani P., Mainieri V., Kellermann K. I., Miller N., Rosati P., Tozzi P., Vattakunnel S., 2013, MNRAS, 436, 3759

Bower G. A., 1992, PhD thesis, Michigan Univ., Ann Arbor.

Brown R. H., Hazard C., 1961, MNRAS, 122, 479

Busch G. et al., 2014, A&A, 561, A140

Buttiglione S., Capetti A., Celotti A., Axon D. J., Chiaberge M., Macchetto F. D., Sparks W. B., 2009, A&A, 495, 1033

Buttiglione S., Capetti A., Celotti A., Axon D. J., Chiaberge M., Macchetto F. D., Sparks W. B., 2010, A&A, 509, A6

Capetti A., Baldi R. D., 2011, A&A, 529, A126

Capetti A., Balmaverde B., 2006, A&A, 453, 27

Capetti A., Kharb P., Axon D. J., Merritt D., Baldi R. D., 2009, AJ, 138, 1990

Capetti A., Raiteri C. M., Buttiglione S., 2010, A&A, 516, A59

Cappellari M., Bertola F., Burstein D., Buson L. M., Greggio L., Renzini A., 2001, ApJ, 551, 197

Chiaberge M., Marconi A., 2011, MNRAS, 416, 917

Chiaberge M., Capetti A., Celotti A., 1999, A&A, 349, 77

Cid Fernandes R., González Delgado R. M., Storchi-Bergmann T., Martins L. P., Schmitt H., 2005, MNRAS, 356, 270

Colbert E. J. M., Baum S. A., Gallimore J. F., O'Dea C. P., Christensen J. A., 1996, ApJ, 467, 551

Condon J. J., 1992, ARA&A, 30, 575

Condon J. J., Condon M. A., Gisler G., Puschell J. J., 1982, ApJ, 252, 102

Condon J. J., Huang Z.-P., Yin Q. F., Thuan T. X., 1991, ApJ, 378, 65

Conway J. E., Myers S. T., Pearson T. J., Readhead A. C. S., Unwin S. C., Xu W., 1994, ApJ, 425, 568

Czerny B., Siemiginowska A., Janiuk A., Nikiel-Wroczyński B., Stawarz Ł., 2009, ApJ, 698, 840

Dale D. A. et al., 2006, ApJ, 646, 161

de Gasperin F., Merloni A., Sell P., Best P., Heinz S., Kauffmann G., 2011, MNRAS, 415, 2910

de Vaucouleurs G., de Vaucouleurs A., Corwin J. R., 1976, Second Reference Catalogue of Bright Galaxies, Vol. 1976, Univ. of Texas Press, Austin

de Vaucouleurs G., de Vaucouleurs A., Corwin H. G., Jr, Buta R. J., Paturel G., Fouqué P., 1991, Third Reference Catalogue of Bright Galaxies, Vol. 82. Volume I: Explanations and references. Volume II: Data for galaxies between 0^h and 12^h. Volume III: Data for galaxies between 12^h and 24^h Sky and Telescope.

Decarli R., Gavazzi G., Arosio I., Cortese L., Boselli A., Bonfanti C., Colpi M., 2007, MNRAS, 381, 136

Di Matteo T., Springel V., Hernquist L., 2005, Nature, 433, 604

Di Matteo T., Colberg J., Springel V., Hernquist L., Sijacki D., 2008, ApJ, 676, 33

Dicken D. et al., 2014, ApJ, 788, 98

Donea A.-C., Biermann P. L., 1996, A&A, 316, 43

Donea A.-C., Biermann P. L., 2002, PASA, 19, 125

Dullo B. T. et al., 2018, MNRAS, 475, 4670

Ekers R. D., Ekers J. A., 1973, A&A, 24, 247

Falcke H., Biermann P. L., 1999, A&A, 342, 49

Falcke H., Nagar N. M., Wilson A. S., Ulvestad J. S., 2000, ApJ, 542, 197

Falcke H., Körding E., Markoff S., 2004, A&A, 414, 895

Falco E. E. et al., 1999, PASP, 111, 438

Fanaroff B. L., Riley J. M., 1974, MNRAS, 167, 31P

Fenech D. M., Muxlow T. W. B., Beswick R. J., Pedlar A., Argo M. K., 2008, MNRAS, 391, 1384

Ferrarese L., Merritt D., 2000, ApJL, 539, L9

Field G. B., Rogers R. D., 1993, ApJ, 403, 94

Filho M. E., Barthel P. D., Ho L. C., 2000, ApJS, 129, 93

Filho M. E., Barthel P. D., Ho L. C., 2002, ApJS, 142, 223

Filho M. E., Fraternali F., Markoff S., Nagar N. M., Barthel P. D., Ho L. C., Yuan F., 2004, A&A, 418, 429

Filho M. E., Barthel P. D., Ho L. C., 2006, A&A, 451, 71

Filippenko A. V., Sargent W. L. W., 1985, ApJS, 57, 503

Fraix-Burnet D., Despringre V., Baudry A., 1997, Vistas Astron., 41, 237

Gallimore J. F., Baum S. A., O'Dea C. P., Pedlar A., 1996, ApJ, 458, 136

Gallimore J. F., Baum S. A., O'Dea C. P., 2004, ApJ, 613, 794

Gallimore J. F., Axon D. J., O'Dea C. P., Baum S. A., Pedlar A., 2006, AJ, 132, 546

Gallo E., Treu T., Jacob J., Woo J.-H., Marshall P. J., Antonucci R., 2008, ApJ, 680, 154

Gallo E., Treu T., Marshall P. J., Woo J.-H., Leipski C., Antonucci R., 2010, ApJ, 714, 25

Garofalo D., 2013, Adv. Astron., 2013, 213105

Garofalo D., Evans D. A., Sambruna R. M., 2010, MNRAS, 406, 975

Gavazzi G., Consolandi G., Dotti M., Fossati M., Savorgnan G., Gualandi R., Bruni I., 2013, A&A, 558, A68

Gendre M. A., Best P. N., Wall J. V., Ker L. M., 2013, MNRAS, 430, 3086

Giovannini G., Cotton W. D., Feretti L., Lara L., Venturi T., 1998, ApJ, 493, 632

Giovannini G., Taylor G. B., Feretti L., Cotton W. D., Lara L., Venturi T., 2005, ApJ, 618, 635

Giroletti M., Panessa F., 2009, ApJ, 706, L260

Gonzalez-Serrano J. I., Perez-Fournon I., Junor W., Spencer R., 1989, Ap&SS, 157, 183

Goulding A. D., Alexander D. M., 2009, MNRAS, 398, 1165

Graham A. W., Scott N., 2013, ApJ, 764, 151

Gültekin K., Cackett E. M., Miller J. M., Di Matteo T., Markoff S., Richstone D. O., 2009, ApJ, 706, 404

Hardcastle M. J., Worrall D. M., 2000, MNRAS, 314, 359

Hardcastle M. J., Evans D. A., Croston J. H., 2009, MNRAS, 396, 1929

Heckman T. M., 1980, A&A, 87, 152

Heckman T. M., Lehnert M. D., Armus L., 1993, in Shull J. M., Thronson H. A., eds, Astrophysics and Space Science Library, Vol. 188, The Environment and Evolution of Galaxies. Kluwer, Dordrecht, p. 455

Heckman T. M., Kauffmann G., Brinchmann J., Charlot S., Tremonti C., White S. D. M., 2004, ApJ, 613, 109

Heinz S., Sunyaev R. A., 2003, MNRAS, 343, L59

Herrero-Illana R. et al., 2017, MNRAS, 471, 1634

Heywood I., Blundell K. M., Rawlings S., 2007, MNRAS, 381, 1093

Ho L. C., 1999a, ApJ, 516, 672

Ho L. C., 1999b, ApJ, 510, 631

Ho L. C., 2002, ApJ, 564, 120

Ho L. C., 2008, ARA&A, 46, 475

Ho L. C., Ulvestad J. S., 2001, ApJS, 133, 77

Ho L. C., Filippenko A. V., Sargent W. L. W., 1993, ApJ, 417, 63

Ho L. C., Filippenko A. V., Sargent W. L., 1995, ApJS, 98, 477

Ho L. C., Filippenko A. V., Sargent W. L. W., 1997, ApJS, 112, 315

Ho L. C., Filippenko A. V., Sargent W. L. W., 2003, ApJ, 583, 159

Ho L. C., Greene J. E., Filippenko A. V., Sargent W. L. W., 2009, ApJS, 183, 1

Kauffmann G. et al., 2003, MNRAS, 346, 1055

Kauffmann G. et al., 2007, ApJS, 173, 357

Kauffmann G., Heckman T. M., Best P. N., 2008, MNRAS, 384, 953

Keel W. C., 1983, ApJ, 269, 466

Kennicutt R., 1983, A&A, 120, 219

Kennicutt R. C., Jr, 1998, ARA&A, 36, 189

Kettenis M., van Langevelde H. J., Reynolds C., Cotton B., 2006, in Gabriel C., Arviset C., Ponz D., Enrique S., eds, ASP Conf. Ser., Vol. 351, Astronomical Data Analysis Software and Systems XV, Astron. Soc. Pac., San Francisco, p. 497

Kewley L. J., Dopita M. A., Sutherland R. S., Heisler C. A., Trevena J., 2001, ApJ, 556, 121

Kewley L. J., Groves B., Kauffmann G., Heckman T., 2006, MNRAS, 372, 961

Kharb P., O'Dea C. P., Baum S. A., Colbert E. J. M., Xu C., 2006, ApJ, 652, 177

Kharb P. et al., 2012, AJ, 143, 78

Kharb P., O'Dea C. P., Baum S. A., Hardcastle M. J., Dicken D., Croston J. H., Mingo B., Noel-Storr J., 2014, MNRAS, 440, 2976

Kharb P., Subramanian S., Vaddi S., Das M., Paragi Z., 2017, ApJ, 846, 12

King A. L. et al., 2011, ApJ, 729, 19

Körding E., Falcke H., Corbel S., 2006, A&A, 456, 439

Körding E. G., Jester S., Fender R., 2008, MNRAS, 383, 277

Kormendy J., Ho L. C., 2013, ARA&A, 51, 511

Kukula M. J., Ghosh T., Pedlar A., Schilizzi R. T., Miley G. K., de Bruyn A. G., Saikia D. J., 1993, MNRAS, 264, 893

Kukula M. J., Pedlar A., Baum S. A., O'Dea C. P., 1995, MNRAS, 276, 1262

Kukula M. J., Ghosh T., Pedlar A., Schilizzi R. T., 1999, ApJ, 518, 117

LaMassa S. M., Heckman T. M., Ptak A., Urry C. M., 2013, ApJ, 765, L33

Laor A., 2000, ApJ, 543, L111

Laor A., Behar E., 2008, MNRAS, 390, 847

Leech K. J., Penston M. V., Terlevich R., Lawrence A., Rowan-Robinson M., Crawford J., 1989, MNRAS, 240, 349

Lira P., Johnson R. A., Lawrence A., Cid Fernandes R., 2007, MNRAS, 382, 1552

Lovelace R. V. E., Romanova M. M., 1996, in Hardee P. E., Bridle A. H., Zensus J. A., eds, ASP Conf. Ser., Vol. 100, Energy Transport in Radio Galaxies and Quasars, Astron. Soc. Pac., San Francisco, p. 25

Maoz D., 2007, MNRAS, 377, 1696

Markoff S., Nowak M. A., Wilms J., 2005, ApJ, 635, 1203

Massaglia S., Bodo G., Rossi P., Capetti S., Mignone A., 2016, A&A, 596, A12

Mauch T., Sadler E. M., 2007, MNRAS, 375, 931

McKinney J. C., Tchekhovskoy A., Blandford R. D., 2012, MNRAS, 423, 3083

Meier D. L., 2001, ApJ, 548, L9

Merloni A., Heinz S., di Matteo T., 2003, MNRAS, 345, 1057

Mezcua M., Prieto M. A., 2014, ApJ, 787, 62

Miller N. A., Hornschemeier A. E., Mobasher B., Bridges T. J., Hudson M. J., Marzke R. O., Smith R. J., 2009, AJ, 137, 4450

Mingo B. et al., 2016, MNRAS, 462, 2631

Morganti R., 2017, Nat. Astron., 1, 596

Morganti R., Fanti C., Fanti R., Parma P., de Ruiter H. R., 1987, A&A, 183, 203

Morganti R., Tsvetanov Z. I., Gallimore J., Allen M. G., 1999, A&AS, 137, 457

Moustakas J. Kennicutt, Jr R. C., 2006, ApJS, 164, 81

Murphy E. J., Dong D., Momjian E., Linden S., Kennicutt R. C., Jr, Meier D. S., Schinnerer E., Turner J. L., 2018, ApJS, 234, 24

Muxlow T. W. B., Pedlar A., Wilkinson P. N., Axon D. J., Sanders E. M., de Bruyn A. G., 1994, MNRAS, 266, 455

Muxlow T. W. B. et al., 2010, MNRAS, 404, L109

Nagar N. M., Wilson A. S., Mulchaey J. S., Gallimore J. F., 1999, ApJS, 120, 209

Nagar N. M., Falcke H., Wilson A. S., Ho L. C., 2000, ApJ, 542, 186

Nagar N. M., Wilson A. S., Falcke H., 2001, ApJ, 559, L87

Nagar N. M., Falcke H., Wilson A. S., Ulvestad J. S., 2002a, A&A, 392, 53

Nagar N. M., Falcke H., Wilson A. S., Ulvestad J. S., 2002b, A&A, 392, 53

Nagar N. M., Falcke H., Wilson A. S., 2005, A&A, 435, 521

Narayan R., McClintock J. E., 2008, The Observatory, 51, 733

Narayan R., Yi I., 1994, ApJ, 428, L13

Narayan R., Mahadevan R., Quataert E., 1998, in Abramowicz M. A., Björnsson G., Pringle J. E., eds, Theory of Black Hole Accretion Disks. Cambridge Univ. Press, p. 148

Nemmen R. S., Bower R. G., Babul A., Storchi-Bergmann T., 2007, MNRAS, 377, 1652

Nemmen R. S., Storchi-Bergmann T., Eracleous M., 2014, MNRAS, 438, 2804

Nyland K. et al., 2016, MNRAS, 458, 2221

Orienti M., Prieto M. A., 2010, MNRAS, 401, 2599

Padovani P., 2016, A&A Rev., 24, 13

Panessa F., Giroletti M., 2013, MNRAS, 432, 1138

Panessa F., Barcons X., Bassani L., Cappi M., Carrera F. J., Ho L. C., Pellegrini S., 2007, A&A, 467, 519

Parma P., de Ruiter H. R., Fanti C., Fanti R., 1986, A&AS, 64, 135

Parma P., Fanti C., Fanti R., Morganti R., de Ruiter H. R., 1987, A&A, 181, 244

Peck L. W., Fenech D. M., 2013, Astron. Comput., 2, 54

Pedlar A., Unger S. W., Dyson J. E., 1985, MNRAS, 214, 463

Pérez E., Márquez I., Marrero I., Durret F., González Delgado R. M., Masegosa J., Maza J., Moles M., 2000, A&A, 353, 893

Pérez-Torres M. A., Alberdi A., Marcaide J. M., Guirado J. C., Lara L., Mantovani F., Ros E., Weiler K. W., 2002, MNRAS, 335, L23

Plotkin R. M., Markoff S., Kelly B. C., Körding E., Anderson S. F., 2012, MNRAS, 419, 267

Ramadarath H. et al., 2018, preprint (arXiv:1802.04417)

Rampazzo R., Reduzzi L., Sulentic J. W., Madejsky R., 1995, A&AS, 110, 131

Reynolds C. S., 1997, MNRAS, 286, 513

Risaliti G., Salvati M., Marconi A., 2011, MNRAS, 411, 2223

Sadler E. M., 1984, AJ, 89

Sadler E. M., Jenkins C. R., Kotanyi C. G., 1989, MNRAS, 240, 591

Sadler E. M., Slee O. B., Reynolds J. E., Roy A. L., 1995, MNRAS, 276, 1373

Saikia P., Körding E., Falcke H., 2015, MNRAS, 450, 2317

Salak D., Tomiyasu Y., Nakai N., Miyamoto Y., 2016, ApJ, 823, 68

Sandage A., Tammann G. A., 1981, Revised Shapley-Ames Catalog of Bright Galaxies. Vol. 635, Carnegie Inst. of Washington Publ., University of Michigan, p. 157

Sarzi M. et al., 2006, MNRAS, 366, 1151

Sarzi M. et al., 2010, MNRAS, 402, 2187

Scarpa R., Falomo R., 1997, A&A, 325, 109

Seymour N., McHardy I. M., Gunn K. F., 2004, MNRAS, 352, 131

Shakura N. I., Sunyaev R. A., 1973, A&A, 24, 337

Shankar F., 2009, The Observatory, 53, 57

Shankar F. et al., 2016, MNRAS, 460, 3119

Sikora M., Stawarz Ł., Lasota J.-P., 2008, The Observatory, 51, 891

Singh R. et al., 2013, A&A, 558, A43

Slee O. B., Sadler E. M., Reynolds J. E., Ekers R. D., 1994, MNRAS, 269, 928

Stoughton C. et al., 2002, AJ, 123, 485

Tchekhovskoy A., McKinney J. C., 2012, MNRAS, 423, L55

Tchekhovskoy A., Narayan R., McKinney J. C., 2011, MNRAS, 418, L79

Thean A., Pedlar A., Kukula M. J., Baum S. A., O'Dea C. P., 2000, MNRAS, 314, 573

Tremaine S. et al., 2002, ApJ, 574, 740

Trippe S., 2014, J. Korean Astron. Soc., 47, 159

Trippe M. L., Crenshaw D. M., Deo R. P., Dietrich M., Kraemer S. B., Rafter S. E., Turner T. J., 2010, ApJ, 725, 1749

Ulvestad J. S., Ho L. C., 2001a, ApJ, 558, 561

Ulvestad J. S., Ho L. C., 2001b, ApJ, 562, L133

Ulvestad J. S., Ho L. C., 2002, ApJ, 581, 925

Ulvestad J. S., Wilson A. S., 1984, ApJ, 278, 544

Ulvestad J. S., Wilson A. S., 1989, ApJ, 343, 659

Ulvestad J. S., Wilson A. S., Sramek R. A., 1981, ApJ, 247, 419

Unger S. W., Booler R. V., Pedlar A., 1984, MNRAS, 207, 679

van den Bosch R. C. E., 2016, ApJ, 831, 134

Varenius E., Conway J. E., Martí-Vidal I., Aalto S., Beswick R., Costagliola F., Klöckner H.-R., 2014, A&A, 566, A15
Veilleux S., Osterbrock D. E., 1987, ApJS, 63, 295
Vila M. B., Pedlar A., Davies R. D., Hummel E., Axon D. J., 1990, MNRAS, 242, 379
Volonteri M., Sikora M., Lasota J.-P., Merloni A., 2013, ApJ, 775, 94
Westcott J. et al., 2017, MNRAS, 467, 2113
Williams D. R. A. et al., 2017, MNRAS, 472, 3842
Wrobel J. M., 1991, AJ, 101, 127
Wrobel J. M., 2000, ApJ, 531, 716
Wrobel J. M., Heeschen D. S., 1991, AJ, 101, 148
Yuan F., Narayan R., 2014, ARA&A, 52, 529
Yuan F., Bu D., Wu M., 2012, ApJ, 761, 130

SUPPORTING INFORMATION

Supplementary data are available at *MNRAS* online.

APPENDIX A: RADIO DATA

In the Appendix, we present the radio images of the 47 detected objects of the Palomar sample studied here (Figs A1 and A2). Tables A1 and A2 list the source parameters of the radio components detected in the images for the identified and unidentified sources, respectively. Table A3 provides the radio contours and the properties of the restoring beams of the radio maps.

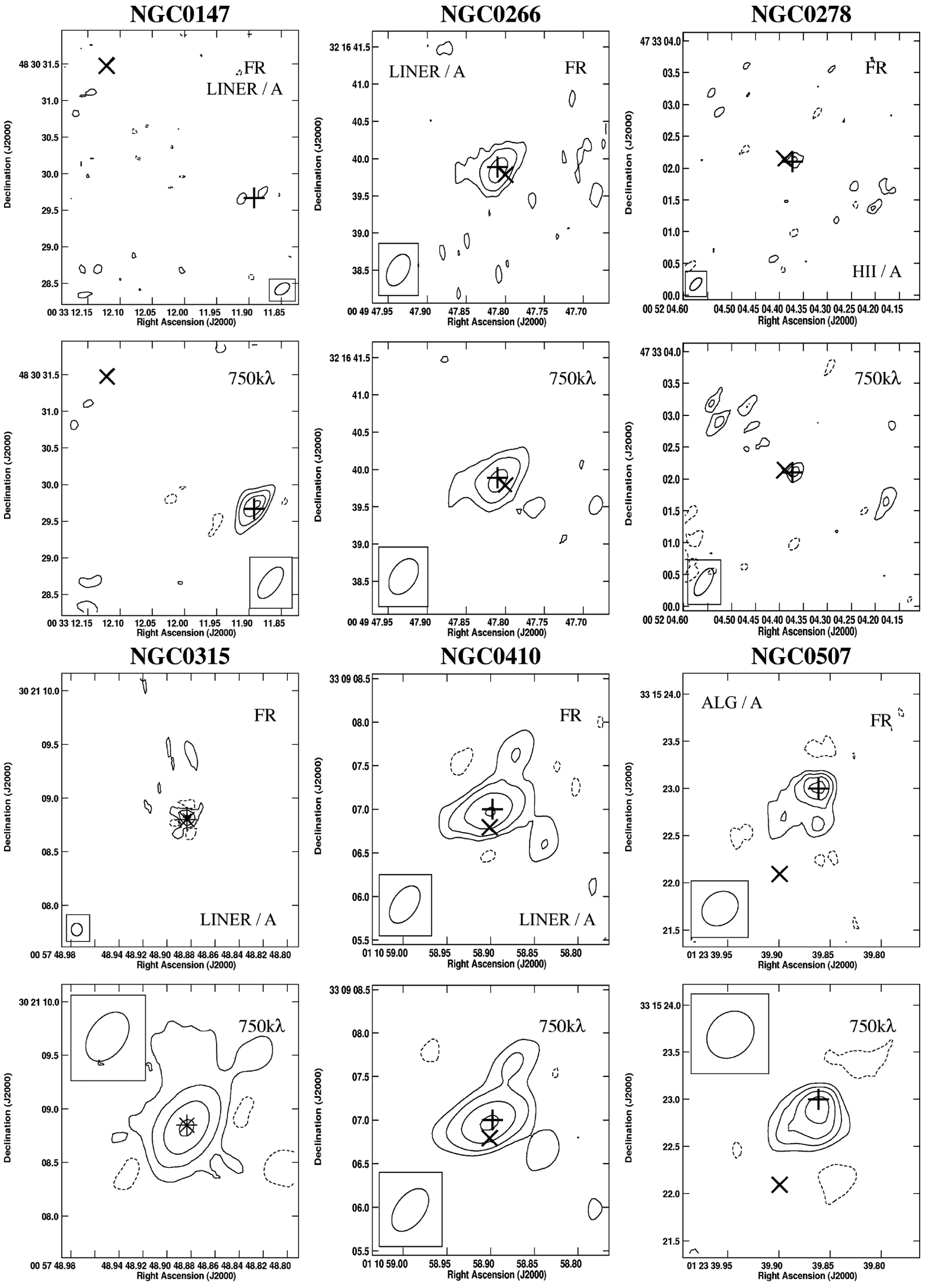

Figure A1. eMERLIN 1.5-GHz radio images of the galaxies with an identified radio core. For each galaxy two panels are shown. The upper panel shows the full-resolution map, while the lower panel shows the low-resolution map obtained with a uv-tapered scale written in the panel (in kλ). For four galaxies (NGC 3665, NGC 5005, NGC 5194, and NGC 5985) a third radio map is presented corresponding to a lower resolution map (see the scale and map parameters in Table A3). The maps for the each source are on the same physical scale, unless there is a zoom-in map, marked with a box around the selected source. The restoring beam is presented as an ellipse on one of the corners of each of the maps. The contour levels of the images are presented in Table A3. The × mark indicates the optical galaxy centre taken from NED, while the + symbol marks the radio core position, if identified. In the upper panels, the optical (LINER, Seyfert, H II, and ALG) and radio (A, B, C, D, E; see Section 4.2 for description) classifications of the sources are reported.

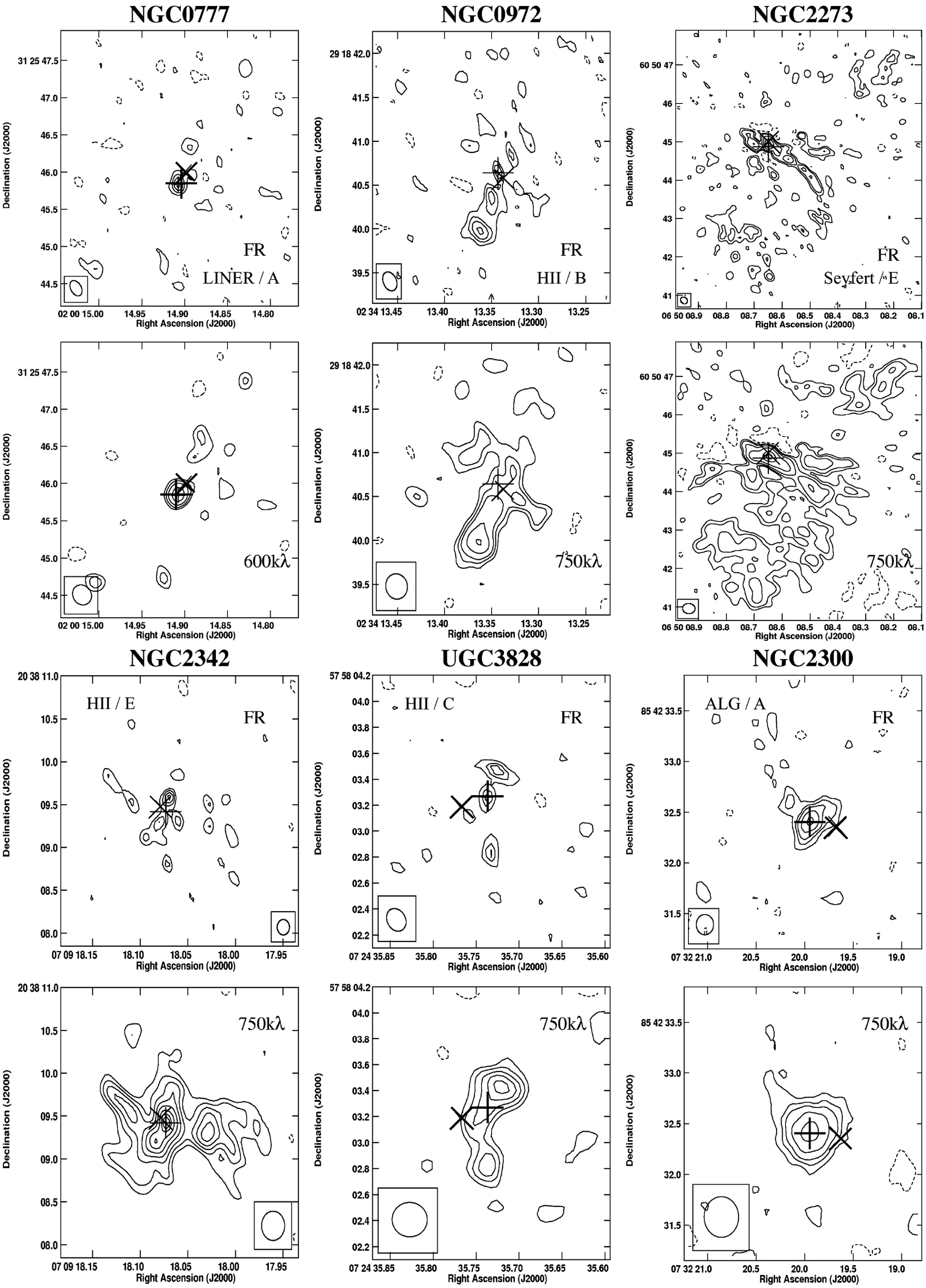

Figure A1 – *continued*

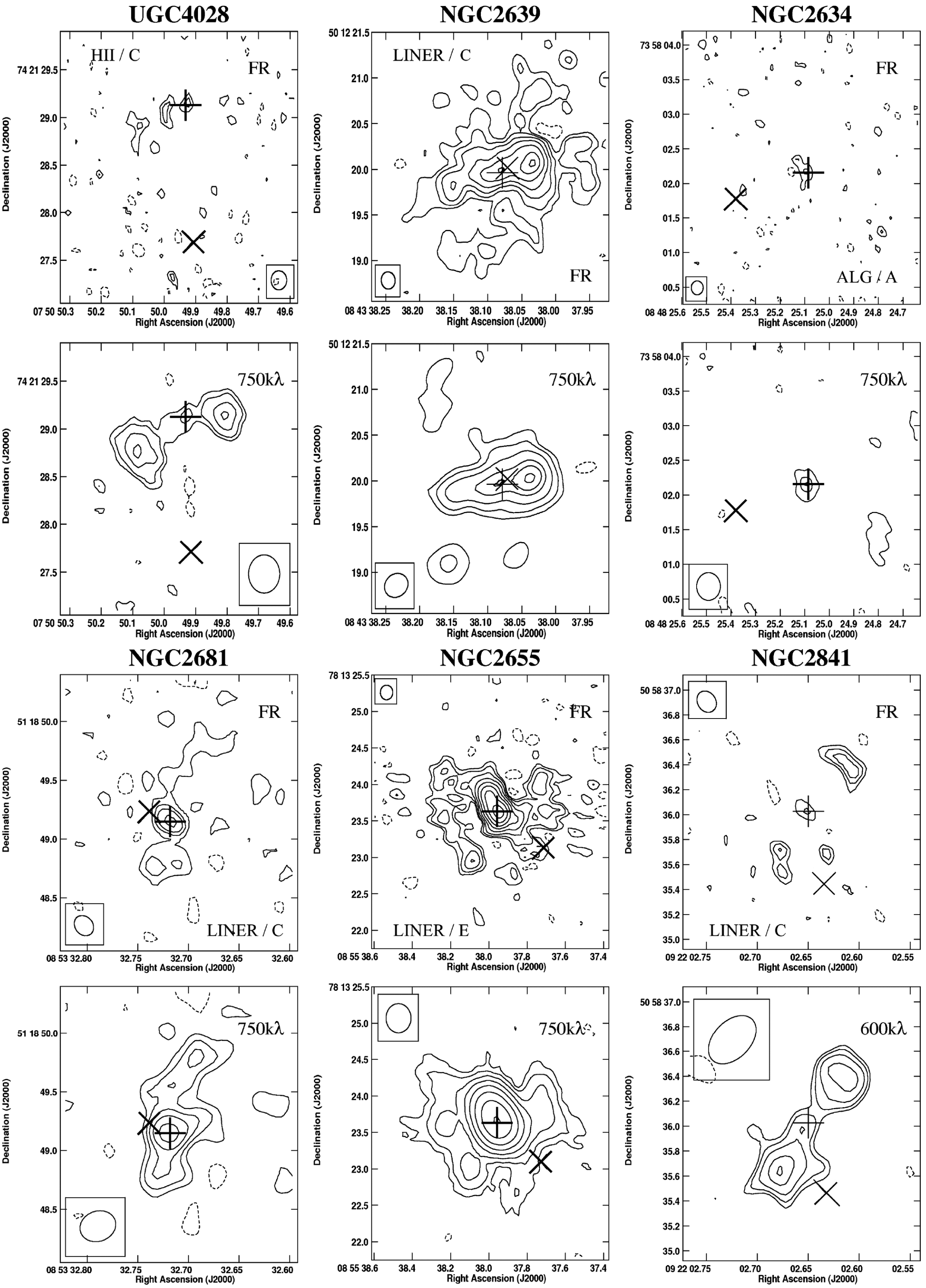

Figure A1 – *continued*

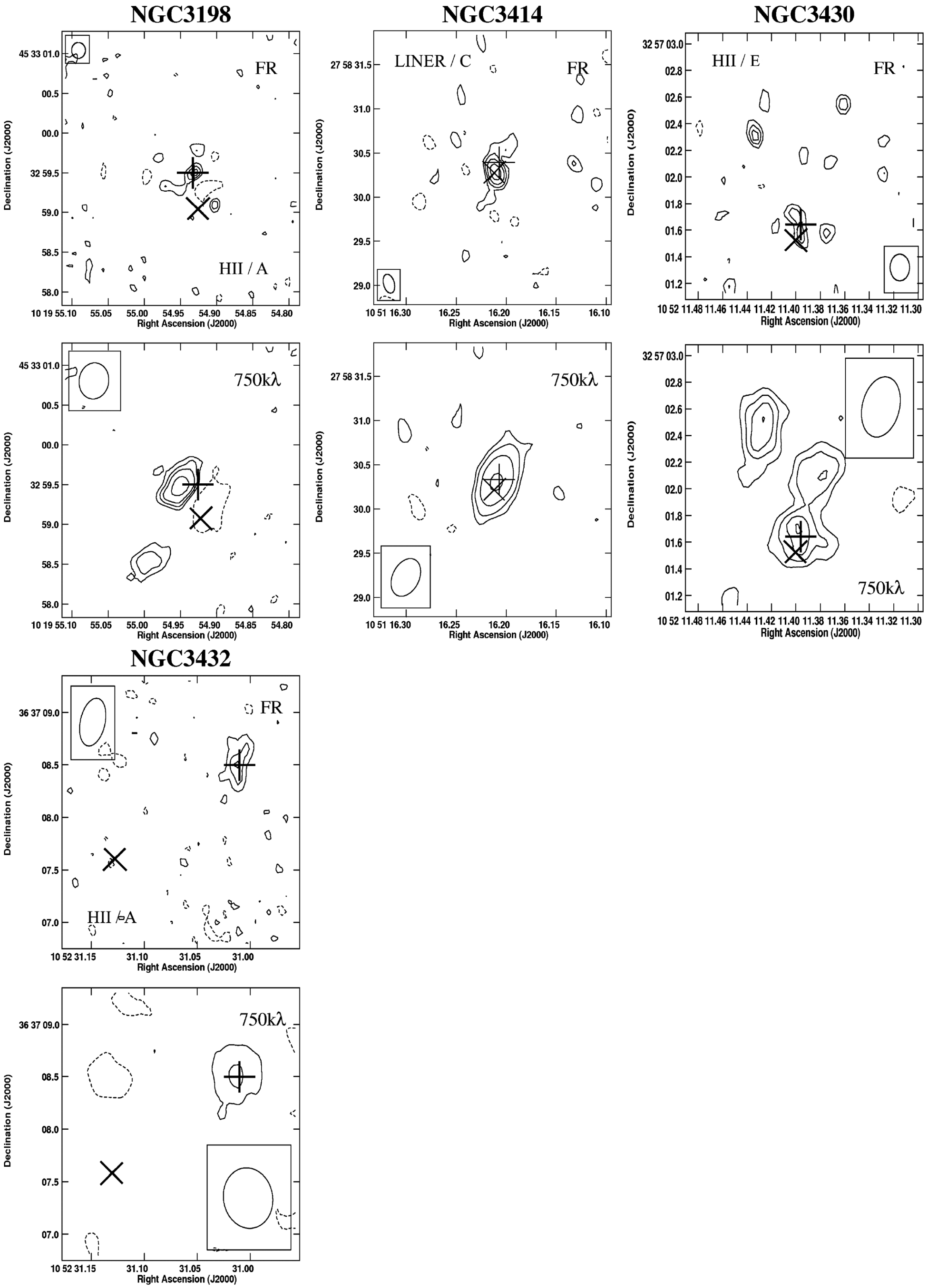

Figure A1 – *continued*

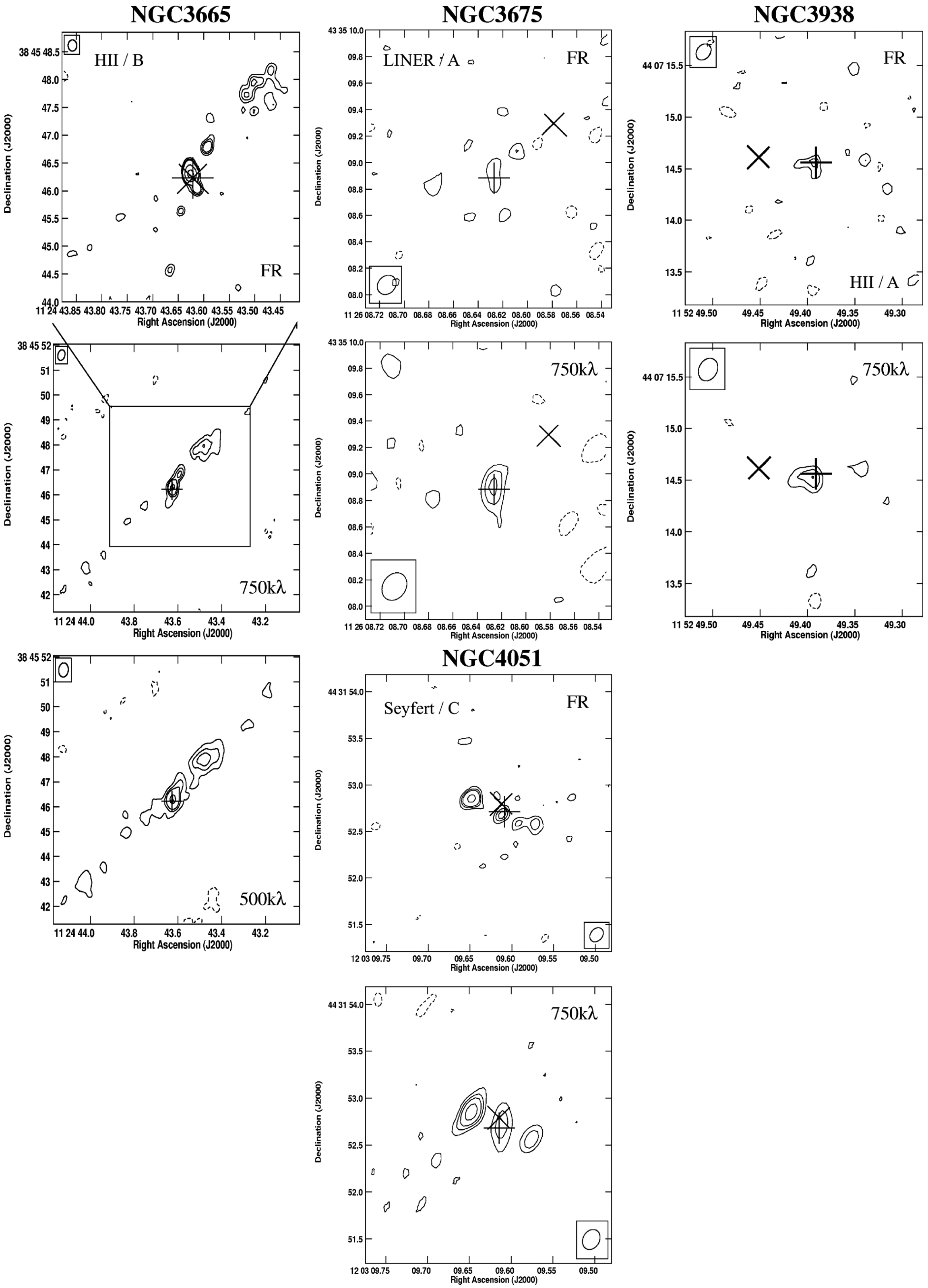

Figure A1 – *continued*

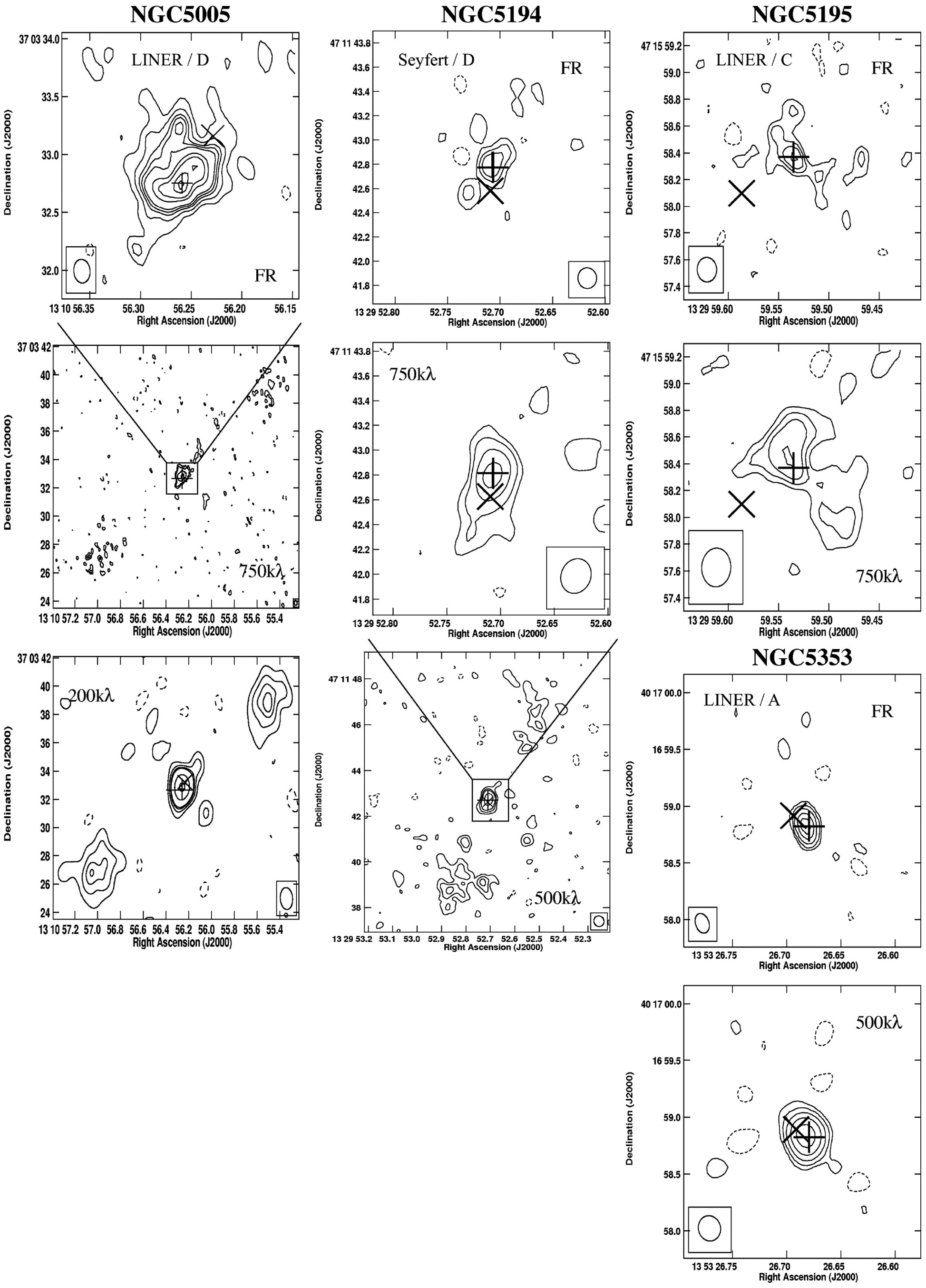

Figure A1 – *continued*

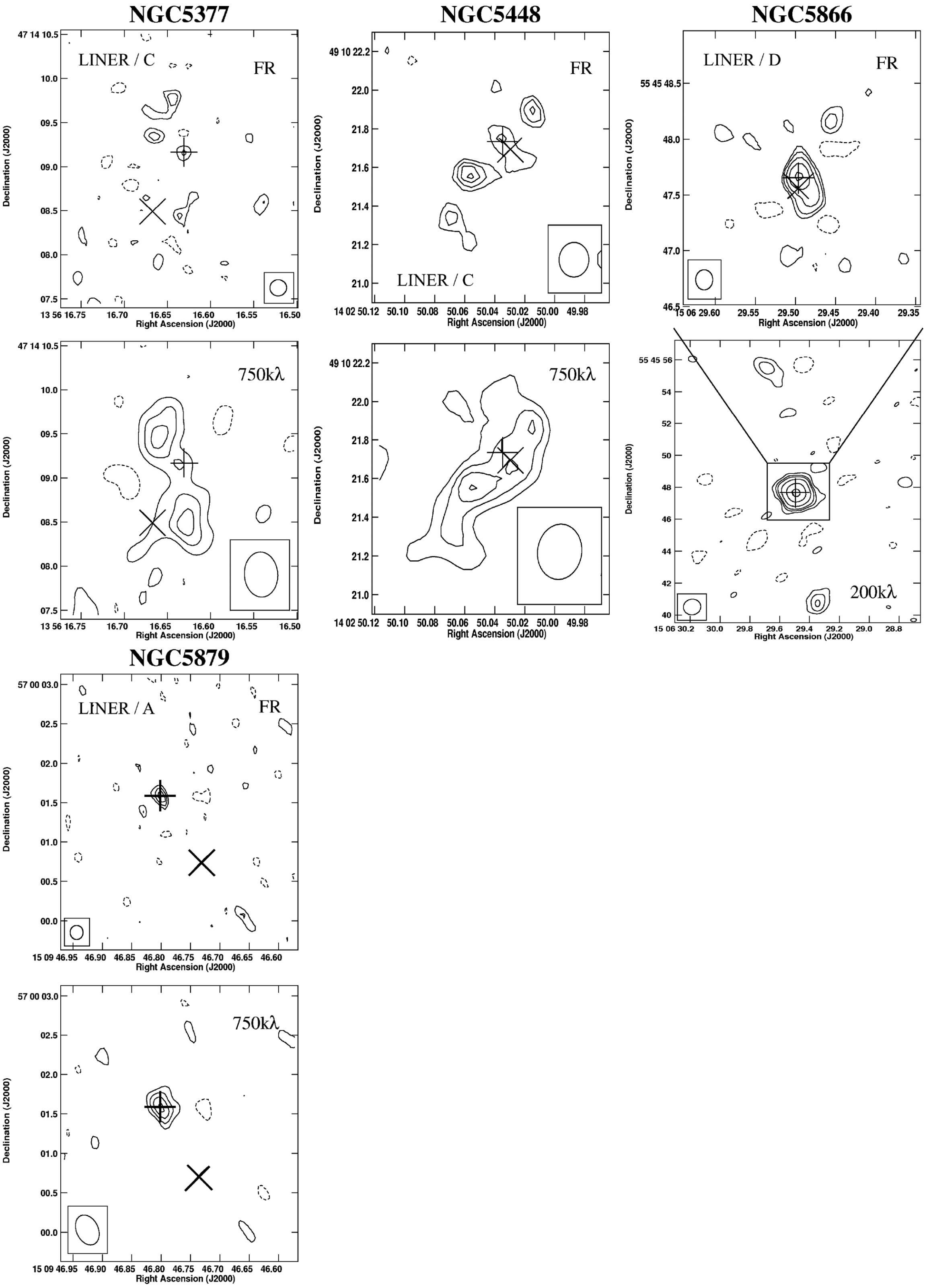

Figure A1 – *continued*

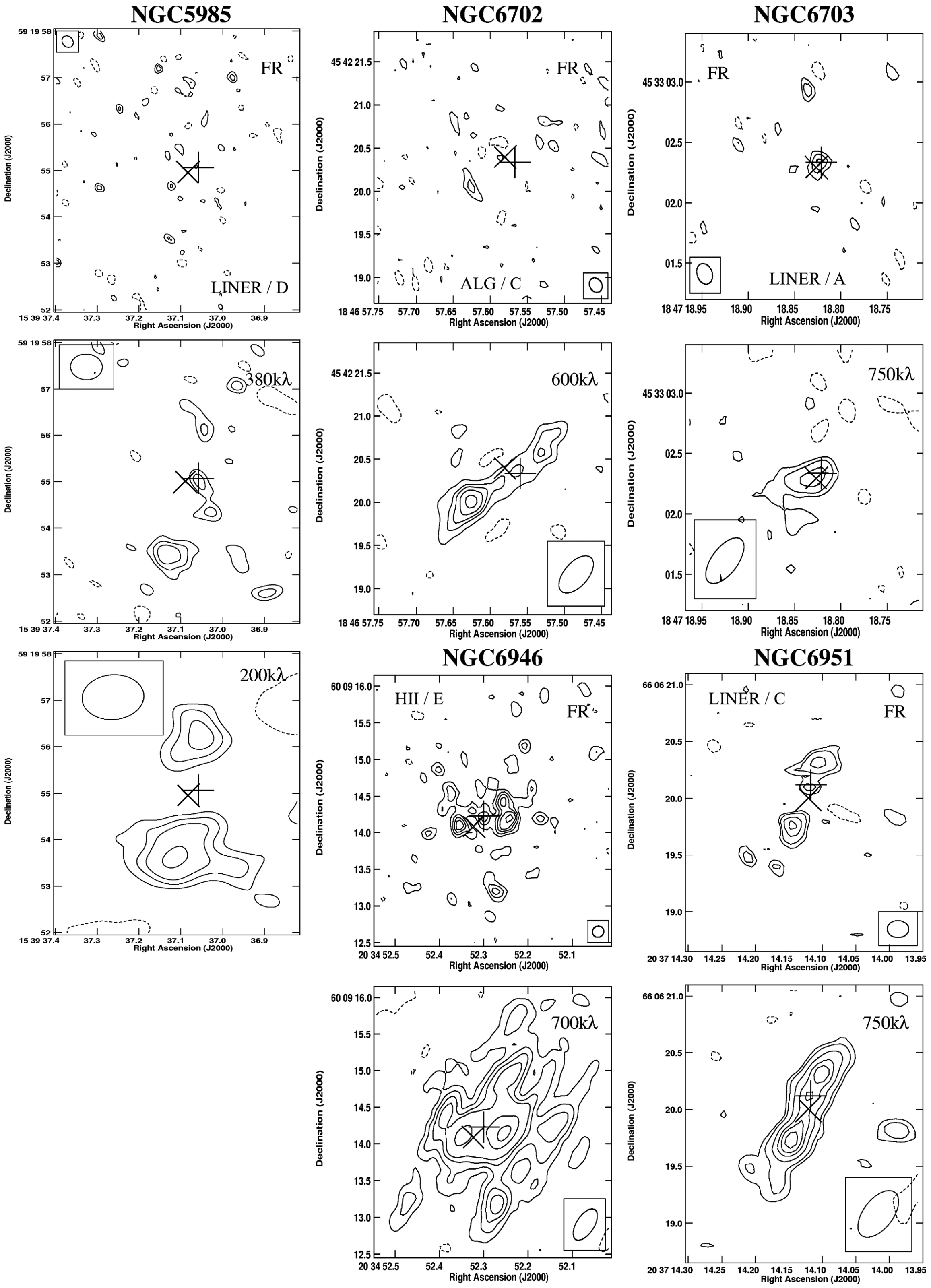

Figure A1 – *continued*

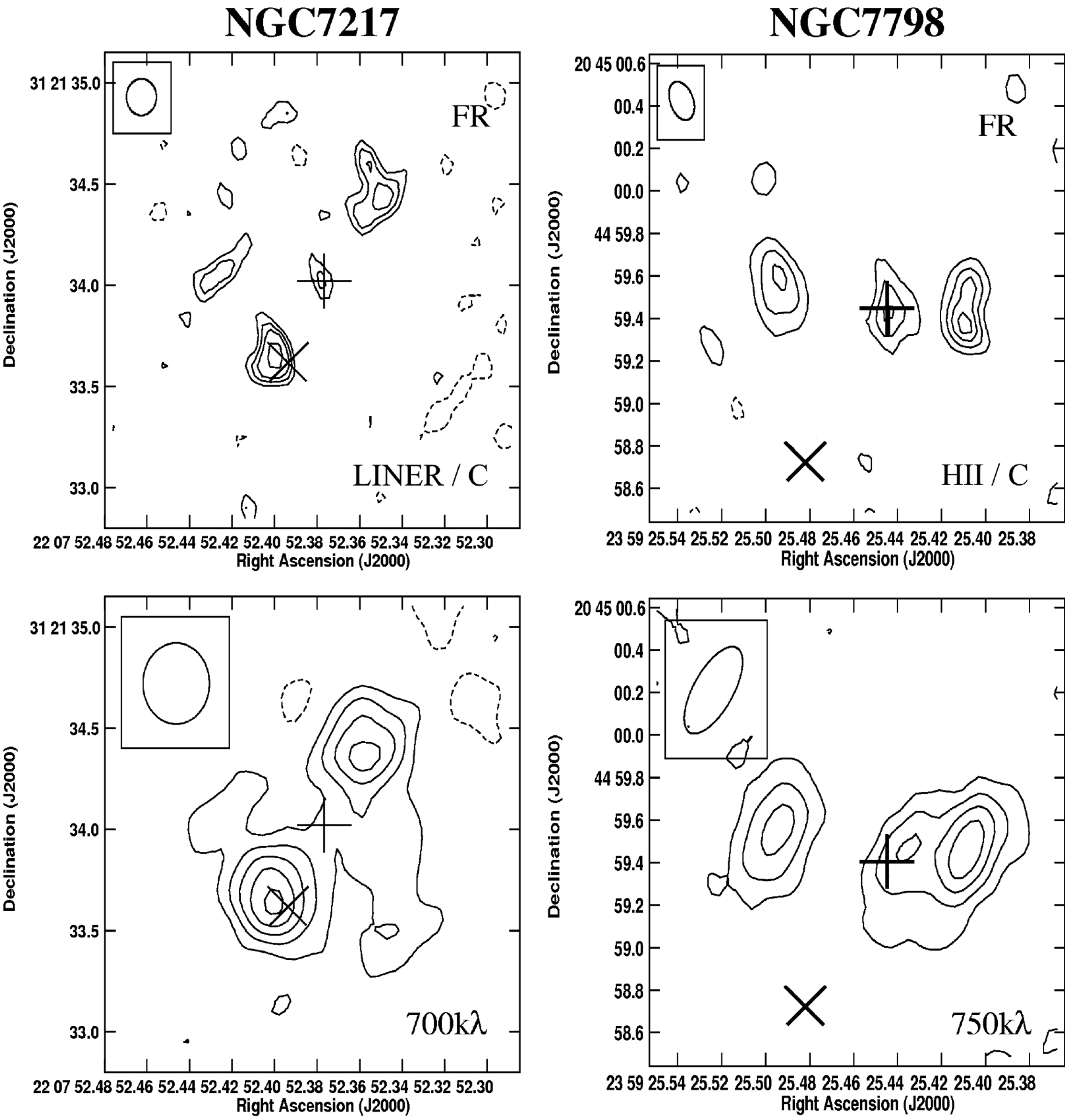

Figure A1 – *continued*

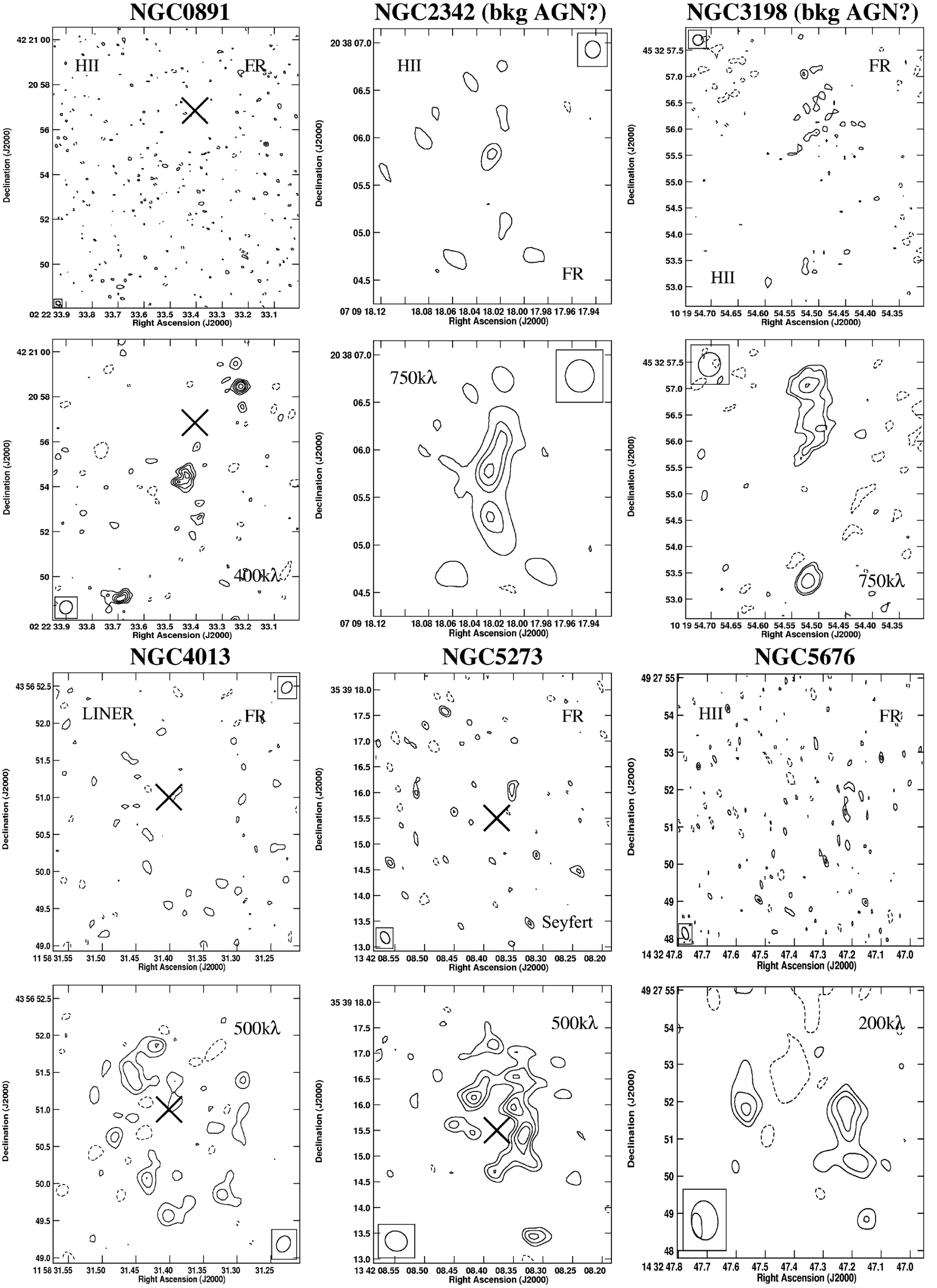

NGC0891

NGC2342 (bkg AGN?)

NGC3198 (bkg AGN?)

NGC4013

NGC5273

NGC5676

Figure A2. eMERLIN 1.5-GHz radio images of the galaxies, which are detected but no radio core is identified. For each galaxy two panels are shown. The upper panel shows the full-resolution (FR) map, while the lower panel shows the low-resolution map obtained with a uv-tapered scale written in the panel (in kλ). The restoring beam is presented as an ellipse on one of the corners of each of the maps. The contour levels of the maps are presented in Table A3. The × mark indicates the optical galaxy centre taken from NED. The maps for the each source are on the same physical scale. The images presented for NGC 2342 and NGC 3198 show jet-like features of possible background AGN, while NGC 5676, NGC 5907, and NGC 6015 show off-nuclear regions, possibly attributed to SF (see Section 4.3 for details). In the upper panels, the optical (LINER, Seyfert, H II, and ALG) classification of the sources is reported.

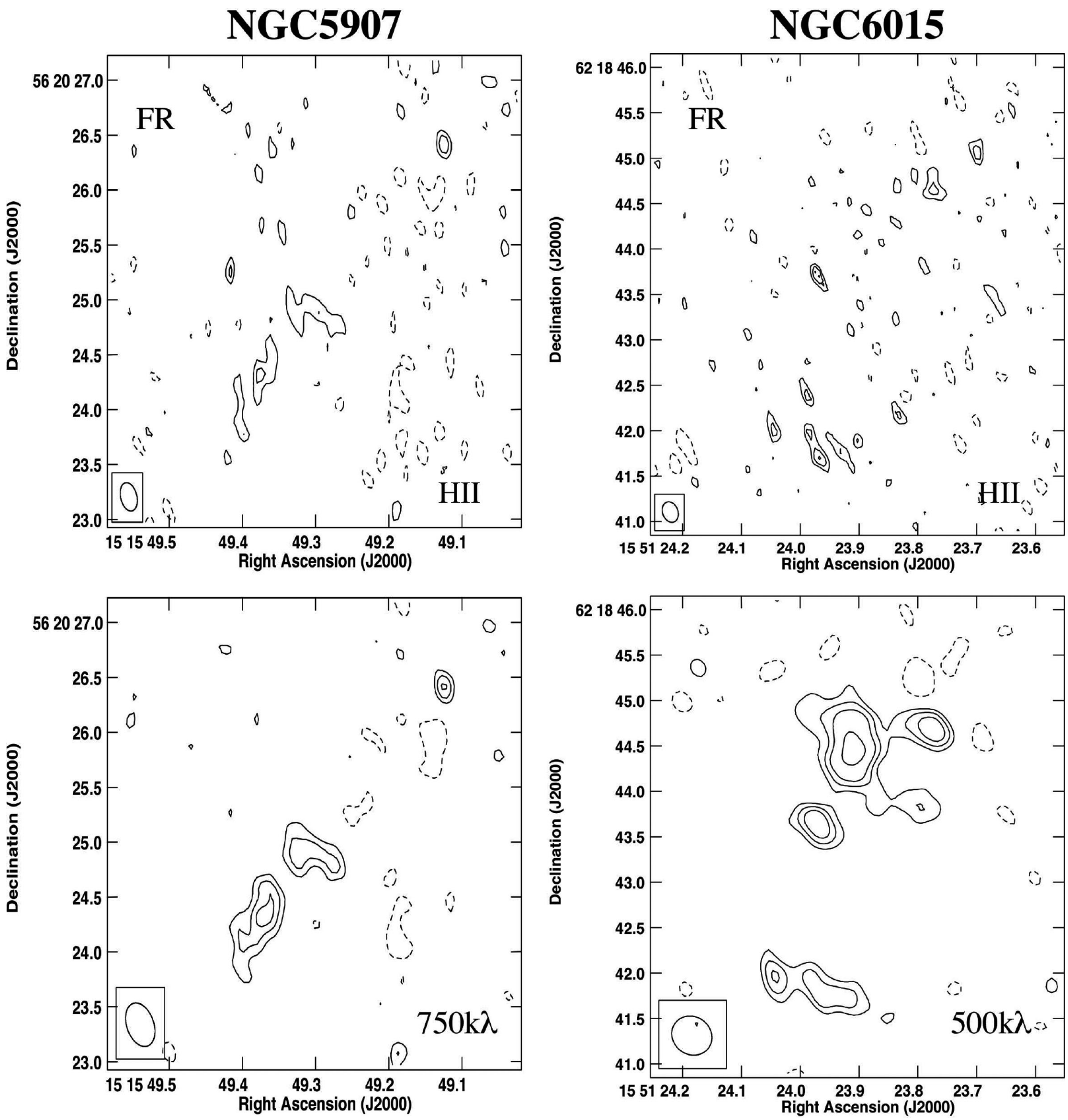

Figure A2 – *continued*

Table A1. Properties of the detected sources.

		Full resolution									Low resolution			
Name	Comp	$\theta_{\rm M} \times \theta_{\rm m}$ arcsec	PA$_{\rm d}$ deg	rms mJB	α(J2000)	δ(J2000)	$F_{\rm peak}$ mJB	$F_{\rm tot}$ mJy	$u-v$ kλ	$\theta_{\rm M} \times \theta_{\rm m}$ arcsec	PA$_{\rm d}$ deg	rms mJB	$F_{\rm peak}$ mJB	morph/size
NGC 147		0.13 × <0.198	28.40	0.073	00 33 11.894	48 30 29.69	<0.28	0.95	750	0.39 × 0.07	142.8	0.070	0.5 ± 0.09	core (A)
	Tot												0.95 ± 0.10	
NGC 266	core	0.16 × <0.26	174.1	0.095	00 49 47.810	32 16 39.83	1.24 ± 0.10	1.31	750	0.20 × 0.12	159.0	0.10	1.28 ± 0.10	core-jet (A) 1.5″ →480pc
	Tot												1.5 ± 0.1	
NGC 278		0.19 × <0.34	109.0	0.050	00 52 04.203	47 33 01.38	0.26 ± 0.06	0.29	750	0.48 × 0.05	157.3	0.054	2.1 ± 0.05	core (A) + components
	core	0.17 × <0.25	62.4	0.050	00 52 04.368	47 33 02.13	0.26 ± 0.06	0.34	750	0.16 × <0.30	146.6	0.054	0.24 ± 0.05	
		0.04 × <0.28	74.7	0.050	00 52 0.4527	47 33 02.899	0.18 ± 0.06	0.20	750	0.17 × <0.45	159.8	0.054	0.24 ± 0.05	
	Tot												2.7 ± 0.2	
NGC 315	core	0.01 × 0.08	67.3	5.5	00 57 48.883	30 21 08.82	490 ± 30	503	750	0.10 × <0.21	71.0	4.0	331 ± 26	core-jet (A)
	Tot												520 ± 50	
NGC 410	core	0.53 × 0.11	89.6	0.14	01 10 58.901	33 09 06.98	2.05 ± 0.14	3.62	750	0.55 × 0.10	93.6	0.16	2.21 ± 0.16	core-jet (A)
	Tot												3.8 ± 0.2	
NGC 507	core	0.24 × <0.41	68.4	0.18	01 23 39.863	33 15 23.00	0.93 ± 0.18	1.02	750	0.42 × 0.24	16.7	0.26	1.01 ± 0.26	core-jet (A)
	Tot												1.5 ± 0.1	
NGC 777		0.17 × <0.23	152.6	0.077	02 00 14.894	31 25 46.33	0.36 ± 0.09	0.59	600	0.88 × <0.22	163.8	0.081	0.32 ± 0.12	core (A) + components
	core	0.17 × <0.14	171.7	0.077	02 00 14.908	31 25 45.84	0.74 ± 0.10	0.84	600	0.16 × <0.25	108.9	0.081	0.84 ± 0.12	
	Tot												1.2 ± 0.2	
NGC 972	core	0.06 × <0.06	164.2	0.069	02 34 13.34	29 18 40.65	0.25 ± 0.08	0.38	750	0.42 × 0.26	157.6	0.069	0.26 ± 0.09	one-sided jet (B) 1.7″ →185pc
		<0.24 × <0.17	162.2	0.069	02 34 13.35	29 18 40.40	0.30 ± 0.08	0.33	750	0.45 × 0.29	148.4	0.069	0.35 ± 0.09	
		0.40 × 0.27	152.5	0.069	02 34 13.56	29 18 34.99	0.38 ± 0.08	1.44	750	0.39 × 0.26	145.8	0.069	0.55 ± 0.09	
	Tot												1.4 ± 0.2	
NGC 2273		0.19 × 0.06	72.1	0.930	06 50 08.577	60 50 44.55	1.64 ± 0.10	2.26	750			0.12	<3.25	twin jet + extended emission (E) 2.2″ →280pc
	core	0.25 × 0.16	169.4	0.930	06 50 08.647	60 50 44.93	2.99 ± 0.10	7.12	750	0.29 × 0.19	61.9	0.12	4.87 ± 0.13	
		0.30 × 0.11	48.3	0.930	06 50 08.701	60 50 44.94	1.68 ± 0.09	4.17	750			0.12	<4.82	
	Tot												66.1 ± 3.0	
NGC 2342				0.065	07 09 18.029	20 38 09.26	<0.41		750	0.53 × 0.34	164.3	0.068	0.51 ± 0.09	complex (E) 2.5″ →865pc
	core	0.17 × 0.08	151.6	0.065	07 09 18.069	20 38 09.59	0.41 ± 0.08	0.54	750	0.53 × 0.28	172.4	0.068	<5.8	
		0.26 × 0.03	133.5	0.065	07 09 18.080	20 38 09.28	0.30 ± 0.08	0.52	750	0.63 × 0.34	135.2	0.068	0.59 ± 0.09	
	Tot												5.0 ± 0.2	
UGC 3828	lobeN	0.22 × <0.12	73.2	0.071	07 24 35.726	57 58 03.47	0.32 ± 0.10	0.51	750	0.32 × 0.19	93.3	0.078	0.49 ± 0.11	double jet (C) 1″ →238pc
	lobeS	0.16 × <0.29	1.4	0.071	07 24 35.733	57 58 02.83	0.29 ± 0.10	0.35	750	0.23 × <0.38	178.1	0.078	0.38 ± 0.12	
	core	0.13 × 0.23	156.69	0.071	07 24 35.7372	57 58 03.261	0.30 ± 0.10	0.31	750			0.078	<4.8	
	Tot												1.09 ± 0.10	

Table A1 – *continued*

				Full resolution								Low resolution		
Name	Comp	$\theta_{\rm M} \times \theta_{\rm m}$ arcsec	PA$_{\rm d}$ deg	rms mJB	α(J2000)	δ(J2000)	$F_{\rm peak}$ mJB	$F_{\rm tot}$ mJy	$u-v$ kλ	$\theta_{\rm M} \times \theta_{\rm m}$ arcsec	PA$_{\rm d}$ deg	rms mJB	$F_{\rm peak}$ mJB	morph/size
NGC 2300	core	0.18 × 0.06	138.2	0.060	07 32 19.945	85 42 32.41	0.99 ± 0.08	1.25	750	0.22 × 0.09	116.3	0.065	1.21 ± 0.08	core-jet (A) 0.75″ →103pc
	Tot												1.5 ± 0.1	
UGC 4028	lobeW			0.10	07 50 49.810	74 21 29.15	<0.30		750	0.21 × 0.26	53.2	0.072	0.44 ± 0.08	twin jets (C) 1.5″ →406pc
	core	>0.18 × >14	155	0.10	07 50 49.931	74 21 29.13	0.33 ± 0.10	0.33	750	0.12 × <0.26	127.8	0.072	0.23 ± 0.08	
	lobeW			0.10	07 50 50.0749	74 21 28.77	<0.30		750	0.46 × 0.24	55.96	0.072	0.43 ± 0.08	
	Tot												1.0 ± 0.1	
NGC 2639		0.32 × 0.25	121.1	0.13	08 43 38.034	50 12 20.07	17.5 ± 0.1	25.2	750	0.38 × 0.26	102.1	0.29	24.5 ± 0.3	twin jets (C) 1.5″ →340pc
	core	0.42 × 0.08	108.4	0.13	08 43 38.080	50 12 19.99	12.6 ± 0.1	17.8	750	0.42 × 0.18	105.0	0.29	17.6 ± 0.3	
		0.29 × 0.20	141.8	0.13	08 43 38.151	50 12 19.82	3.40 ± 0.1	8.3	750			0.29	<11.4	
	Tot												98 ± 10	
NGC 2634	core	0.25 × <0.3	38.8	0.082	08 48 25.095	73 58 02.15	0.39 ± 0.11	0.59	750	0.10 × <0.4	31.4	0.081	0.41 ± 0.12	core (A)
	Tot												0.45 ± 0.1	
NGC 2681	jetN			0.92	08 53 32.693	51 18 49.78	<3.7		750	0.68 × 0.18	141.1	0.099	0.57 ± 0.12	twin jets (C) 1.5″ →70pc
	core	0.17 × 0.07	56.7	0.92	08 53 32.718	51 18 49.15	1.03 ± 0.10	1.49	750	0.20 × 0.16	175.2	0.099	1.22 ± 0.12	
		0.20 × 0.16	169.5	0.92	08 53 32.733	51 18 48.77	0.473 ± 0.10	0.90	750	0.41 × 0.28	161.6	0.099	0.54 ± 0.12	
	Tot												3.1 ± 0.2	
NGC 2655	core	0.17 × 0.07	40.8	0.12	08 55 37.950	78 13 23.63	36.81 ± 0.13	51.5	750	0.37 × 0.10	38.2	0.16	53.04 ± 0.17	S-shaped jet + components (E) 2″ →204pc
		0.17 × 0.10	148.0	0.12	08 55 38.09	78 13 22.96	1.62 ± 0.13	2.35	750	0.45 × 0.31	170.1	0.16	2.09 ± 0.17	
	Tot												88 ± 2	
NGC 2841	lobeN	0.45 × <0.12	50.4	0.074	09 22 02.611	50 58 36.39	0.40 ± 0.09	0.51	600	0.36 × <0.40	46.9	0.081	0.51 ± 0.11	twin jets (C) 1.5″ →68pc
	core	0.19 × <0.12	52.7	0.074	09 22 02.652	50 58 36.03	0.27 ± 0.09	0.31	600	0.36 × <0.45	166.9	0.081	0.31 ± 0.11	
	lobeS	0.02 × <0.19	52.7	0.074	09 22 02.676	50 58 35.65	0.31 ± 0.09	0.63	600	0.23 × <0.51	114.2	0.081	0.52 ± 0.11	
	Tot												1.15 ± 0.15	
NGC 3198	core	0.15 × <0.08	125.9	0.114	10 19 54.931	45 32 59.50	0.50 ± 0.12	0.52	750	0.45 × <0.05	137.7	0.81	0.49 ± 0.09	core+ component (A)
				0.114	10 19 54.994	45 32 58.53	<0.33		750	0.47 × <0.19	120.2	0.81	0.30 ± 0.09	
	Tot												0.74 ± 0.15	
NGC 3414	core	0.07 × <0.12	162.4	0.060	10 51 16.211	27 58 30.28	1.56 ± 0.10	1.67	750	0.32 × 0.07	159.7	0.11	1.89 ± 0.13	twin jet (C) 1″ →95pc
	Tot												2.1 ± 0.1	
NGC 3430				0.10	10 52 11.384	32 57 02.11	<0.30		750	0.29 × >0.28	113.5	0.069	0.33 ± 0.08	double-lobed/complex (E) 2.2″ →230pc
	core			0.10	10 52 11.403	32 57 01.63	<0.30		750	0.42 × >0.29	102.6	0.069	0.43 ± 0.08	
		0.17 × <0.13	167.4	0.10	10 52 11.433	32 57 02.32	0.41 ± 0.11	0.42	750	0.64 × 0.59	55.3	0.069	0.42 ± 0.11	
	Tot												1.2 ± 0.2	

Table A1 – *continued*

		Full resolution								Low resolution				
Name	Comp	$\theta_{\rm M} \times \theta_{\rm m}$ arcsec	PA$_{\rm d}$ deg	rms mJB	α(J2000)	δ(J2000)	$F_{\rm peak}$ mJB	$F_{\rm tot}$ mJy	$u - v$ kλ	$\theta_{\rm M} \times \theta_{\rm m}$ arcsec	PA$_{\rm d}$ deg	rms mJB	$F_{\rm peak}$ mJB	morph/size
NGC 3432	core	>0.38 × >0.21	173.4	0.11	10 52 31.012	36 37 08.50	0.60 ± 0.14	0.61	750	>0.53 × >0.44	142.7	0.13	0.47 ± 0.14	core (A)
	Tot												0.62 ± 0.15	
NGC 3665	blobN			0.061	11 24 43.482	38 45 47.89	<5.3		{ 750	1.60 × 0.74	109.7	0.35	1.71 ± 0.35	extended one-sided jet (B) 4.2″ →580pc
									500	1.78 × 0.82	107.8	0.45	2.27 ± 0.45	
	jetN			0.061	11 24 43.592	38 45 46.80	0.71 ± 0.08	1.13	{ 750	0.64 × 0.25	143.5	0.35	2.00 × 0.35	
									500				<3.5	
	core	0.10 × 0.01	20.5	0.061	11 24 43.626	8 45 46.31	3.78 ± 0.08	4.25	{ 750	0.34 × 0.22	0.47	0.35	4.09 ± 0.35	
									500	0.44 × 0.32	167.4	0.45	4.71 ± 0.44	
	Tot												25 ± 3	
NGC 3675	core			0.080	11 26 08.627	43 35 08.91	<0.53		750	0.31 × <0.15	174.5	0.077	0.31 ± 0.08	core + comp (A)
	Tot												0.5 ± 0.1	
NGC 3938	core	<0.15 × <0.07	144.6	0.074	11 52 49.393	44 07 14.57	0.28 ± 0.07	0.33	750	0.41 × 0.08	90.4	0.083	0.32 ± 0.08	core (A)
	Tot												0.6 ± 0.1	
NGC 4051	lobeW	0.28 × 0.07	132.2	0.071	12 03 09.576	44 31 52.572	0.35 ± 0.07	0.57	750	0.28 × 0.07	132.2	0.20	8.41 ± 2.1	triple source (C) 1″ →50pc
	core	0.15 × 0.11	145.2	0.071	12 03 09.612	44 31 52.69	0.38 ± 0.07	0.63	750	0.47 × 0.14	175.3	0.20	7.96 ± 2.1	
	lobeE	0.10 × 0.06	78.3	0.071	12 03 09.648	44 31 52.85	0.86 ± 0.07	1.08	750	0.29 × 0.08	144.4	0.20	15.9 ± 2.1	
	Tot											64.5 ± 7.0		
NGC 5005	lobeN			0.093	13 10 55.512	37 03 38.96	<0.24		200	2.41 × 2.32	153.7	0.34	2.8 ± 0.3	double-lobed jets (D) 26″ →1.7kpc
		0.54 × 0.28	106.3	0.093	13 10 56.247	37 03 32.87	2.08 ± 0.09	10.6	750			0.090	<8.4	
	core	0.34 × 0.23	138.3	0.093	13 10 56.260	37 03 32.74	2.37 ± 0.09	7.49	{ 750	0.56 × 0.28	127.8	0.090	4.44 ± 0.10	
									200	0.88 × 0.41	128.7	0.34	15.2 ± 0.3	
	lobeS			0.093	13 10 57.009	37 03 26.81	<0.29		200	2.20 × 2.10	123.1	0.34	2.5 ± 0.3	
	Tot												42.3 ± 3.0	
NGC 5194	lobeN			0.101	13 29 52.510	47 11 45.97	<0.34		500			0.078	4.7 ± 0.2^{tot}	
	core	0.18 × 0.09	145.3	0.091	13 29 52.708	47 11 42.80	1.08 ± 0.09	1.74	{ 750	0.23 × 0.10	159.8	0.076	1.4 ± 0.1	double-lobed (D) on 10″ →370pc
									500	0.50 × 0.10	170.3	0.078	1.7 ± 0.1	
	lobeS			0.111	13 29 52.819	47 11 38.92	<0.35		500			0.078	5.8 ± 0.2^{tot}	
	Tot												13.1 ± 1.5	
NGC 5195	jetW			0.080	13 29 59.493	47 15 58.07	<0.24		750	0.93 × 0.59	35.9	0.11	0.33 ± 0.1	twin jet (C) 1″ →37pc
	core	0.21 × 0.02	55.0	0.080	13 29 59.535	47 15 58.37	0.51 ± 0.09	0.77	750			0.11	<6.3	
	jetE			0.080	13 29 59.539	47 15 58.50	<0.25		750	0.54 × 0.34	158.5	0.11	0.61 ± 0.1	
	Tot												2.5 ± 0.2	
NGC 5353	core	0.12 × 0.04	8.4	0.18	13 53 26.682	40 16 58.83	16.5 ± 0.2	21.0	500	0.12 × 0.07	21.1	0.14	17.6 ± 0.2	core (A)
	Tot												17.9 ± 0.1	
NGC 5377	jetS			0.091	13 56 16.627	47 14 08.52	<5.1		500	0.60 × 0.21	4.0	0.11	0.53 ± 0.12	twin jets (C) 1.8″ →227pc
	core	0.11 × 0.04	168.2	0.091	13 56 16.631	47 14 09.16	0.30 ± 0.09	0.36	500	0.19 × <0.33	57.8	0.11	0.38 ± 0.13	

Table A1 – *continued*

				Full resolution									Low resolution		
Name	Comp	$\theta_{\rm M} \times \theta_{\rm m}$ arcsec	PA$_{\rm d}$ deg	rms mJB	α(J2000)	δ(J2000)	$F_{\rm peak}$ mJB	$F_{\rm tot}$ mJy		$u-v$ kλ	$\theta_{\rm M} \times \theta_{\rm m}$ arcsec	PA$_{\rm d}$ deg	rms mJB	$F_{\rm peak}$ mJB	morph/size
	jetN			0.091	13 56 16.658	47 14 09.49	<1.0			500	0.50 × 0.27	156.1	0.11	0.53 ± 0.12	
	Tot													1.3 ± 0.2	
NGC 5448		0.10 × <0.21	28.0	0.086	14 02 50.015	49 10 21.89	0.35 ± 0.10	0.50		750	0.19 × 0.14	21.9	0.082	0.37 ± 0.11	twin jet (C) 1″ →141pc
	core	0.22 × 0.05	59.1	0.086	14 02 50.035	49 10 21.75	0.28 ± 0.09	0.45		750	0.59 × 0.34	137.8	0.082	0.36 ± 0.11	
		0.18 × <0.12	86.1	0.086	14 02 50.057	49 10 21.56	0.39 ± 0.10	0.53		750	0.43 × <0.21	98.6	0.082	0.45 ± 0.11	
		0.19 × 0.10	53.5	0.086	14 02 50.069	49 10 21.34	0.30 ± 0.10	0.40		750	0.69 × 0.24	172.6	0.082	0.32 ± 0.10	
	Tot													1.5 ± 0.2	
NGC 5866	lobeN			0.097	15 06 29.344	55 45 40.77	<0.32			200	1.01 × <0.66	56.0	0.133	0.95 ± 0.19	core+jet, two lobes (D) 16″ →960pc
	core	0.12 × 0.07	20.8	0.097	15 06 29.492	55 45 47.66	7.6 ± 0.1	9.3		200	0.44 × <0.22	12.3	0.133	10.2 ± 0.2	
	lobeS			0.097	15 06 29.686	55 45 55.49	<0.37			200	1.11 × <0.75	163.8	0.133	0.83 ± 0.19	
	Tot													13.6 ± 0.5	
NGC 5879	core	0.19 × <0.14	27.2	0.071	15 09 46.801	57 00 01.58	0.37 ± 0.10	0.51		750	0.21 × 0.16	142.3	0.068	0.37 ± 0.09	core (A)
	Tot													0.49 ± 0.12	
NGC 5985	lobeN			0.057	15 39 37.031	59 19 55.95	<0.31		{	380	1.94 × <0.21	22.9	0.066	0.22 ± 0.09	double-lobed (D) 4″ →530pc
										200	1.06 × <1.91	2.5	0.34	0.25 ± 0.10	
	core			0.057	15 39 37.062	59 19 55.09	<0.17			380	0.36 × 0.32	15.7	0.066	0.21 ± 0.09	
	lobeS			0.057	15 39 37.130	59 19 53.45	<0.32		{	380	0.45 × 0.25	40.8	0.066	0.30 ± 0.09	
										200	1.35 × 0.66	145.1	0.34	0.35 ± 0.10	
	Tot													0.73 ± 0.15	
NGC 6702		0.08 × <0.24	19.6	0.074	18 46 57.534	45 42 20.57	0.20 ± 0.08	0.23		600	0.20 × <0.57	133.1	0.066	0.27 ± 0.09	twin jet (C) 2″ →656pc
	core			0.074	18 46 57.564	45 42 20.36	<0.22			600	0.36 × 0.10	96.6	0.066	0.22 ± 0.09	
		0.27 × 0.10	28.5	0.074	18 46 57.626	45 42 20.04	0.30 ± 0.08	0.34		600	0.29 × 0.56	137.5	0.066	0.42 ± 0.09	
	Tot													1.0 ± 0.1	
NGC 6703	core	0.18 × 0.04	128.8	0.066	18 47 18.823	45 33 02.34	0.26 ± 0.08	0.42		750	0.30 × <0.24	72.7	0.063	0.32 ± 0.08	core+jet (A)
	Tot													0.35 ± 0.09	
NGC 6946		0.04 × <0.16	66.4	0.057	20 34 52.172	60 09 14.20	0.37 ± 0.07	0.37		700	0.77 × 0.39	114.1	0.067	0.48 ± 0.07	jet+complex (E) 2.3″ →42pc
		0.38 × 0.16	133.8	0.057	20 34 52.242	60 09 14.20	0.83 ± 0.08	1.61		700	0.55 × 0.28	123.1	0.067	1.59 ± 0.08	
		0.24 × 0.10	0.33	0.057	20 34 52.255	60 09 14.42	0.61 ± 0.07	1.31		700			0.067	<2.57	
		0.21 × 0.03	56.0	0.057	20 34 52.273	60 09 13.20	0.48 ± 0.07	0.72		700	0.34 × <0.50	124.5	0.067	0.63 ± 0.08	
	core	0.09 × 0.04	12.5	0.057	20 34 52.299	60 09 14.20	0.49 ± 0.07	0.57		700			0.067	<0.35	
		0.17 × 0.10	12.7	0.057	20 34 52.320	60 09 14.10	0.67 ± 0.07	1.11		700	0.60 × 0.32	116.0	0.067	1.28 ± 0.08	
	Tot													10.0 ± 0.3	
NGC 6951		0.23 × 0.11	97.6	0.055	20 37 14.106	66 06 20.31	0.40 ± 0.08	0.66		750	0.05 × <0.21	142.6	0.065	0.63 ± 0.09	twin jet (C) 1.6″ →175pc

Table A1 – *continued*

Name	Comp	$\theta_{\rm M} \times \theta_{\rm m}$ arcsec	PA$_{\rm d}$ deg	Full resolution rms mJB	α(J2000)	δ(J2000)	$F_{\rm peak}$ mJB	$F_{\rm tot}$ mJy	$u - v$ kλ	$\theta_{\rm M} \times \theta_{\rm m}$ arcsec	PA$_{\rm d}$ deg	Low resolution rms mJB	$F_{\rm peak}$ mJB	morph/size
	core	0.06 × <0.23	83.3	0.055	20 37 14.118	66 06 20.10	0.25 ± 0.08	0.24	750	0.16 × <0.26	136.2	0.065	0.56 ± 0.09	
		0.14 × 0.06	172.9	0.055	20 37 14.144	66 06 19.76	0.51 ± 0.08	0.73	750	0.09 × <0.26	130.6	0.065	0.73 ± 0.09	
	Tot												1.0 ± 0.1	
NGC 7217		0.24 × 0.11	138.2	0.075	22 07 52.350	31 21 34.44	0.37 ± 0.09	0.72	700	0.19 × <0.17	99.0	0.063	0.67 ± 0.08	twin lobes (C) 1.5″ →120pc
	core	0.14 × <0.11	27.5	0.075	22 07 52.378	31 21 34.03	0.27 ± 0.09	0.28	700			0.063	<1.00	
		0.19 × 0.12	4.2	0.075	22 07 52.400	31 21 33.64	0.55 ± 0.09	0.79	700	0.21 × <0.21	8.9	0.063	0.79 ± 0.08	
	Tot												1.6 ± 0.2	
NGC 7798		0.14 × 0.12	22.1	0.031	23 59 25.410	20 44 59.38	0.33 ± 0.04	0.53	750	0.29 × 0.21	2.0	0.058	0.51 ± 0.07	triple source (C) 1.4″ →240pc
	core	0.22 × 0.06	162.2	0.031	23 59 25.444	20 44 59.43	0.23 ± 0.04	0.43	750			0.058	<0.34	
		0.35 × 0.20	28.1	0.031	23 59 25.494	20 44 59.57	0.23 ± 0.04	0.82	750	0.33 × 0.27	173.7	0.058	0.36 ± 0.07	
	Tot											1.8 ± 0.1		

Column description: (1) galaxy name; (2) radio component: core, jet, lobe, blob or unidentified component if not labeled (N or S stand for North or South); (3) deconvolved FWHM dimensions (major × minor axes, $\theta_{\rm M} \times \theta_{\rm m}$) of the fitted component, determined from an ellitpical Gaussian fit from the full-resolution radio map; (4) PA of the deconvolved component, PA$_{\rm d}$ from the full-resolution radio map (degree); (5) rms of the radio map close to the specific component from the full-resolution radio map (mJB, mJy beam^{-1}); (6)-(7) radio position in epoch J2000; (8) peak flux density in mJy beam^{-1}, $F_{\rm peak}$ from the full-resolution radio map: this represents the radio core flux density; (9) integrated flux density, F_{tot} in mJy, from the full-resolution radio map; (10) *uv*-taper scale of the low-resolution radio map in kλ; (11) deconvolved FWHM dimensions (major × minor axes, $\theta_{\rm M} \times \theta_{\rm m}$) of the fitted component, determined from an ellitpical Gaussian fit from the low-resolution radio map; (12) PA of the deconvolved component, PA$_{\rm d}$, from the low-resolution radio map (degree); (13) rms of the radio map close to the specific component from the low-resolution radio map (mJy beam^{-1}); (14) peak flux density in mJy beam^{-1}, $F_{\rm peak}$ from the low-resolution radio map. For NGC 5194 we give the total integrated flux densities of the radio lobes instead of the peak flux densities. At the bottom of each target the total flux density of the radio source associated with the galaxy is given in mJy, measured from the low-resolution map; (15) radio morphology (A, B, C, D, E) and size in arcsec and pc (see Section 4.2).

Table A2. Properties of the unidentified sources.

		Full resolution							Low resolution					
Name	Comp	$\theta_{\rm M} \times \theta_{\rm m}$ arcsec	PA$_{\rm d}$ deg	rms mJB	α(J2000)	δ(J2000)	$F_{\rm peak}$ mJB	$F_{\rm tot}$ mJy	$u - v$ kλ	$\theta_{\rm M} \times \theta_{\rm m}$ arcsec	PA$_{\rm d}$ deg	rms mJB	$F_{\rm peak}$ mJB	morph/size
NGC 891		0.23 × 0.10	10.6	0.063	02 22 33.230	42 20 58.56	0.27 ± 0.07	0.40	400	0.22 × 0.45	74.6	0.060	0.40 ± 0.08	multi-components
				0.063	02 22 33.441	42 20 54.70	<0.25		400	0.50 × 0.30	12.9	0.060	0.30 ± 0.08	
				0.063	02 22 33.451	42 20 54.27	<0.20		400	1.0 × <0.50	120.0	0.060	0.30 ± 0.08	
		0.24 × 0.17	65.6	0.063	02 22 33.705	42 20 48.80	0.25 ± 0.08	0.50	400	0.76 × 0.41	139.854	0.060	0.34 ± 0.08	
	Tot												1.5 ± 0.2	
NGC 2342		0.47 × <0.13	11.2	0.065	07 09 18.018	20 38 06.25	0.22 ± 0.08	0.36	750	0.64 × <0.22	163.2	0.068	0.46 ± 0.09	twin-jets? 2″ →692pc, 4″ offset
(field)				0.065	07 09 18.027	20 38 05.29	<0.40		750	0.44 × 0.16	32.1	0.068	0.42 ± 0.09	
	core?	0.13 × 0.11	136.8	0.065	07 09 18.027	20 38 05.83	0.39 ± 0.08	0.48	750	0.34 × 0.11	163.5	0.068	0.55 ± 0.09	
	Tot												1.7 ± 0.2	
NGC 3198		>0.19 × >0.08	166.6	0.114	10 19 54.519	45 32 57.07	0.35 ± 0.12	0.40	750	0.37 × >0.25	105.7	0.81	0.61 ± 0.09	elongated jet? 4.5″ →202pc, 6″ offset
(field)				0.114	10 19 54.520	45 32 53.35	<0.34		750	>0.29 × >0.32	171.3	0.81	0.62 ± 0.09	
	Tot												2.1 ± 0.2	
NGC 4013				0.070	11 58 31.321	43 56 49.86	< 0.24		500	0.20 × 0.02	58.4	0.064	0.23 ± 0.06	star-foring ring? 1.5″ →90pc
				0.070	11 58 31.402	43 56 49.57	<0.24		500	0.18 × 0.07	64.0	0.064	0.25 ± 0.06	
				0.070	11 58 31.422	43 56 51.85	<0.24		500	0.20 × <0.15	75.9	0.064	0.28 ± 0.06	
				0.070	11 58 31.433	43 56 50.05	<0.24		500	0.18 × <0.24	25.2	0.064	0.27 ± 0.06	
				0.070	11 58 31.455	43 56 50.46	<0.24		500	0.47 × 0.15	29.0	0.064	0.27 ± 0.06	
				0.070	11 58 31.481	43 56 50.63	<0.21		500	0.08 × <0.22	118.7	0.064	0.24 ± 0.06	
	Tot												3.8 ± 0.3	
NGC 5273				0.057	13 42 08.312	35 39 13.45	<0.19		500	0.35 × < 0.28	92.5	0.049	0.25 ± 0.05	star-forming ring? 3″ →230pc
				0.057	13 42 08.333	35 39 15.40	<0.22		500	0.92 × <0.32	167.5	0.049	0.31 ± 0.05	
				0.057	13 42 08.350	35 39 16.76	<0.23		500	0.87 × 0.22	159.3	0.049	0.28 ± 0.05	
		0.26 × <0.20	150.50	0.057	13 42 08.354	35 39 15.92	0.24 ± 0.06	0.33	500	0.92 × 0.12	155.1	0.049	0.30 ± 0.05	
				0.057	13 42 08.415	35 39 16.35	<0.25		500	1.30 × 0.22	140.3	0.049	0.32 ± 0.05	
	Tot												2.6 ± 0.2	
NGC 5676				0.085	14 32 47.221	49 27 51.79	<0.28		200	0.38 × <1.0	14.5	0.091	0.38 ± 0.09	multi-components, 27.7″ offset
				0.085	14 32 47.565	49 27 51.83	<0.26		200	0.46 × 0.2	30.7	0.091	0.31 ± 0.09	
	Tot												0.7 ± 0.2	
NGC 5907		0.19 × <0.13	22.2	0.097	15 15 49.124	56 20 26.42	0.44 ± 0.10	0.72	750	0.16 × <0.19	31.9	0.090	0.41 ± 0.09	multi-components, 55.7″ offset
		1.90 × 0.33	29.5	0.097	15 15 49.300	56 20 25.01	0.30 ± 0.10	0.53	750	1.90 × 0.15	69.9	0.090	0.33 ± 0.09	
		1.63 × 0.22	157.6	0.097	15 15 49.372	56 20 24.33	0.34 ± 0.10	0.52	750	0.63 × <0.35	145.8	0.090	0.42 ± 0.09	
	Tot												2.1 ± 0.2	

Table A2 – *continued*

		Full resolution							Low resolution					
Name	Comp	$\theta_{\rm M} \times \theta_{\rm m}$ arcsec	PA$_{\rm d}$ deg	rms mJB	α(J2000)	δ(J2000)	$F_{\rm peak}$ mJB	$F_{\rm tot}$ mJy	$u-v$ kλ	$\theta_{\rm M} \times \theta_{\rm m}$ arcsec	PA$_{\rm d}$ deg	rms mJB	$F_{\rm peak}$ mJB	morph/size
NGC 6015				0.082	15 51 23.775	62 18 44.72	<0.32		500	0.07 × 0.18	57.6	0.079	0.38 ± 0.10	multi-components, 11.6″ offset
				0.082	15 51 23.911	62 18 44.45	<0.35		500	1.03 × 0.36	4.5	0.079	0.50 ± 0.09	
				0.082	15 51 23.974	62 18 43.70	<0.34		500	<0.33 × <0.42	78.7	0.079	0.39 ± 0.09	
				0.082	15 51 24.037	62 18 42.17	<0.39		500	1.14 × <0.25	57.5	0.079	0.27 ± 0.09	
				0.082	15 51 24.039	62 18 41.945	<0.38		500	0.38 × 0.04	21.1	0.079	0.32 ± 0.09	
	Tot												2.6 ± 0.2	

Notes. Column description: (1) galaxy name; (2) radio component: core, jet, or lobe or unidentified component if not labeled (N or S stands for North or South); (3) deconvolved FWHM dimensions (major × minor axes, $\theta_{\rm M} \times \theta_{\rm m}$) of the fitted component, determined from an ellitpical Gaussian fit from the full-resolution radio map; (4) PA of the deconvolved component, PA$_{\rm d}$ from the full-resolution radio map (degree); (5) rms of the radio map close to the specific component from the full-resolution radio map (mJB, mJy beam^{-1}); (6)–(7) radio position in epoch J2000; (8) peak flux density in mJy beam^{-1}, $F_{\rm peak}$ from the full-resolution radio map; (9) integrated flux density, $F_{\rm rmtot}$ in mJy, from the full-resolution radio map; (10) *uv*-taper scale of the low-resolution radio map in kλ; (11) deconvolved FWHM dimensions (major × minor axes, $\theta_{\rm M} \times \theta_{\rm m}$) of the fitted component, determined from an ellitpical Gaussian fit from the low-resolution radio map; (12) PA of the deconvolved component, PA$_{\rm d}$ from the low-resolution radio map (degree); (13) rms of the radio map close to the specific component from the low-resolution radio map (mJy beam^{-1}); (14) peak flux density in mJy beam^{-1}, $F_{\rm peak}$ from the low-resolution radio map. At the bottom of each target the total flux density of the radio source associated with the galaxy is given in mJy, measured from the low-resolution map; (15) radio morphology, size in arcsec and pc, and offset from the optical centre, if present.

Table A3. Radio contour levels

Name	FR			LR			
	Beam	PA	Levels	kλ	beam	PA	levels
NGC 147	0.24 × 0.14	−63.2	0.18 × (−1,1)	750	0.537 × 0.25	−41.6	0.2 × (−1,1,1.5,2,2.3)
NGC 266	0.48 × 0.31	−40.0	0.21 × (−1,1,2,4)	750	0.57 × 0.37	−46.0	0.25 × (−1,1,2,4)
NGC 278	0.29 × 0.14	−55.2	0.11 × (−1,1,2)	750	0.54 × 0.25	−42.9	0.13 × (−1,1,1.5)
NGC 315	0.12 × 0.12	45.0	25.0 × (−1,1,5,15)	750	0.55 × 0.36	−45.7	10.0 × (−1,1,5,15,30)
NGC 410	0.52 × 0.32	−46.85	0.28 × (−1,1,2,4,7)	750	0.62 × 0.37	−49.9	0.28 × (−1,1,2,4,7)
NGC 507	0.46 × 0.35	−67.8	0.34 × (−1,1,1.5,2,2.5)	750	0.60 × 0.48	−64.6	0.34 × (−1,1,1.5,2,2.5)
NGC 777	0.23 × 0.15	7.6	0.165 × (−1,1,2,3,4)	600	0.29 × 0.26	58.7	0.21 × (−1,1,1.42,2,3,3.9)
NGC 891	0.20 × 0.17	65.6	0.15 × (−1,1,2)	400	0.59 × 0.53	−22.9	0.12 × (−1,1,1.5,2,2.4,3)
NGC 972	0.24 × 0.17	37.2	0.13 × (−1,1,1.5,2,2.7)	750	0.31 × 0.29	66.8	0.13 × (−1,1,1.5,2,3,4.2)
NGC 2273	0.20 × 0.16	48.1	0.20 × (−1,1,2,4,8,13)	750	0.33 × 0.27	85.1	0.20 × (−1,1,2,4,8,16,22)
NGC 2342	0.18 × 0.18	0.0	0.15 × (−1,1,1.5,2,2.5)	750	0.34 × 0.34	0.0	0.1 × (−1,1,1.5,2,2.5,3,3.5,3.9,4.15)
NGC 2342*	0.18 × 0.18	0.0	0.15 × (−1,1,2)	750	0.34 × 0.34	0.0	0.17 × (−1,1,1.9,2.4,3)
UGC 3828	0.19 × 0.16	50.3	0.15 × (−1,1,1.5,1.85)	750	0.33 × 0.26	89.3	0.15 × (−1,1,2,3)
NGC 2300	0.20 × 0.20	0.0	0.11 × (−1,1,2,3,5,8)	750	0.40 × 0.40	0.0	0.13 × (−1,1,2,3,5,8)
UGC 4028	0.20 × 0.20	0.0	0.17 × (−1,1,1.5)	750	0.40 × 0.40	0.0	0.13 × (−1,1,1.5,2.5,3.2)
NGC 2639	0.20 × 0.19	68.0	0.40 × (−1,1,2,4,8, 16,29,40)	750	0.34 × 0.26	−75.3	1.5 × (−1,1,2,4, 8,11.2,15)
NGC 2634	0.20 × 0.20	0.0	0.18 × (−1,1,2)	750	0.40 × 0.40	0.0	0.16 × (−1,1,2,2.5)
NGC 2681	0.19 × 0.16	51.8	0.17 × (−1,1,2,3,5)	750	0.34 × 0.26	−76.4	0.20 × (−1,1,1.7,2.5,3.5,5)
NGC 2655	0.20 × 0.20	0.0	0.20 × (−1,1,2,4,8, 16,32,64,128)	750	0.40 × 0.40	0.0	0.40 × (−1,1,2,4,8, 16,32,64,128)
NGC 2841	0.19 × 0.16	52.7	0.16 × (−1,1,1.5,2)	600	0.50 × 0.32	−53.6	0.17 × (−1,1,1.3,1.77,2.5,3)
NGC 3198	0.20 × 0.20	0.00	0.21 × (−1,1,1.5,2)	750	0.46 × 0.43	−25.4	0.15 × (−1,1,1.5,2,2.7)
NGC 3198*	0.20 × 0.20	0.00	0.3 × (−1,1,1.5)	750	0.46 × 0.43	−25.4	0.15 × (−1,1,1.5,3,4)
NGC 3414	0.22 × 0.14	20.60	0.11 × (−1,1,2,4,8)	750	0.47 × 0.34	−37.6	0.21 × (−1,1,2,4,8)
NGC 3430	0.20 × 0.20	0.0	0.17 × (−1,1,1.5,2)	750	0.48 × 0.37	−30.9	0.16 × (−1,1,1.5,2,2.5)
NGC 3432	0.47 × 0.28	−16.7	0.21 × (−1,1,2,3)	750	0.59 × 0.55	35.1	0.21 × (−1,1,2)
NGC 3665	0.20 × 0.20	0.00	0.23 × (−1,1,1.5, 2,5,12)	750	0.45 × 0.36	−34.6	0.90 × (−0.80, 1, 1.5, 2, 4)
				500	0.57 × 0.50	18.0	1.0 × (−0.80, 1, 1.5, 2, 4)
NGC 3675	0.17 × 0.14	−63.3	0.16 × (−1,1,1.5)	750	0.24 × 0.19	−54.0	0.14 × (−1,1,1.5,2)
NGC 3938	0.19 × 0.14	−54.2	0.15 × (−1,1,1.5)	750	0.24 × 0.19	−47.0	0.15 × (−1,1,1.5,2)
NGC 4013	0.19 × 0.14	−56.4	0.14 × (−1,1)	500	0.24 × 0.20	−51.0	0.09 × (−1,1,2,3)
NGC 4051	0.18 × 0.14	−58.6	0.19 × (−1,1,1.5,2, 2.5,3,3.5,4,5)	750	0.24 × 0.19	−53.13	3.0 × (−1,1,1.5,2,2.5, 3,3.5,4,5)
NGC 5005	0.21 × 0.19	27.0	0.19 × (−1, 1, 2, 3, 3.7, 4.5, 7, 8.5, 10.75, 12)	750	0.34 × 0.30	25.8	0.23 × (−1, 1, 2, 7, 16)
				200	1.57 × 1.28	11.9	0.70 × (−1, 1, 2, 3, 3.7, 10, 20)
NGC 5194	0.18 × 0.17	82.7	0.21 × (−1,1,2,3)	750	0.30 × 0.27	53.6	0.18 × (−1, 1, 2, 3, 6)
				500	0.47 × 0.42	14.7	0.18 × (−1, 1, 2, 2.5, 3.3, 5, 8)
NGC 5195	0.20 × 0.18	82.8	0.17 × (−1,1,1.5,2,2.8)	750	0.30 × 0.29	−59.9	0.21 × (−1,1,1.5,2,2.8)
NGC 5273	0.25 × 0.17	32.4	0.11 × (−1,1,1.5)	500	0.46 × 0.39	76.2	0.11 × (−1,1,1.5,2,2.4)

Table A3 – *continued*

Name	FR			LR			
	Beam	PA	Levels	kλ	beam	PA	levels
NGC 5353	0.18 × 0.14	29.6	0.90 × (−1,1,2,4,8,13)	500	0.24 × 0.22	66.3	0.70 × (−1,1,2,4,8,16)
NGC 5377	0.20 × 0.18	−86.5	0.18 × (−1,1,1.5)	750	0.51 × 0.39	4.3	0.19 × (−1,1,1.85,2.5)
NGC 5448	0.19 × 0.18	−86.6	0.19 × (−1,1,1.3, 1.6,1.85)	750	0.30 × 0.28	−51.8	0.19 × (−1,1,1.5,1.88,2.3)
NGC 5676	0.35 × 0.19	23.2	0.19 × (−1,1,1.5)	200	1.06 × 0.89	13.2	0.15 × (−1,1,1.5,2)
NGC 5866	0.18 × 0.18	0.0	0.40 × (−1,1,2,4,8,16)	200	1.00 × 0.96	−50.8	0.25 × (−1,1,2,3,6,15,30)
NGC 5879	0.18 × 0.18	0.0	0.15 × (−1,1,1.5,2,)	750	0.41 × 0.30	32.0	0.15 × (−1,1,1.5,2,2.5)
NGC 5907	0.28 × 0.19	18.6	0.20 × (−1,1,1.5)	750	0.42 × 0.30	29.8	0.19 × (−1,1,1.5,2)
NGC 5985	0.26 × 0.19	22.1	0.13 × (−1,1,1.5)	{ 380	0.58 × 0.55	78.3	0.11 × (−1, 1, 1.5, 2)
				200	1.13 × 0.96	−81.03	0.11 × (−1, 1, 1.5, 2, 2.5)
NGC 6015	0.23 × 0.18	25.4	0.15 × (−1,1,1.5,2)	500	0.48 × 0.42	67.5	0.15 × (−1,1,1.5,2,3)
NGC 6702	0.19 × 0.16	56.7	0.14(−1,1,2)	600	0.57 × 0.30	−51.2	0.12 × (−1,1,1.7,2.1,2.6,3.2)
NGC 6703	0.19 × 0.15	53.6	0.12 × (−1,1,1.5,2)	750	0.52 × 0.25	−51.51	0.10 × (−1,1,1.5,2.5)
NGC 6946	0.19 × 0.15	−84.1	0.13 × (−1,1,2,3,4,5.5)	700	0.52 × 0.27	−42.73	0.13 × (−1,1,2,3,4,8,11)
NGC 6951	0.20 × 0.15	88.5	0.13 × (1,1,1.5,2.5,3.5)	750	0.48 × 0.26	−39.3	0.13 × (−1,1,1.5,2.5,3.5,4.2,5)
NGC 7217	0.18 × 0.18	0.0	1.5 × (−1,1,1.5,2, 3,4,5)	700	0.40 × 0.4	0.0	1.5 × (−1,1,2,3,4,5)
NGC 7798	0.20 × 0.14	35.9	0.07 × (−1,1,2,3,4)	750	0.50 × 0.23	−41.0	0.1 × (−1,1,2,3,4)

Column description: (1) source name; (2) FWHM of the elliptical Gaussian restoring beam in arcsec of the full-resolution maps; (3) PA of the restoring beam (degree) of the full-resolution maps; (4) radio contour levels (mJy beam^{-1}) of the full-resolution maps (Fig. A1 and A2); (5) uvtaper scale parameter in kλ of the low-resolution radio maps; (6) FWHM of the elliptical Gaussian restoring beam in arcsec of the low-resolution maps; (7) PA of the restoring beam (degree) of the low-resolution maps; (8) radio contour levels (mJy beam^{-1}) of the low-resolution maps (Fig. A1 and A2). * identifies the secondary radio source detected in the field, probably a background AGN.

[1] *School of Physics and Astronomy, University of Southampton, Southampton, SO17 1BJ, UK*
[2] *Jodrell Bank Centre for Astrophysics, School of Physics and Astronomy, The University of Manchester, Manchester, M13 9PL, UK*
[3] *Jeremiah Horrocks Institute, University of Central Lancashire, Preston PR1 2HE, UK*
[4] *Departamento de Astrofisica y Ciencias de la Atmosfera, Universidad Complutense de Madrid, E-28040 Madrid, Spain*
[5] *Instituto de Astrofisica de Canarias, Via Lactea S/N, E-38205, La Laguna, Tenerife, Spain*
[6] *Departamento de Astrofisica, Universidad de La Laguna, E-38206, La Laguna, Tenerife, Spain*
[7] *Centre for Astrophysics Research, University of Hertfordshire, College Lane, Hatfield, AL10 9AB, UK*
[8] *Department of Space, Earth and Environment, Chalmers University of Technology, Onsala Space Observatory, 43992 Onsala, Sweden*
[9] *Instituto de Astrofisica de Andalucía (IAA, CSIC); Glorieta de la Astronomía s/n, 18008-Granada, Spain*
[10] *ALMA Regional Centre Node, UK*
[11] *Laboratoire AIM (CEA/IRFU – CNRS/INSU – Université Paris Diderot), CEA DSM/IRFU/SAp, F-91191 Gif-sur-Yvette, France*
[12] *Station de Radioastronomie de Nançay, Observatoire de Paris, PSL Research University, CNRS, Univ. Orléans, 18330 Nançay, France*
[13] *School of Physics and Astronomy, Cardiff University, Cardiff, CF243AA, UK*
[14] *Department of Physics & Astronomy, University College London, Gower Street, London WC1E 6BT, UK*
[15] *Astrophysics Group, Cavendish Laboratory, 19 J. J. Thomson Avenue, Cambridge CB3 0HE, UK*
[16] *Max-Planck-Institut für Radioastronomie, Auf dem Hügel 69, 53121 Bonn, Germany*
[17] *Department of Astrophysics/IMAPP Radboud University, Nijmegen, The Netherlands*
[18] *National Centre for Radio Astrophysics – Tata Institute of Fundamental Research, Postbag 3, Ganeshkhind, Pune 411007, India*
[19] *Department of Physics, Box 41051, Science Building, Texas Tech University, Lubbock, TX 79409-1051, USA*
[20] *Department of Physics, University of Bath, Claverton Down, Bath, BA2 7AY, UK*
[21] *INAF – IAPS Rome, Via Fosso del Cavaliere 100, I-00133 Roma, Italy*
[22] *Gemini North Operations Center, 670 N. A'ohoku Pl, Hilo, HI 96720, USA*
[23] *New York University Abu Dhabi, PO Box 129188, Abu Dhabi, UAE*
[24] *School of Physics and Astronomy, University of Birmingham, Edgbaston, Birmingham B15 2TT, UK*
[25] *Anton Pannekoek Institute, University of Amsterdam, Science Park 904, 1098 XH Amsterdam, The Netherlands*

This paper has been typeset from a TEX/LATEX file prepared by the author.